学位論文

Electron Microscopic Studies on Dynamics of Organic Molecules

（電子顕微鏡による有機分子ダイナミクスの研究）

平成 27 年 12 月博士（理学）申請

東京大学大学院理学系研究科

化学専攻

岡田　賢

Abstract

Any macroscopic chemical events are composed of numbers of molecular-level dynamics. However, due to the limitation of methods to visualize single molecules or small molecular clusters, the dynamics of molecules has been studied based on molecular ensembles, such as spectroscopies and optical micrographs. Recent development of electron microscopes gave access to investigate the molecular-level events, but still the observations remained qualitative. In this thesis, I have investigated four systems, namely, bond rotation, chemical reaction, crystal nucleation and growth, based on electron microscopic observation and theoretical treatments to demonstrate the quantitative aspects in the behavior of molecular dynamics.

Chapter 1 describes the short history of investigation of molecular dynamics, namely crystal nucleation, molecular vibration, and chemical reactions. Three approaches are described; theoretical calculations, experimental studies, and microscopic visualization. The achievements and the current issues in electron microscopic imaging are highlighted.

Chapter 2 describes the motion of organic molecules in vacuum and their visualization in single molecule atomic real time transmission electron microscopy (SMART-TEM). A Y-shaped biphenyl rotor attached on a carbon nanohorn has been reported to undergo C-C bond rotation under TEM observation condition as a conformational change between frames (K. Harano *et al. Nat. Mater.* **2012**, 877.). However, the origin of the apparent motion could not been elucidated from the qualitative imaging. I quantitatively analyzed the apparent motion of 4-bromophenyl- and 4-iodophenyl-tagged biphenyl rotor under various electron dose condition. Based on the TEM images and a quantum mechanical simulation of rotational motion, I found that each frame of the TEM images was constructed from accumulated snapshots of molecules. The observed result that the apparent motion frequencies became small when electron dose rate was increased or bromine was substituted for iodine matched with the expectation from the simulation, suggesting the quantum mechanical motion involving in SMART-TEM imaging of organic molecules.

Chapter 3 describes the dynamics of chemical reactions under SMART-TEM. Previously, [2 + 2] fullerene dimerization followed by rearrangement to obtain C_{120} was observed inside carbon nanotube, and their temperature dependence was qualitatively discussed (M. Koshino *et al*. *Nat. Chem.* **2010**, 117.). Here I analyzed the reaction kinetics based on a Rice-Ramsperger-Kassel-Marcus theory. The observed each reaction event was cumulated and fitted to find that both

dimerization and rearrangement processes follow first-order kinetics. This result shows that the kinetic analysis is possible at 10^{-22}-mol scale. The energy barrier for the reactions was elucidated from the fitting of temperature-dependent reaction rate. Both reactions are composed of two energetically different reaction pathways; temperature-dependent path from triplet excited state, and temperature-insensitive path from radical cation state with high vibrational energy.

Chapter 4 describes the dynamics of crystal nucleation of two typical donor molecules for organic solar cells; tetrabenzoporphyrin (BP) and poly(3-hexyltionphene-2,5-diyl) (P3HT) controlled by the chemical interaction at organic-organic interface. State-of-the-art scanning electron microscopy (SEM) revealed that both BP and P3HT form polycrystalline flat film with the size of several tenth of nanometers on poly(3,4-ethylene- dioxythiopnene) poly(4-styrenesulfonate) (PEDOT:PSS), a *de facto* standard anode buffer material. On the other hand, they formed randomly dispersed submicron crystals or submicron crystalline domain structure on graphitic surface. From other supporting experiments, the surface acidity of PEDOT:PSS was found to nucleate BP and P3HT by immobilizing one molecules on the surface of PEDOT:PSS.

Chapter 5 describes the dynamics of crystal growth of BP controlled by the viscosity of crystallization environment. BP film is prepared on a polycrystalline flat BP film by casting its soluble precursor solution with some organic matrices, and the crystal size of the additional BP layer depends on the viscosity of the matrices at 180 °C, at which temperature BP is generated from the precursor (M. Oiki, *M. S. Thesis*, UTokyo, **2014**). The nanocolumnar structure of BP is beneficial for organic solar cells, while the nanoscopic mechanism on the morphology has remained unclear. I revealed the molecular-level insight into the dependence of the morphology by spectroscopies, analysis of time-dependent morphologies in SEM, and numerical simulation. I found that the crystal growth of BP takes place at the order of seconds in high viscous matrices such as phenyl-C_{61}-butylic acid butyl ester, a typically used acceptor molecule (1250 Pa s at 180 °C), that explains the completion of crystallization in four minutes and the negligible increase in size under further heating.

Finally, Chapter 6 summarizes the present thesis and presents possible outcomes for further study of dynamics of molecules utilizing electron microscopes.

Acknowledgement

I express my greatest thanks to my supervisor, Prof. Dr. Eiichi Nakamura for his guidance, philosophical and strategic suggestions, and discussion throughout the whole research.

I am very grateful to Dr. Koji Harano for daily discussion, technical suggestions, and support for keeping the highly active environment through the whole research.

I express my sincere thanks to Prof. Dr. Kaoru Yamanouchi for his suggestions, teaching, and discussions based on quantum mechanics and unimolecular reaction mechanisms. Chapter 2 and 3 could not been completed without deep discussion with him.

I appreciate the discussion with Prof. Dr. Masaki Sano from the physical viewpoint on the molecular rotation, reaction, and crystal nucleation. He also supported me as a sub-supervisor

I have greatly benefited from Dr. Hayato Tsuji and Dr. Laurean Ilies who supported the research life and created a good laboratory environment with high safety.

I show my gratitude to people who experimentally contributed to my thesis. Dr. Tamás Szidarovszky calculated the quantum mechanics of bromine-substituted Y-shaped biphenyl rotor in Chapter 2. Ms. Aya Okubo helped me take TEM images in Chapter 2. Dr. Shunsuke Furukawa fabricated solar cells based on tetrabenzoporphyrin (BP) and fullerene in Chapter 4, and the result is included in the paper [2] and my M.S. thesis. Dr. Hideyuki Tanaka guided me on the device fabrication and discussion on device physics in Chapter 4 and 5. He also contributed to the device fabrication and discussion in the paper [2] and [4]. Mr. Motoharu Oiki performed the fabrication of partial device structure with various matrices and qualitatively discussed the time-dependent growth of tetrabenzo- porphyrin in Chapter 5. Prof. Dr. Hiroshi Watanabe in Institute for Chemical Research, Kyoto University performed rheological measurements of matrices in Chapter 5.

I deeply appreciate to people who contributed to my thesis through discussion. Prof. Dr. Ludwik Leibler in Ecole Supérieure de Physique et de Chimie Industrielles (ESPCI), Paris, France discussed with me on the morphology of polymer system in Chapter 4. He also kindly offered me a chance to visit his laboratory to study polymer system and computation for four months. Dr. Yoshiharu Sato in Mitsubishi Chemical Co., Ltd. discussed with me on device physics in Chapter 4 and 5.

I appreciate people who contributed to papers that are not included in the thesis. Mr. Akira Yasuhara in JEOL Ltd. took TEM images for the paper [1]. Prof. Dr. Hiroshi Yabu and Mr. Hiroki Sato provided sample for SEM imaging in the paper [3]. Dr. Yonggang Zhen and Prof. Dr. Yutaka

Matsuo prepared porphyrin derivatives in the paper [4].

I thank people who trained my TEM image acquisitions and discussed on the images. Mr. Hashime Hoshi, Dr. Akihiko Kumamoto and Dr. Naoya Shibata in Graduate School of Engineering, UTokyo, Dr. Mitsuhiro Saito in Jeol Ltd., Prof. Dr. Masahide Kikkawa and Dr. Haruaki Yanagisawa in School of Medicine, UTokyo.

During my three-year Ph. D course, I had the opportunity to study abroad twice. I would like to thank people in Prof. Leibler's laboratory in ESPCI, France who guided my research; Dr. François Tournilhac, Dr. Renaud Nicolay, Ms. Marie-France Boucher, and the laboratory members. I would like to thank people in Saint Petersburg State University, Russia who accepted me as a visiting student; Prof. Dr. Igor Vasilievits Murin, Prof. Dr. Valerii Pavlovich Tolstoy, and Dr. Semenov Konstantin Nikolaevich.

I would like to thank my colleagues for cross-encouragement; Mr. Junya Yamada, Mr. Tatsuaki Matsubara, and Mr. Kazutaka Shoyama.

I appreciate current and former members in Dr. Harano's subgroup members for supporting me through daily discussion and laboratory management; Fr. Yonggang Zhen, Dr. Chao Liu, Dr. Sai Prakash Maddala, Ms. Utako Takeda, Dr. Kosuke Minami, Dr. Hirohisa Nitta, Dr. Ricardo Mizoguchi Gorgoll, Ms. Mami Nakatake, Mr. Takakazu Seki, Mr. Kei Matsumoto, Mr. Yuki Itabashi, Mr. Junfei Xing, Ms. Mayuko Isomura, Mr. Takuya Tsubota, Mr. Hiroki Hanayama, Ms. Satori Kowashi, Ms. Mallory Sea, and Mr. Naoaki Shinjo.

I am indebted to all of my laboratory colleagues who showed immense support. I would like to name Dr. Sobi Asako for his kind help on his guidance for computational methods. I would like to thank Ms. Akemi Maruyama and Dr. Takao Kaneko for their daily support for laboratory management.

I would like to thank Mr. Akira Sugimoto for daily support of my life in the chemistry department.

I would like to acknowledge Advance Leading Graduate Course for Photon Science (ALPS), Program for Leading Graduate Schools, MEXT for financial support as a fellowship and providing the opportunity to study under Prof. Leibler in France for four months. I also thank Students and Researchers Exchange Program in Sciences (STEPS) with Russian universities for providing the opportunity to visit Saint Petersburg State University for two weeks.

TEM imaging in Chapter 2 was conducted in Research Hub for Advanced Nano

Characterization, The University of Tokyo, under the support of "Nanotechnology Platform" (project No. 12024046) by MEXT, Japan.

Finally, I would like to thank my mother Ms. Miyoko Okada for physical and mental support for everyday life. I have no doubt that I could not finish this thesis without her help.

List of Publications

1. Koji Harano, Shinya Takenaga, Satoshi Okada, Yoshiko Niimi, Naohiko Yoshikai, Hiroyuki Isobe, Kazu Suenaga, Hiromichi Kataura, Masanori Koshino, Eiichi Nakamura “Conformational Analysis of Single Perfluoroalkyl Chains by Single-Molecule Real-Time Transmission Electron Microscopic Imaging”, *The Journal of the American Chemical Society* **2014**, *136*, 466–473.

2. Koji Harano, Satoshi Okada, Shunsuke Furukawa, Hideyuki Tanaka, Eiichi Nakamura “Formation of a Polycrystalline Film of Donor Material on PEDOT:PSS Buffer Induced by Crystal Nucleation”, *Journal of Polymer Science Part B: Polymer Physics* **2014**, *52*, 833–841.

3. Masaaki Kanahara, Hiroki Satoh, Takeshi Higuchi, Atsushi. Takahara, Hiroshi Jinnai, Koji Harano, Satoshi Okada, Eiichi Nakamura, Yasutaka Matsuo, Hiroshi Yabu “Fabrication of NIR-Excitable SERS-Active Composite Particles Comprised of Densely-Packed Au Nanoparticles on Polymer Microparticles“ *Particle & Particle Systems Characterization* **2015**, *32*, 441–447.

4. Yonggang Zhen, Hideyuki Tanaka, Koji Harano, Satoshi Okada, Yutaka Matsuo, Eiichi Nakamura “Organic Solid Solution Composed of Two Structurally Similar Porphyrins for Organic Solar Cells“, *The Journal of the American Chemical Society* **2015**, *137*, 2247–2252.

(Publications 1, 3, and 4 are not included in this thesis.)

Abbreviations

‡	transition state
°C	degrees Celsius
Δ	prefix for a change in parameter
Å	angstrom
γ	interfacial energy
η	viscosity
θ	angle
μ	prefix for micro
τ	time constant
Ψ	eigenfunction
$\rho(E)$	density of states
A, a_x (x = d, r)	pre-exponential factor
AFM	atomic force microscopy (microscope)
APCI	atomospheric pressure chemical ionization
aq	aqueous solution
ATR	attenuated total reflection
Bu	*n*-butyl
BP	21*H*,23*H*-tetrabenzo[*b*,*g*,*l*,*q*]porphyrin
br	broad
c_x (x = d, r)	temperature-independent rate constant
C3	spherical abberation
C5	fifth-order spherical aberration
CCD	charge coupled device
CNH	carbon nanohorn (aggregate)
CNT	carbon nanotube
CP	1,4:8,11:15,18:22,25-tetraethano-29*H*,31*H*-tetrabenzo[*b*,*g*,*l*,*q*]porphyrin
d	chemical shift, diameter
d	day(s), doublet (spectral), denoting dimerization reaction (subscript)
D	diffusion coefficient
DEPT	distorsionless enhancement by polarization transfer
DLS	dynamic light scattering
DMF	*N*, *N*-dimethylformamide
DMSO	dimethyl sulfoxide
E	(eigen)energy
E_a	apparent activation energy of diffusion
E_x (x = d, r)	activation energy
e	electrons
e_t	total electron dose
eq	equivalent(s), equation
eV	electron volts
G	Gibbs free energy
GIXD	glazing incidence X-ray diffraction
GPC	gel permeation column chromatography
$g_{\theta\theta}$	rotation inertia
h	Planck's constant
$\hbar$	Dirac's constant
h	hour(s)
H	enthalpy
$\hat{H}$	Hamiltonian
HOMO	highest occupied molecular orbital
HOPG	highly oriented pyrolytic graphite
HRMS	high-resolution mass spectrometry
Hz	Hertz
IP	ionization potential
IR	infrared spectroscopy
ISC	intersystem crossing

ITO	indium tin oxide
J	joule(s)
J	coupling constant
K	kelvin(s) (absolute temperature)
k	prefix for killo
k_B	Boltzmann's constant
k_{et}	rate constant of electron transfer
k_{neu}	rate constants at triplet excited state
k_{rad}	rate constants at radical cation state
k_{rot}	rotational frequency
k_x (x = d, r)	rate constants of dimerization/ rearrangement reaction
L	liter
LUMO	lowest unoccupied molecular orbital
m	prefix for milli, moderate (spectral)
M	prefix for mega
MCP	*N, N´*-dicarbazoyl-3,5-benzene
n	prefix for nano
n	number
N	number of eigenstates ($N(\varepsilon)$)
N_A	Avogadro's number
NMR	nuclear magnetic resonance
mp	melting point
OPV	organic photovoltaics
P_n (n = 1, 2)	extent of step n reaction
P3HT	poly(3-hexylthiophene-2,5-diyl)
Pa	Pascal
PCBNB	phenyl C_{61}-butylic acid n-butyl ester
PEDOT	poly(3,4-ethylenedioxythiophene)
PSS	poly(4-stylenesulfonate)
PES	potential energy surface
Ph-iGO	phenyl isocyanate-attached graphene oxide
ppm	parts per million
PTFE	poly(tetrafluoroethylene)
$q_‡$	partition function of a transition state
q_i	partition function of an initial state
r	denoting rearrangement reaction (subscript)
r	radial distance
$\vec{r}$	three-dimensional position
R	gas constant
r_H	hydrodynamic radius
r_{ij}	inter-atom distance between atom i and j
rGO	reduced graphene oxide
rpm	rotation per minute
RRKM	Rice-Ramsperger-Kassel-Marcus
rt	room temperature
s	second(s), singlet (spectral), strong (spectral)
S	supersaturation ratio
SE1	secondary electron generated by the incident beam
SE2	secondary electron generated after multiple scattered events
sec	second(s)
SEM	scanning electron microscopy
SET	single electron transfer
SMART-TEM	single-molecule atomic real-time transmission electron microscopy
T	temperature
T_s	stage temperature
T_m	temperature of molecules
t	time
TED	total electron dose
TEM	transmission electron microscopy

TG	thermoglavimetry
THF	tetrahydrofuran
TMS	tetramethylsilane
u	concentration of a solute
UV	ultraviolet
v	volume of a molecule
V	volt(s)
vdW	van der Waals
vis	visible
VT	variable temperature
w	weak (spectral)
w	concentration of a solute weighted by radial distance
wt%	weight per cent
Y	1,3,5-tris(4-bromophenyl)benzene
$\mathbf{Y_I}$	1,3,5-tris(4-iodophenyl)benzene
Y-CNH	carbon nanohorn attached with 4"-bromo-5'-(4-bromophenyl)-[1,1':3',1"-terphenyl]-4-carboxamide
$\mathbf{Y_I}$**-CNH**	carbon nanohorn attached with 4"-iodo-5'-(4-iodophenyl)-[1,1':3',1"-terphenyl]-4-carboxamide

Contents

Chapter 1. General Introduction

1-1 Dynamics of Organic Molecules

Chemistry is explained based on single molecules or their assemblies that are as small as single nm or less, and we observe the behavior of statistically averaged behavior of molecular ensembles. In order to get insight into the molecular events, scientists have utilized three methodologies; experimental investigations, theoretical calculations, and microscopic observations. Experimental studies apply some perturbation to the bulk system and observe the response that originates from the statistical change of molecular ensembles. Theoretical calculations deal with single molecules to calculate physical properties of single molecules and molecular assemblies assuming that the single molecule represent the statistical average of the system.

On the contrary to the experimental and theoretical works that put their basis on the statistics, microscopic observation visualize individual molecules or molecular assemblies to so that unique behavior that is out of expectation from the statistical average can be observed.[1] Electron microscopes are one of the tools that can visualize atomic to mm-level objects utilizing the (sub-)Å wavelength of electrons; conventional scanning electron microscopy (SEM) uses electrons down to 50 eV that has the wavelength of 1.73 Å, and transmission electron microscopy (TEM) uses electrons of ~100 keV that has the wavelength of 0.037 Å. Despite the fact that the obtained images are phenomenological and qualitative without detailed analysis, the microscopic methods play key roles in nanoscience. Here I show the interplay of experimental, theoretical, and microscopic studies by taking examples of crystallization, molecular motion and chemical reaction, which are the focus of this thesis.

1-2 Dynamics of Molecular Assemblies –Crystallization–

Crystals are hierarchical assemblies of molecules, and they are formed by crystal nucleation and growth, i.e. formation of seeds of crystals followed by adsorption of molecules. The theoretical discussion on the crystallization was initially presented by Gibbs based on thermodynamics.[2] The competition between free energy of the bulk solid ΔG_{bulk} and the surface free energy $\Delta G_{\mathrm{surface}}$ determines the thermodynamics;

$$\Delta G = \Delta G_{\mathrm{bulk}} + \Delta G_{\mathrm{surface}} = -\frac{4\pi r^3}{3v} k_{\mathrm{B}} TS + 4\pi r^2 \gamma \qquad \text{(eq.1-1)}$$

where r is the radius of the crystal, v is the volume of the crystal, k_{B} is the Boltzmann's constant, S is the supersaturation ratio defined by the concentration of the solution divided by the maximum solubility at the given temperature, and γ is the interfacial energy at crystal-liquid contact, respectively (Figure 1-1a). This theoretical idea has been supported by various experimental proofs.

Eq. 1-1 shows that either increase in supersaturation ratio S or decrease in the interfacial energy γ facilitates crystallization. High S is easily achieved by removal of the solvent, known in salt evaporation pond. Decreasing γ has been achieved by chemically designing the surface structures so that the surface acquires high affinity to the solute molecules via hydrogen bonding and hydrophobic interactions.[3]

The thermodynamic expression has been described in molecular level using spherical solute molecules and a continuum solvent media (Figure 1-1b).[4] Initially, solute molecules aggregate each other to form amorphous cluster composed of several- to several tenth of molecules. The formation of this cluster called pre-nucleation cluster requires some energy so that supercooled liquid can exist in some cases. Next, molecules in a pre-nucleation cluster undergo translational and rotational motion to change the molecular ordering in the cluster, and finds out the energy minimum where the molecules are hierarchically packed. Thus obtained structure is called a crystal nucleus, which is thermodynamically unstable so that further adsorption of solute molecules, or crystal growth, takes place to grow into a macroscopic crystal.

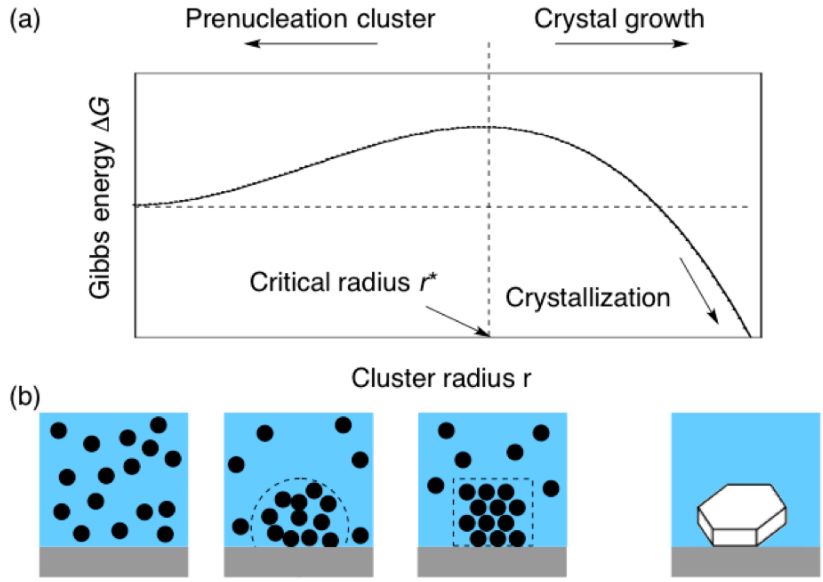

Figure 1-1. Mechanism of crystal nucleation. (a) Thermodynamic expression and (b) molecular-level description using rigid spherical solute (black dots).

Besides the success in describing the crystallization by the solid sphere model, several questions remained to apply the mechanisms directly to organic molecules. [5] In the crystallization of organic molecules, anisotropy, conformational flexibility, and various intermolecular interactions such as hydrogen bonding and π-π interaction makes the theoretical treatment more complex than that using a spherical model,[6] and the importance of solute-solvent interaction on specific crystal

surface is recognized to determine the crystal habit during the crystal growth process.[7]

Microscopic methods enable the study of each crystallization event in atomic to optically visible scale. TEM with an atomic resolution enables visualization of pre-nucleation cluster of calcium carbonate.[8] *In situ* observation is also a powerful tool to study the time-evolution of crystallization of gold[9] and platinum[10] nanoparticles, and dissolution of inorganic molecules.[11] On the contrary to inorganic clusters, visualization of crystals of organic molecules have been considered difficult due to sample decomposition by electron beam irradiation.[12] One way to access to the organic molecules is the cryogenic technologies with minimum electron dose and sometimes with metal staining, which are applied to visualize the intermediate structure of self-assembly process of the capsid proteins of tobacco mosaic virus.[13] Another way is to visualize single molecules that do not form crystals, since the electron radiation damage is not well accumulated in the isolated single organic molecules. In this method called single molecule atomic real time (SMART)-TEM, Nakamura *et al*. observed a single molecule and aggregate of up to 15 organic molecules, proving existence of pre-nucleation cluster during crystallization for organic molecules.[14] SEM gives the information on the molecular clusters, and enables nm-scale visualization of crystal growth,[15] morphology, and habits.[16] It can snapshoot the crystal growth process by obtaining samples from crystallization system, and the morphological evolution helps understanding of crystallization. For example, crystallization of metal organic framework was found to involve layered sheet before formation of cubic crystals.[17]

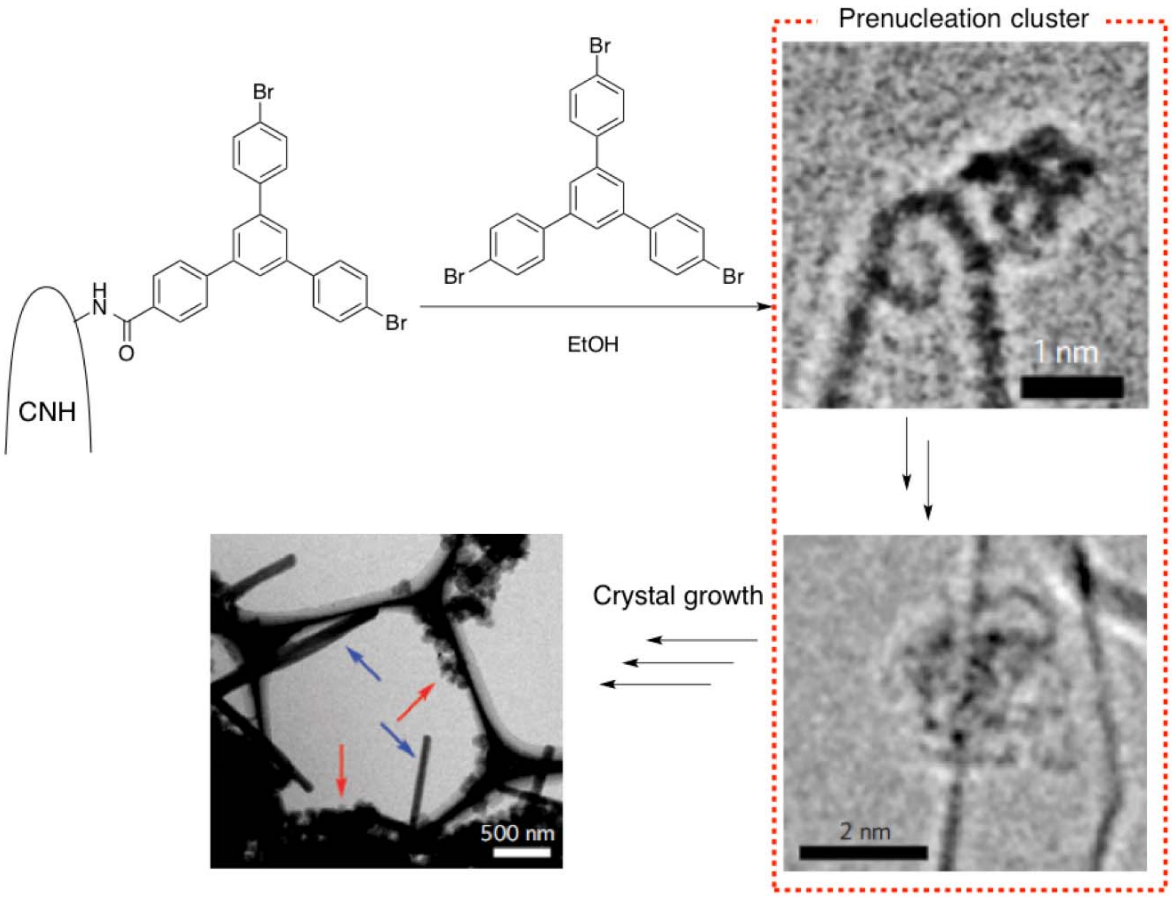

Figure 1-2. TEM imaging of the pre-nucleation clusters and their evolution into needle crystals of 1,3,5-tris(4-bromophenyl)benzene. TEM and SEM images were reprinted from ref. [14a] with permission from Nature Publishing Groups.

1-3 Dynamics of Single Molecules –Molecular Vibration-

Molecules not only translationally move and rotate as observed in crystallization, but also vibrate and change their conformations. The molecular vibration has also been studied theoretically, spectroscopically, and microscopically. Coblentz initially performed spectroscopic investigation of molecular vibration in 1905, and assigned several functional groups.[18] Dennison performed theoretical discussion based on Heisenberg equation in 1926, mentioning the application of the calculated result to C-C bond rotation of ethane.[19]

It required one century visualizing vibration-related phenomena in a single molecule level. Qualitative TEM imaging of conformational change of C-C bonds was performed in 2007 using alkyl chains entrapped inside single-walled carbon nanotubes (CNT) that act as a one-dimensional "optical cell" for TEM (Figure 1-3).[20] Not only alkyl chains but also perfluoroalkyl chain,[21] amide-aryl bond,[22] and motion of metal atoms inside fullerene[23] were observed. Interestingly,

alkyl chains inside CNT can be sometimes exposed to outer side, and this indicates the existence of hole defects in the CNT vessel.[24] Molecules exposed to vacuum were also found to undergo conformational change as demonstrated in a Y-shaped biphenyl rotor[14] and alkylamide-tethered biotin[25] attached onto a dahlia-shaped aggregate of CNT called carbon nanohorn.[26] Graphene, an atomically thin two-dimensional carbon layer, can be also used as a substrate to display gold nanoclusters to visualize their motion.[27]

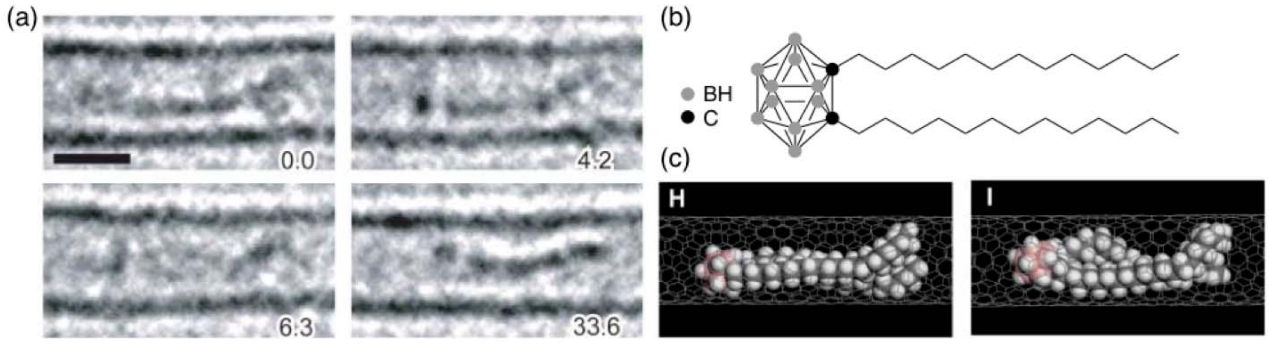

Figure 1-3. TEM imaging of C-C bond rotational motion of alkyl chains attached on a *ortho*-carborane and encapsulated inside CNT. (a) TEM images. Numbers show the frame time in seconds. Scale bar is 1 nm. (b) Chemical structure. (c) Molecular model. TEM and modeling images were reproduced from ref. [20] with permission from American Association for the Advancement of Science.

1-4 Chemical Reactions under Electron Microscopy

Chemical reactions, the most fundamental aspects of chemistry, have also been observed in TEM. CNT undergo transformation and cleavage under an electron beam, and the reaction is dependent on electron beam voltage.[28] Structurally similar boron-nitride nanotube also decompose under TEM imaging and the low electron conductivity is considered to accelerate decomposition.[29] In the case of graphene, iron-catalyzed rearrangement on edge was visualized.[30] Chemical reactions on graphene take place without any catalyst as a form of ejection of carbon atoms.[31] These chemical events depend on the beam energy,[32] and people in TEM society call this as “knock-on damage”. However, the knock-on is essentially a bond cleavage “reaction” and should be expressed in chemical perspective.

In order to trap small molecules, the beam-fragile CNT was used as a reaction vessel because it is convenient to deal with one-dimensional vessel for focusing on the specimen molecules. Dimerization followed by rearrangement of fullerene molecules inside CNT was initially reported as an example of chemical reactions of discrete molecules.[33] Endohedral

fullerenes as well as pristine fullerene reacted to form short CNT inside CNT vessel. Similar CNT formation was also observed in metal complexes of fullerenes, $[Re(\mu_5\text{-}C_{60}H_5)(CO)_3]$[34] and $[Os_3(CO)_9(\mu_3\text{-}\eta^2,\eta^2,\eta^2\text{-}C_{60})]$. [35] Electron-induced reaction was observed for analogues of metallocenes; buckyferrocene and buckyruthenocene that undergo C-C bond reorganization and C-H bond cleavage to form C_{70} fullerene, which is the first example to obtain compounds with the discrete structure by electron beam irradiation.[36] Sulfur-terminated graphene nanoribbons also reacted inside CNT.[37]

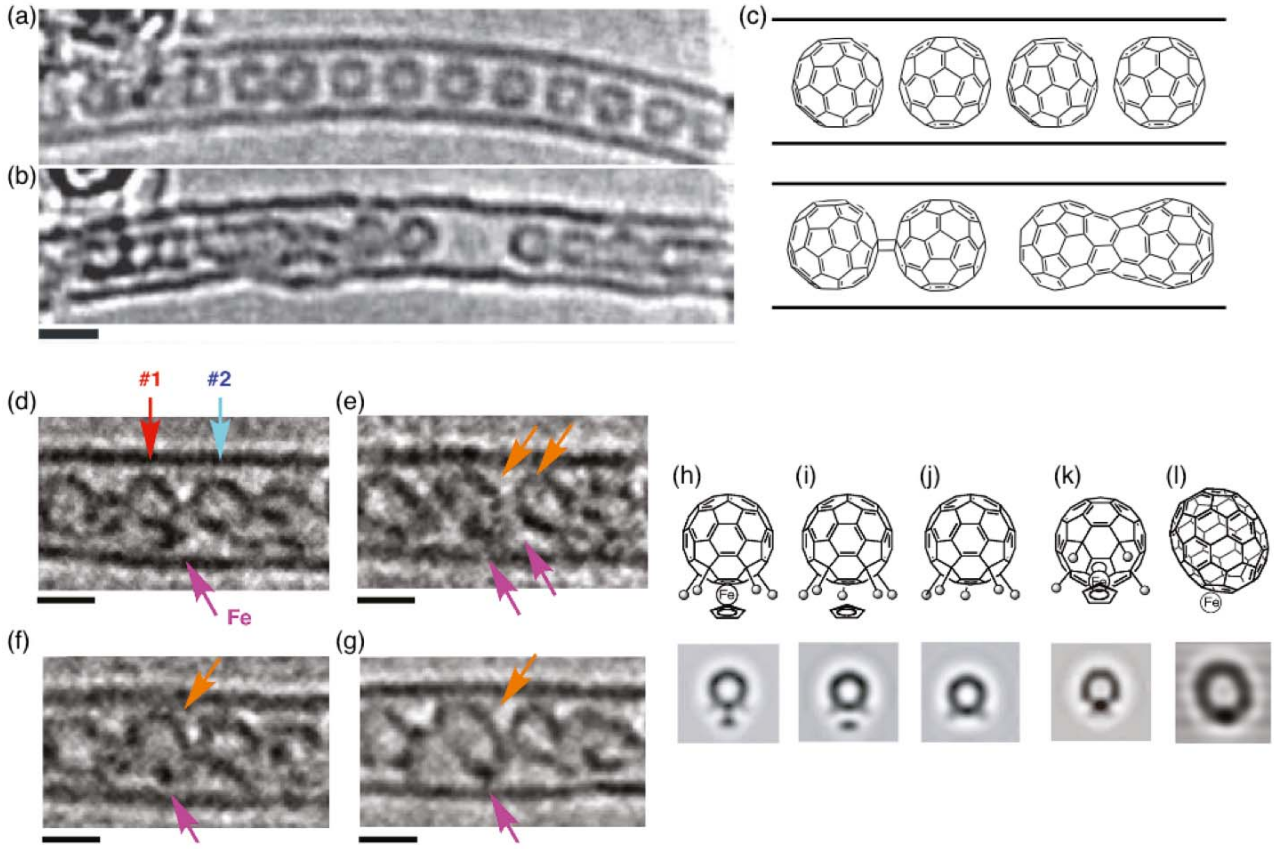

Figure 1-4. Representative TEM images of chemical reactions at 120 kV, 293 K. (a–c) Reaction of C_{60} observed at the total electron dose of (a) 1.3×10^6 and (b) 2.5×10^7 electrons nm^{-2}. (c) Typical structure of the C_{60} and its dimer. TEM images were reprinted from ref. [33] with permission from Nature Publishing Group. (d–l) TEM images of buckyferrocene $Fe(C_{60}Me_5)Cp$ (#1 and #2) in a single-walled CNT taken at the total electron dose of (d) 3.7×10^4, (e) 2.2×10^5, (f) 3.0×10^5, and (g) 1.6×10^6 electrons/nm^2. (e) Molecular models and TEM simulation images of the buckyferrocene viewed from the side. Balls in the models represent methyl groups. (f) Model of a buckyferrocene without an iron atom. (g) Model of pentamethyl- fullerene. (h) Buckyferrocene viewed from the top. (i) [70]Fullerene with an iron atom on the surface. Scale bars are 1 nm. Reprinted with permission from ref. [36]. Copyright (2011) American Chemical Society.

1-5 Current Issues in Electron Microscopic Imaging of Dynamics of Molecules

As stated in the introduction, electron microscopic studies are qualitative without special experimental techniques although microscopic observation can reveal dynamics of molecules in the spatial resolution of single molecule to molecular assembly that were otherwise inaccessible. Here I summarize general problems in electron microscopy that has not been clearly solved so far.

(1) What is the surrounding environment of the molecules and how does the environment contribute to molecular motion? The molecules should undergo conformational change by bond vibration and translational motion by heat transfer from surrounding environment. In addition to the heat, inelastic electron-specimen interaction transfers some energy to the specimen as observed in electron energy loss, which may also contribute to molecular motion.[38] There also exists a hypothesis that the temperature that molecules feel in TEM might be cooler than that of the stage.[21] Thus the origin of the motion is still in controversy.

(2) How do electrons affect the stability of organic molecules? As shown above, some organic molecules such as fullerene and its derivatives react, and others do not. The electron-sample interaction is the most probable factor to determine the stability, or so-called irradiation damage. The imaging principles in atomic resolution TEM including the irradiation damage have been developed for inorganic solids that have periodic structures.[39] However, whether this discussion is also applicable to the system of single organic molecules should be carefully investigated.

(3) How can we quantitatively understand the observed dynamics, or can the phenomena be explained in coherence with theories? Since theories are developed for single molecules and then applied for statistical ensembles, high-resolution microscopic imaging of the chemical events in which one or few molecules are involved is an appropriate system to investigate the coherence.

1-6 Focus of This Thesis

In this work, I have studied molecular vibrations, chemical reactions, crystal nucleation and crystal growth to solve the three problems mentioned in section 1-5. Question (3) is always discussed in all the chapters.

In Chapter 2, question (1) is solved based on imaging principles of TEM, quantum mechanics of molecular vibration and TEM imaging with variable electron dose rate.

In Chapter 3, questions (2) and (3) are solved by analyzing reaction kinetics of dimerization followed by rearrangement of two fullerene molecules inside carbon nanotube observed in TEM.

In Chapter 4, crystal nucleation of tetrabenzoporphyrin is studied by SEM, and it shows that the crystal nucleation on surface is templated by surface-immobilized molecules.

In Chapter 5, morphological control during crystal growth by the viscosity of the crystallization system is discussed based on spectroscopies, SEM, and diffusion equations. This chapter connects the macroscopic parameters with nm-scale events.

In Chapter 6, the topics in the present thesis are summarized with implications derived from the obtained results.

References

[1] (a) Reimer, L. *Scanning Electron Microscopy: Physics of Image Formation and Microanalysis*; Springer-Verlag: Berlin, 1998. (b) Williams, D. B.; Carter, C. B. *Transmission Electron Microscopy*; Springer: New Work, 2009. (c) Nakamura, E. *Angew. Chem. Int. Ed.* **2013**, *52*, 236–252.

[2] Gibbs, J. W.; *Am. J. Sci.* **1878**, *16*, 441–458.

[3] (a) Mannsfeld, S. C.; Briseno, A. L.; Liu, S.; Reese, C.; Roberts, M. E.; Bao, Z. *Adv. Funct. Mater.* **2007**, *17*, 3545–3553. (b) Briseno, A. L.; Mannsfeld, S. C. B.; Ling, M. M.; Liu, S.; Tseng, R. J.; Reese, C.; Roberts, M. E.; Yang, Y.; Wudl, F.; Bao, Z. *Nature* **2006**, *444*, 913–917. (c) Diao, Y.; Helgeson, M. E.; Myerson, A. S.; Hatton, T. A.; Doyle, P. S.; Trout, B. L. *J. Am. Chem. Soc.* **2011**, *133*, 3756–3759. (d) Diao, Y.; Whaley, K. E.; Helgeson, M. E.; Woldeyes, M. A.; Doyle, P. S.; Myerson, A. S.; Hatton, T. A.; Trout, B. L. *J. Am. Chem. Soc.* **2012**, *134*, 673–684.

[4] (a) Davey, R. J.; Schroeder, S. L. M.; Horst, ter, J. H. *Angew. Chem. Int. Ed.* **2013**, *52*, 2166–2179. (b) De Yoreo, J. J.; Vekilov, P. G. *Rev. Mineral. Geochem.* **2003**, *54*, 57–93. (d) Otálora, F.; García-Ruiz, J. *Chem. Soc. Rev.* **2014**, *43*, 2013–2026.

[5] Gránásy, L.; Podmaniczky, F.; Tóth, G. I.; Tegze, G.; Pusztai, T. *Chem. Soc. Rev.* **2014**, *43*, 2159.

[6] Price, S. L. *Chem. Soc. Rev.* **2014**, *43*, 2098–2111.

[7] Theoretical work: Hartman, P.; Bennema, P. *J. Cryst. Growth* **1980**, *49*, 145–156.

Experimental works: (a) Dang, L.; Wei, H.; Zhu, Z.; Wang, J. *J. Cryst. Growth* **2007**, *307*, 104–111. (b) Niu, W.; Zhang, W.; Firdoz, S.; Lu, X. *J. Am. Chem. Soc.* **2014**, *36*, 3010–3012. (c) Mukherjee, G.; Biradha, K. *Cryst. Growth Des.* **2011**, *11*, 5649–5658.

[8] (a) Achlioptas, D.; D'Souza, R. M.; Spencer, J. *Science* **2009**, *323*, 1453–1455. (b) Gebauer, D.; Kellermeier, M.; Gale, J. D.; Bergström, L.; Cölfen, H. *Chem. Soc. Rev.* **2014**, *43*, 2348–2371.

[9] Uematsu, T.; Baba, M.; Oshima, Y.; Tsuda, T.; Torimoto, T.; Kuwabata, S. *J. Am. Chem. Soc.* **2014**, *136*, 13789–13797.

[10] Liao, H. G.; Zherebetskyy, D.; Xin, H.; Czarnik, C.; Ercius, P.; Elmlund, H.; Pan, M.; Wang, L. W.; Zheng, H. *Science* **2014**, *345*, 916–919.

[11] Cordeiro, M. A. L.; Crozier, P. A.; Leite, E. R. *Nano Lett.* **2012**, *12*, 5708–5713.

[12] Egerton, R. F. *Phys. Status Solidi A* **1976**, *37*, 663–668.

[13] Butler, P. J. G.; Bloomer, A. C.; Finch, J. T. *J. Mol. Biol.* **1992**, *224*, 381–394.

[14] (a) Harano, K.; Homma, T.; Niimi, Y.; Koshino, M.; Suenaga, K.; Leibler, L.; Nakamura, E. *Nat. Mater.* **2012**, *11*, 877–881. (b) Vekilov, P. G. *Nat. Mater.* **2012**, *11*, 838–840.

[15] Zheng, C.; Greer, H. F.; Chiang, C.-Y.; Zhou, W. *CrystEngComm* **2014**, *16*, 1064–1070.

[16] (a) Huang, W.-C.; Lyu, L.-M.; Yang, Y.-C.; Huang, M. H. *J. Am. Chem. Soc.* **2012**, *134*, 1261–1267. (b) Han, Y.-J.; Aizenberg, J. *J. Am. Chem. Soc.* **2003**, *125*, 4032–4033.

[17] (a) Zheng, C.; Greer, H. F.; Chiang, C.-Y.; Zhou, W. *CrystEngComm.* **2014**, *16*, 1064–1070. (b) Kim, J.; Dolgos, M. R.; Lear, B. J. *Cryst. Growth Des.* **2015**, *15*, 4781–4786.

[18] Coblentz, W. W. *Phys. Rev.* **1905**, *20*, 337–363.

[19] Dennison, D. M. *Phys. Rev.* **1926**, *28*, 318–333.

[20] Koshino, M.; Tanaka, T.; Solin, N.; Suenaga, K.; Isobe, H.; Nakamura, E. *Science* **2007**, *316*, 853.

[21] Harano, K.; Takenaga, S.; Okada, S.; Niimi, Y.; Yoshikai, N.; Isobe, H.; Suenaga, K.; Kataura, H.; Koshino, M.; Nakamura, E. *J. Am. Chem. Soc.* **2014**, *136*, 466–473.

[22] Solin, N.; Koshino, M.; Tanaka, T.; Takenaga, S.; Kataura, H.; Isobe, H.; Nakamura, E. *Chem. Lett.* **2007**, *36*, 1208–1209.

[23] Warner, J. H.; Watt, A. A. R.; Ge, L.; Porfyrakis, K.; Akachi, T.; Okimoto, H.; Ito, Y.; Ardavan, A.; Montanari, B.; Jefferson, J. H.; Harrison, N. M.; Shinohara, H.; Briggs, G. A. D. *Nano Lett.* **2008**, *8*, 1005–1010.

[24] Koshino, M.; Solin, N.; Tanaka, T.; Isobe, H.; Nakamura, E. *Nat. Nanotechnol.* **2008**, *3*, 595–597.

[25] (a) Nakamura, E.; Koshino, M.; Tanaka, T.; Niimi, Y.; Harano, K.; Nakamura, Y.; Isobe, H. *J. Am. Chem. Soc.* **2008**, *130*, 7808–7809. (b) Gorgoll, R. M.; Yücelen, E.; Kumamoto, A.; Shibata, N.; Harano, K.; Nakamura, E. *J. Am. Chem. Soc.* **2015**, *137*, 3474–3477.

[26] Iijima, S.; Yudasaka, M.; Yamada, R.; Bandow, S.; Suenaga, K.; Kokai, F.; Takahashi, K. *Chem. Phys. Lett.* **1999**, *309*, 165–170.

[27] Bosch-Navarro, C.; Laker, Z. P. L.; Thomas, H. R.; Marsden, A. J.; Sloan, J.; Wilson, N. R.; Rourke, J. P. *Angew. Chem. Int. Ed.* **2015**, *54*, 9560–9563.

[28] Smith, B. W.; Luzzi, D. *J. Appl. Phys.* **2001**, *90*, 3509–3515.

[29] Arenal, R.; Lopez-Bezanilla, A. *ACS Nano* **2014**, *8*, 8419–8425.

[30] Zhao, J.; Deng, Q.; Avdoshenko, S. M.; Fu, L.; Eckert, J.; Rummeli, *Proc. Natl. Acad. Sci. USA* **2014**, *111*, 15641–15646.

[31] Meyer, J. C.; Eder, F.; Kurasch, S.; Skakalova, V.; Kotakoski, J.; Park, H. J.; Roth, S.; Chuvilin, A.; Eyhusen, S.; Benner, G.; Krasheninnikov, A. V.; Kaiser, U. *Phys. Rev. Lett.* **2012**, *108*, 196102.

[32] (a) Egerton, R. F.; Wang, F.; Crozier, P. A. *Microsc. Microanal.* **2005**, *12*, 65–71. (b) Egerton, R. F. *Microsc. Res. Tech.* **2012**, *75*, 1550–1556.

[33] Koshino, M.; Niimi, Y.; Nakamura, E.; Kataura, H.; Okazaki, T.; Suenaga, K.; Iijima, S. *Nat. Chem.* **2010**, *2*, 117–124.

[34] Chamberlain, T. W.; Meyer, J. C.; Biskupek, J.; Leschner, J.; Santana, A.; Besley, N. A.; Bichoutskaia, E.; Kaiser, U.; Khlobystov, A. N. *Nat. Chem.* **2011**, *3*, 732–737.

[35] Chamberlain, T. W.; Champness, N. R.; Schröder, M.; Khlobystov, A. N. *Chem. Eur. J.* **2010**, *17*, 668–674.

[36] Nakamura, E.; Koshino, M.; Saito, T.; Niimi, Y.; Suenaga, K.; Matsuo, Y. *J. Am. Chem. Soc.* **2011**, *133*, 14151–14153.

[37] Chuvilin, A.; Bichoutskaia, E.; Gimenez-Lopez, M. C.; Chamberlain, T. W.; Rance, G. A.; Kuganathan, N.; Biskupek, J.; Kaiser, U.; Khlobystov, A. N. *Nat. Mater.* **2011**, *10*, 687–692.

[38] Egerton, R. F. *Rep. Prog. Phys.* **2009**, *72*, 016502.

[39] Williams, D. B.; Carter, C. B. *Transmission Electron Microscopy*; Springer: New Work, 2009; pp. 23–72.

Chapter 2. Quantum Mechanics of Internal Rotor Probed by Single Molecule Transmission Electron Microscopic Imaging

2-1 Introduction

Molecules undergo global rotation,[1] bond vibration,[2] and translational motion on surface[3], in a confined space[4] and in a liquid phase[5] that have been traced by transmission electron microscopy (TEM), scanning transmission electron microscopy, and scanning probe microscopy. When one part of the molecules is fixed on a solid support, translational and rotational motions are inhibited while vibration including bond rotation remains active to undergo conformational changes. The bond rotation has been recently visualized in single-molecule atomic real-time TEM (SMART-TEM) imaging as a conformational difference between two adjacent frames of the sequential movies. So far, motions of alkyl chains,[6] perfluoroalkyl chains,[7] pyrene amide,[8] Y-shaped biphenyl,[9] and biotin-tagged alkylamide[10] encapsulated inside carbon nanotube or attached on a carbon nanohorn (CNH) have been observed under vacuum. Although these SMART-TEM images qualitatively showed apparent motions in the time scale of seconds, the quantitative discussion on the motion frequencies and the explanation on the origin of the apparent motion still remain unclear. Here I show that the origin of the apparent motion in SMART-TEM images as quantum mechanical nature of the molecules by taking an example of Y-shaped internal rotor attached on carbon nanohorn (**Y-CNH**) that show C-C bond rotation of biphenyl core (Figure 2-1). First I explain the failure of classical mechanics in treating the bond rotation, and then explain the origin of apparent motion based on the principles of TEM imaging methods coupled with quantum mechanics. The quantum mechanical consideration gives the conclusion that the image sharpness is the function of the total electron dose, and finally it is experimentally proven by SMART-TEM imaging with variable electron dose and different inertia of the rotor.

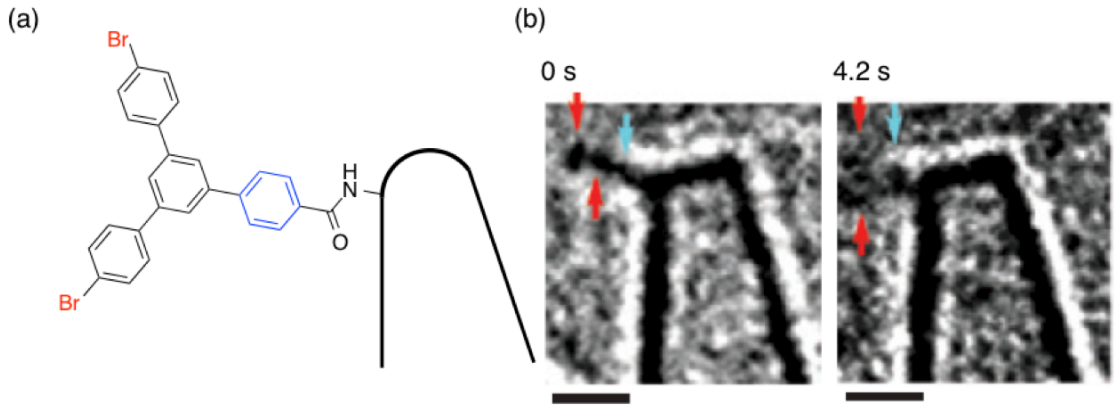

Figure 2-1. C-C bond rotation of **Y-CNH** observed by SMART-TEM. (a) Structure of biphenyl rotor, and (b) representative TEM images taken at 120 kV. Red and blue arrows indicate Br atoms and a benzene ring, respectively. Scale bars are 1 nm. TEM images were reprinted from ref. [9] with permission from Nature Publishing Groups.

2-2 Description of Molecular Motions in Classical Mechanics

The apparent shape of two-dimensionally projected Y-shaped biphenyl rotor changes by C-C bond rotation of two adjacent benzene rings. The C-C bond rotation of biphenyl mostly undergoes through the transition state with minimum energy barrier among several possible transition states. The energy barrier of bond rotation was evaluated at MP2/6-31G(d,p) level of theory using the model system, assuming that the energy barrier mostly depends on the local structure (Figure 2-2, experimental section). The minimum energy barrier was found on C-C bond rotation of biphenyl when two phenyl groups are perpendicular to each other, and the Gibbs free energy barrier $\Delta G^{\ddagger}$ was calculated to be 10.3 kJ/mol at 298.15 K, 1 atm. This Gibbs free energy barrier gives the rotational frequency k_{rot} from Eyring equation

$$k_{rot} = \frac{k_B T}{h} \exp\left(-\frac{\Delta G^{\ddagger}}{RT}\right) \qquad \text{(eq.2-1)}$$

where k_B is the Boltzmann's constant, h is the Planck's constant, T is the temperature, and R is the gas constant. Assuming the temperature of the biphenyl rotor as the same as that of the sample stage at 293 K, k_{rot} is calculated as 9.15×10^{10} s^{-1}. Based on classical mechanics, this result indicates that the molecule is continuously rotating at this frequency. Since overall molecular shape is averaged in TEM images, resulting in the same images at any frame.

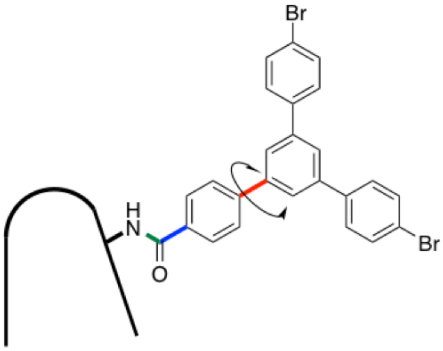

	$\Delta H^{\ddagger}$ [kJ mol^{-1}]	$\Delta G^{\ddagger}$ [kJ mol^{-1}]	k_{rot} [s^{-1}]	Structural model
Biphenyl C-C	5.82	10.23	9.15×10^{10}	
CO-biphenyl C-C	12.28	15.09	1.24×10^{10}	
Amide C-N	55.01	75.43	1.28×10^{2}	
CNH-amide C-N	25.85	59.87	2.37×10^{7}	

Figure 2-2. Minimum enthalpy ($\Delta H^{\ddagger}$), Gibbs free energy barriers ($\Delta G^{\ddagger}$) and rate constants of bond rotation that contributes to significant structural change of **Y-CNH** calculated for model structures at MP2/6-31G(d,p) level of theory at 298.15 K, 1 atm. Calculation details are shown in Chapter 2-8 experimental section.

On the contrary to this classical mechanical assumption, Y-shaped biphenyl rotor randomly changes its appearance under TEM observation (Figure 2-3 and Figure 2-4). The apparent motions were determined by the change of the shape of Y-shaped rotor by making a movie of two

adjacent frames. A typical published sequential TEM images shows one apparent C-C bond rotation within 6.6 s in average, or $k_{rot} = 1.5 \times 10^{-1}$ s^{-1}, and the interval between images is not uniform. This result may lead to the assumption that the temperature of the molecules is cooled down from the stage temperature. Assuming that the apparent motion truly reflects the real motion of the molecules, Eq. 2-1 gives T = 26 K. Notably, even 100 times faster rotation is assumed, the temperature is still 30 K. However, this result contradicts with the fact that there is a black-body radiation from the TEM chamber with the temperature of 293 K.

From these results, either or both of the following assumptions were found to be wrong; (1) the molecules follow classical mechanical motion, and (2) the apparent motion observed in TEM images directly expresses the molecular motion. In order to clearly understand the origin of apparent motions, understanding of principles in both TEM imaging and molecular motions are required.

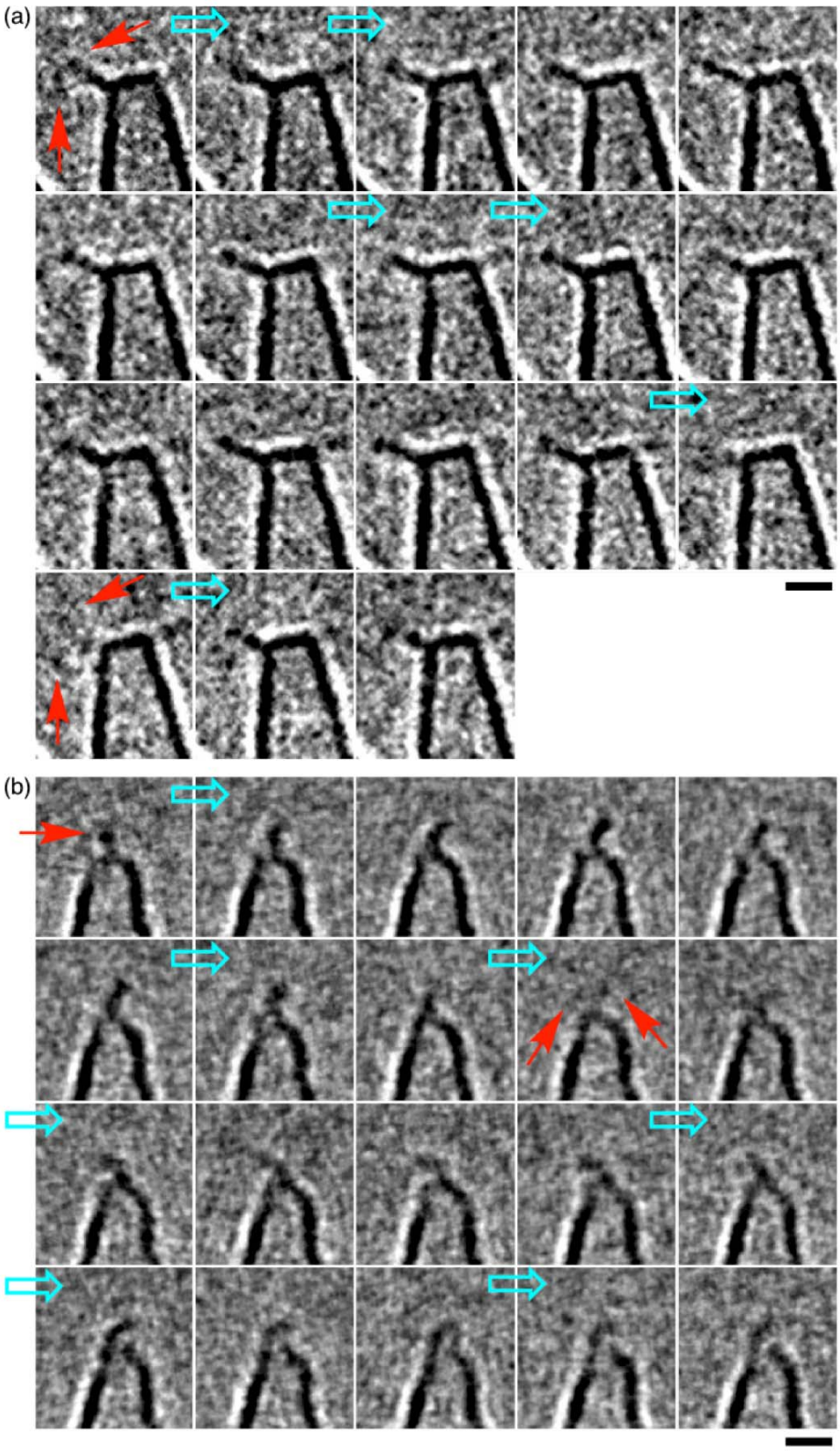

Figure 2-3. SMART-TEM images of Br-substituted biphenyl rotor on CNH taken at 120 kV, 7.2 $\times 10^2$ electrons $Å^{-2}$ s^{-1}. Red and blue arrows indicate two Br atoms and apparent motions, respectively. Scale bars are 1 nm. TEM images were reprinted from ref. [9] with permission from Nature Publishing Groups.

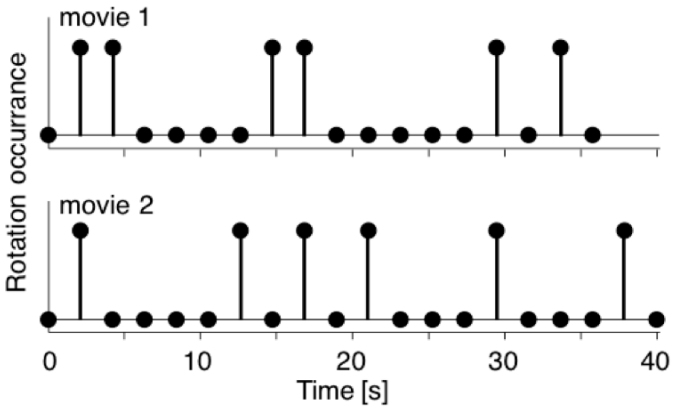

Figure 2-4. Frequency of rotational motion of biphenyl rotor. Dots with bars indicate significant difference in image from previous frame or disappearance of molecules illustrated in blue arrows in ***Figure 2-3***. Data were acquired from SMART-TEM movies in ref.9.

2-3 Principles in TEM Imaging

Unlike optical imaging, TEM images are constructed by limited numbers of electrons. In TEM imaging using conventional charge coupled device (CCD) camera, 10^4–10^6 electrons nm^{-2} frame^{-1} is irradiated within 0.4 s followed by data processing for 0.8 s (Figure 2-5a). In other words, single electron is introduced to one nm^2 in every 1–100 μs. In addition, TEM imaging at 120 kV uses electrons with the speed of 8.7×10^6 m s^{-1}, or 2.9% of the speed of light, that is, the electron beam paths through an organic molecule with the typical thickness of 0.3 nm within 3.4×10^{-17} s (Figure 2-5b). In classical mechanics, the time constant one C-C bond rotation event τ is given by

$$\tau = \frac{1}{k_{\mathrm{rot}}} = 1.13 \times 10^{-11} \left[\mathrm{s}\right] \qquad \text{(eq.2-2)}$$

and six orders of magnitude slower than the time of electron-sample interaction. This shows that electron beam snapshots the molecules without motion of the nuclei. The speed of electrons in TEM is faster than 10^6 m s^{-1} (cf. 3.6×10^6 m s^{-1} at 80 kV, $\tau = 2.73 \times 10^{-11}$ s), and the following discussion would be valid for TEM observation at any conventional beam voltage.

One may think of the ionization of molecules by the incident electron, however, this do not change the conclusion that the bond rotation observed in TEM is mainly due to the C-C bond rotation of biphenyl at the ground state. Some of the incident electron irradiated at 120 kV removes either outer-shell or inner-shell electrons, and the vacancies at the inner shell is filled by the outer shell in ~10^{-14} s to generate a cation radical.[11] The radical cation then accepts one electron from CNH to neutralize its charge in 10^8–10^{10} s^{-1},[12] which is faster enough than the time interval between electron irradiation to the biphenyl rotor, 10^4–10^6 s^{-1}. Since the incident electrons

contributed to ionization lose some of the energy and are scattered in large angle that are cut by aperture, the electrons contribute to contrast formation always possess information of neutral molecules.

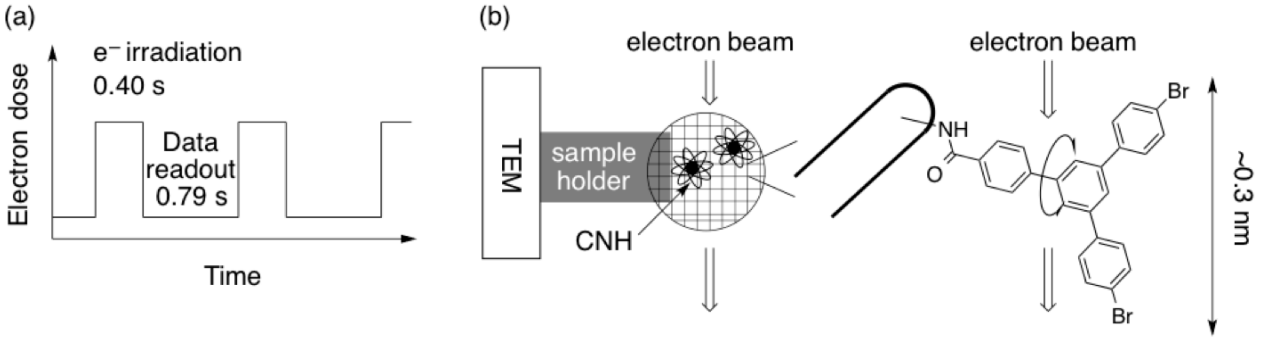

Figure 2-5. Image acquisition in TEM. (a) Temporal diagram of electron dose and image acquisition. (b) Setup of single molecule TEM imaging.

Among the 10^2–10^4 electrons $Å^{-2}$ $frame^{-1}$, some of them interact with specimen molecules and contribute to generation of image contrast, while others pass through samples. The number of scattered electrons was calculated from TEM images at three different electron doses (Figure 2-6). The dark-contrasted part of CNH and Br were determined by the simulation based on molecular models, and the number of electrons at each pixel in the raw images on the red-squared regions in the below figure was counted and averaged. Similarly, the background was determined, and the distance between CNH and the sample region of background were more than 1 nm to avoid contrast originating from the inelastically scattered electrons and interference from CNT. The result shows that the scattered electrons were 6–12% of the introduced electrons at any electron dose rate (Figure 2-6b). This indicates that 10^3–10^5 electrons contribute to construct the image contrast of the biphenyl rotor with the maximum two-dimensional projection size of 1.24 nm^2.

(a)

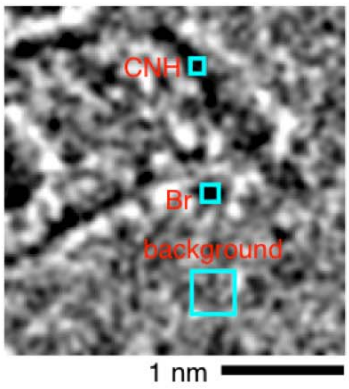

(b)

Background	CNH	Br
(1.97 ± 0.00) x 10^3	(2.14 ± 0.01) x 10^3 (8.6 %)	(2.14 ± 0.00) x 10^3 (8.6 %)
(4.56 ± 0.00) x 10^3	(5.10 ± 0.03) x 10^3 (11.8 %)	(4.95 ± 0.05) x 10^3 (8.6 %)
(2.03 ± 0.00) x 10^4	(2.16 ± 0.10) x 10^3 (6.0 %)	(2.19 ± 0.07) x 10^3 (7.5 %)

Figure 2-6. Measurement of the number of electrons contributing to generation of image contrast. (a) A typical TEM image of **Y-CNH** taken at 120 kV, 5.1 × 10^3 electrons Å^{-2} s $^{-1}$ = 2.0 × 10^3 electrons Å^{-2} frame^{-1}. (b) Number of electron counts in electrons Å^{-2} frame^{-1} sampled from the blue square in (a). The data was averaged from 5 frames with the size of > 10 pixels. Contribution to contrast is shown in parenthesis.

2-4 C-C Bond Vibration in Quantum Mechanics

The rotational motion of biphenyl is described from quantum mechanical viewpoint. The quantum states of the rotor is given by solving the Schrödinger equation

$$\hat{H}\Psi = E\Psi \qquad \text{(eq.2-3)}$$

using a Hamiltonian

$$\hat{H} = -\frac{\hbar^2}{2g_{\theta\theta}}\frac{\partial}{\partial\theta^2} + \frac{\Delta H^{\ddagger}}{2}\left[\cos(2\theta)+1\right] \qquad \text{(eq.2-4)}$$

where Ψ and E are the eigenfunction and eigenvalues for the rotational states, respectively, $g_{\theta\theta}$ is the inertia of the rotor given by $g_{\theta\theta} = \sum_i m_i l_i^2$ where m_i and l_i are the mass and the distance of ith atom from the rotation axis, respectively, and θ is the angle of the rotor (Figure 2-7a). Using the calculated enthalpy barrier for rotation $\Delta H^{\ddagger}$ of 5.82 kJ/mol, 652 eigenstates were found below the barrier, and $|\Psi|^2$ gives the angular probability of the rotor (Figure 2-7b). The population of each eigenstate follows Boltzmann distribution, and the probability to tilt more than 45° is calculated to be 0.0% at 30 K and 4% at 298 K. This indicates that we have almost no possibility to observe rotation if the stage temperature is below 30 K, and the low-temperature assumption was denied. In addition, 46% of the rotor exists within 10° from the equilibrium position at 298 K, indicating the relatively high probability to find bromine atoms at a similar position.

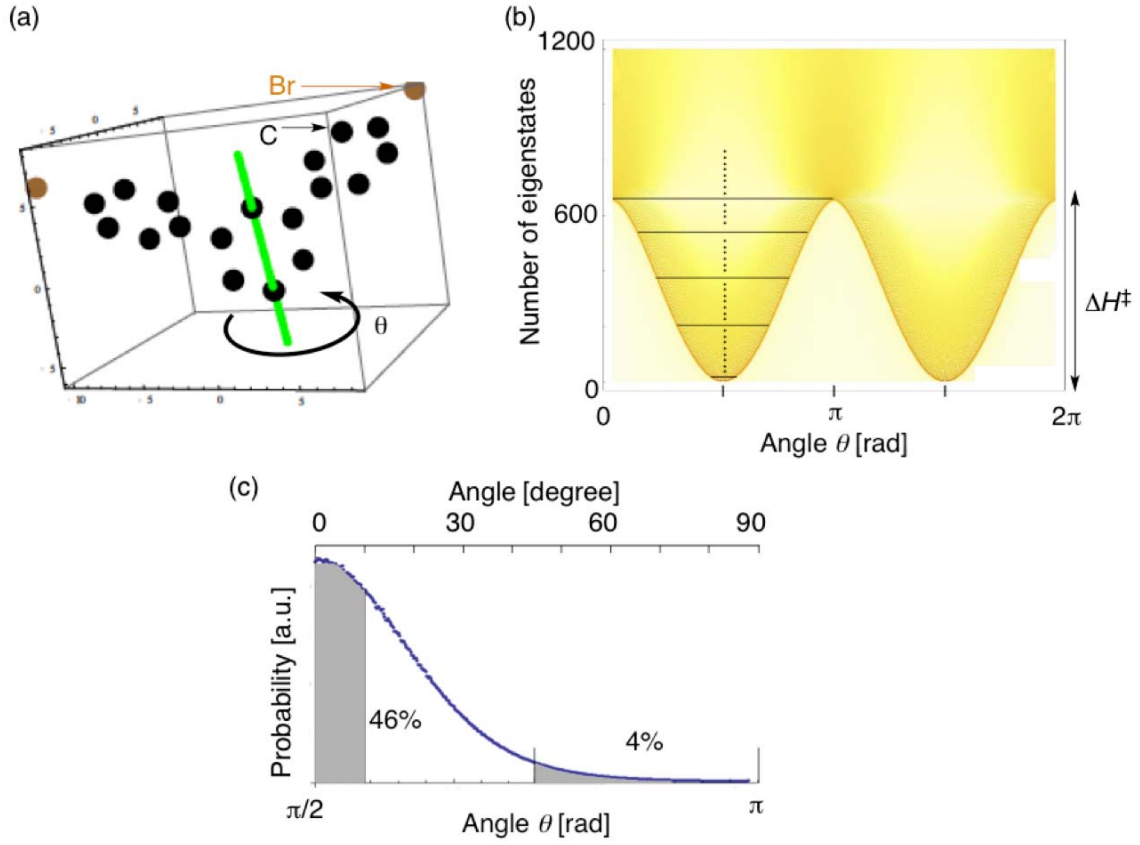

Figure 2-7. Calculation of angular probability of biphenyl rotor. (a) A structural model of biphenyl rotor used for calculation. Hydrogen atoms were omitted for clarity. Black and brown circles show carbon and bromine, and green line shows the rotation axis, respectively. (b) Eigenvalues and color plot of the angular probablity density of the rotor. Dense yellow color indicate high probability. (c) Angular probability of the biphenyl rotor.

In order to simulate TEM images out of the quantum mechanical motion, 50 or 100 bromine atom positions were sampled from the probability density in Figure 2-7b. Sampling was performed when electron beam is irradiated parallel (Figure 2-8a–c) and perpendicular (Figure 2-8d–f) to the equilibrium position of Br-rotating center-Br plane. Regardless of the beam direction, the position of dark contrast from Br atom rarely changes at 100 sampling frame^{-1}, while it deviates much and sometimes contrast is not clearly observed at 50 samples frame^{-1}. The deviation in the contrast is recognized as an apparent motion in SMART-TEM images. This result indicates that the image become sharp at high electron doses, and the image blurs much at few electron doses. In addition, increasing the electron dose twice significantly change the apparent motion.

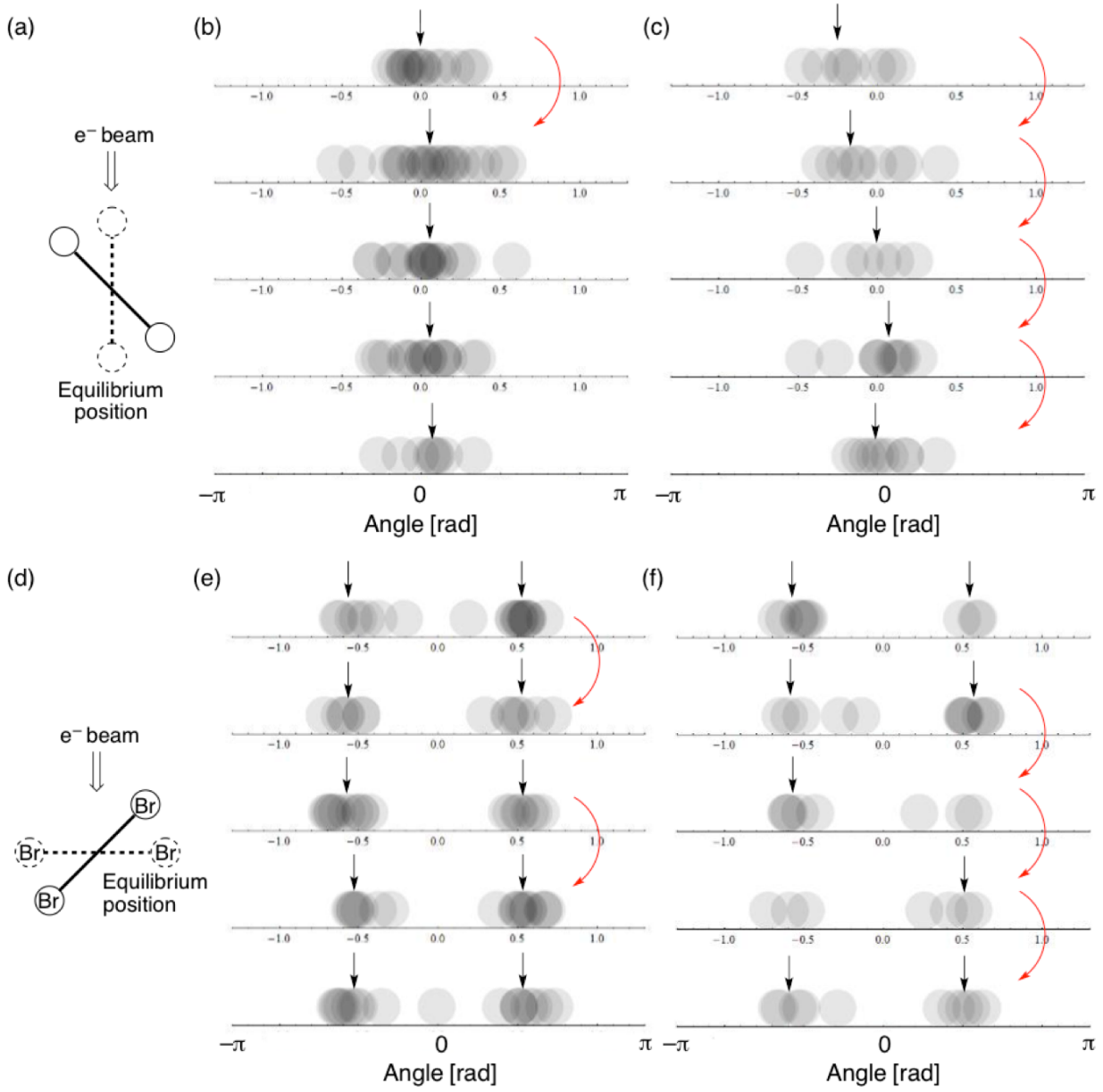

Figure 2-8. Simulation of electron scattering events. (a–c) Electron beam is irradiated parallel to the Br-Br plane, and the electron scattering contrast from Br is shown. (a) A schematic image of beam irradiation to the rotor. (b) Br images simulated with 100 scattering events, and (c) 50 scattering events. (d–f) Electron beam is irradiated perpendicular to the Br-Br plane, and the electron scattering contrast from Br is shown. (d) A schematic image of beam irradiation to the rotor. (e) Br images simulated with 100 scattering events, and (f) 50 scattering events. Center position of the contrast and inter-frame deviation in contrast center, i.e. apparent motion, is noted in black and red arrows, respectively.

2-5 Apparent Motion Frequencies of Br-Substituted Biphenyl Rotor

In order to prove the inverse correlation between the number of scattering events and the apparent motion, biphenyl rotor was chemically attached onto carbon nanohorn (CNH) and observed in SMART-TEM. In the previous observation, carboxylic acid succinimide ester was used as a precursor to introduce Y-shaped rotor onto CNH to afford **Y-CNH**.[9] The succinimide-mediated method can functionalize ~8% of the amino groups, and *N*-hydroxysuccinimide is generated as a side product that can potentially adsorbs on the surface of CNH. Here **Y-CNH** was synthesized via an acid chloride since it gives higher functionalization on CNH and volatile SO_2 and HCl are the only side products that ca be easily removed under vacuum (Scheme 2-1).[7] Thus obtained conjugate **Y-CNH** is deposited onto a microgrid and observed in TEM.

Scheme 2-1. Functionalization of bromine-substituted Y-shaped rotor on CNH.

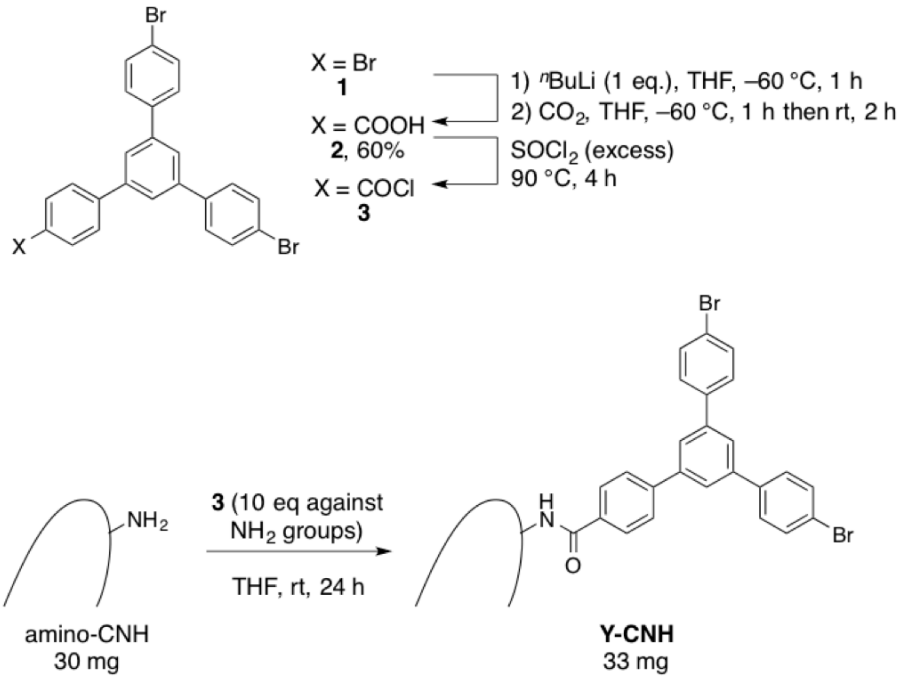

TEM images show the apparent C-C bond rotation in that depend on the beam current density. The existence of biphenyl rotor was confirmed by image simulation (Figure 2-9). SMART-TEM images of the same rotor at electron dose ranging from 5.1×10^3 to 5.1×10^4 electrons $Å^{-2}$ s^{-1} is shown in Figure 2-10 to Figure 2-12 and the apparent motion is summarized in Figure 2-13. The apparent motion decreased from 27 to 8 times out of 40 successive frames by 10-fold increase in the electron dose. This matches with the estimation from quantum mechanics simulation, and shows that the apparent motion is originating from the snapshotted quantum states of molecules.

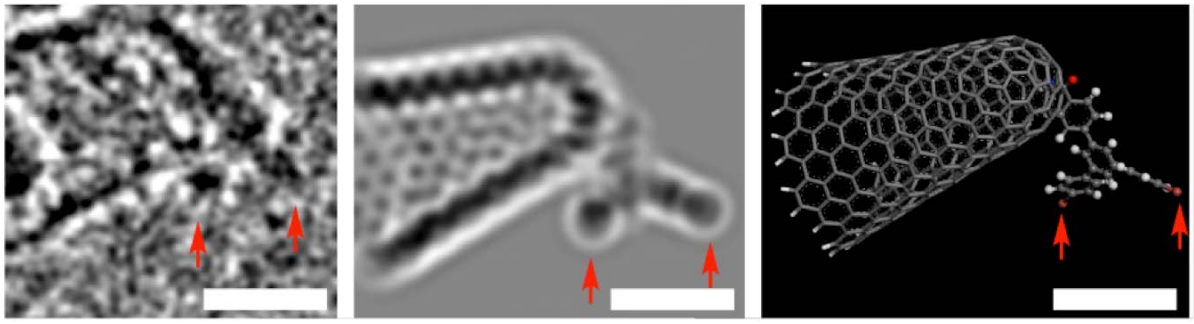

Figure 2-9. A TEM image and simulation of Y-shaped rotor on CNH taken at 5.1×10^3 electrons $Å^{-2}$ s^{-1} Images from left are processed TEM images after contrast inversion, bandpass filter and contrast modification, simulated image, and modeled structure, respectively. Red arrows indicate two Br atoms. Scale bars are 1 nm.

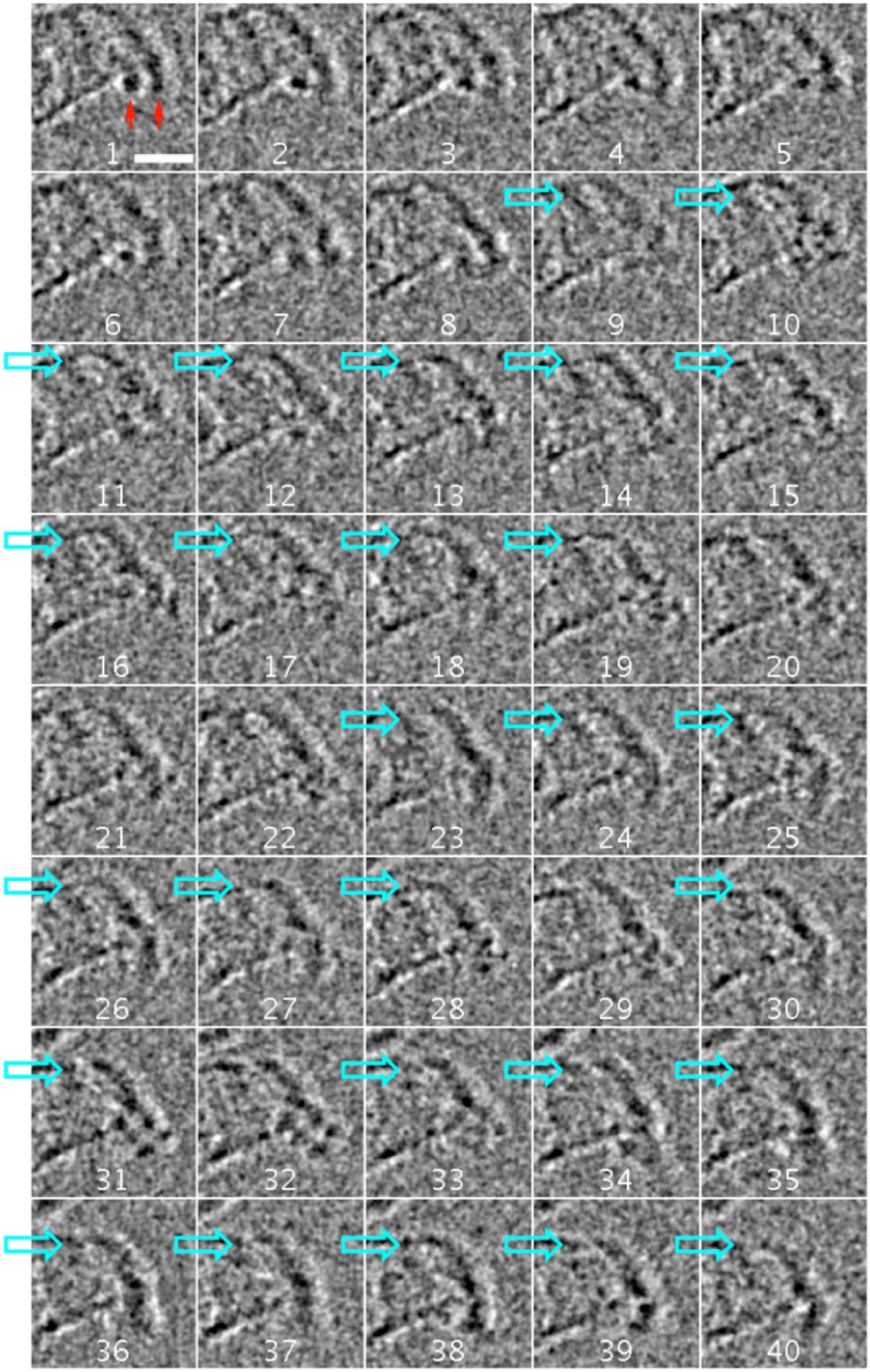

Figure 2-10. SMART-TEM images of Br-substituted biphenyl rotor on CNH taken at 120 kV, 5.1 × 10^3 electrons $Å^{-2}$ s^{-1}. Images were processed by contrast inversion, bandpass filter, and contrast modification. Red and blue arrows indicate two Br atoms and the apparent motion between the connected two frames, and white letters show frame number, respectively. Scale bar is 1 nm.

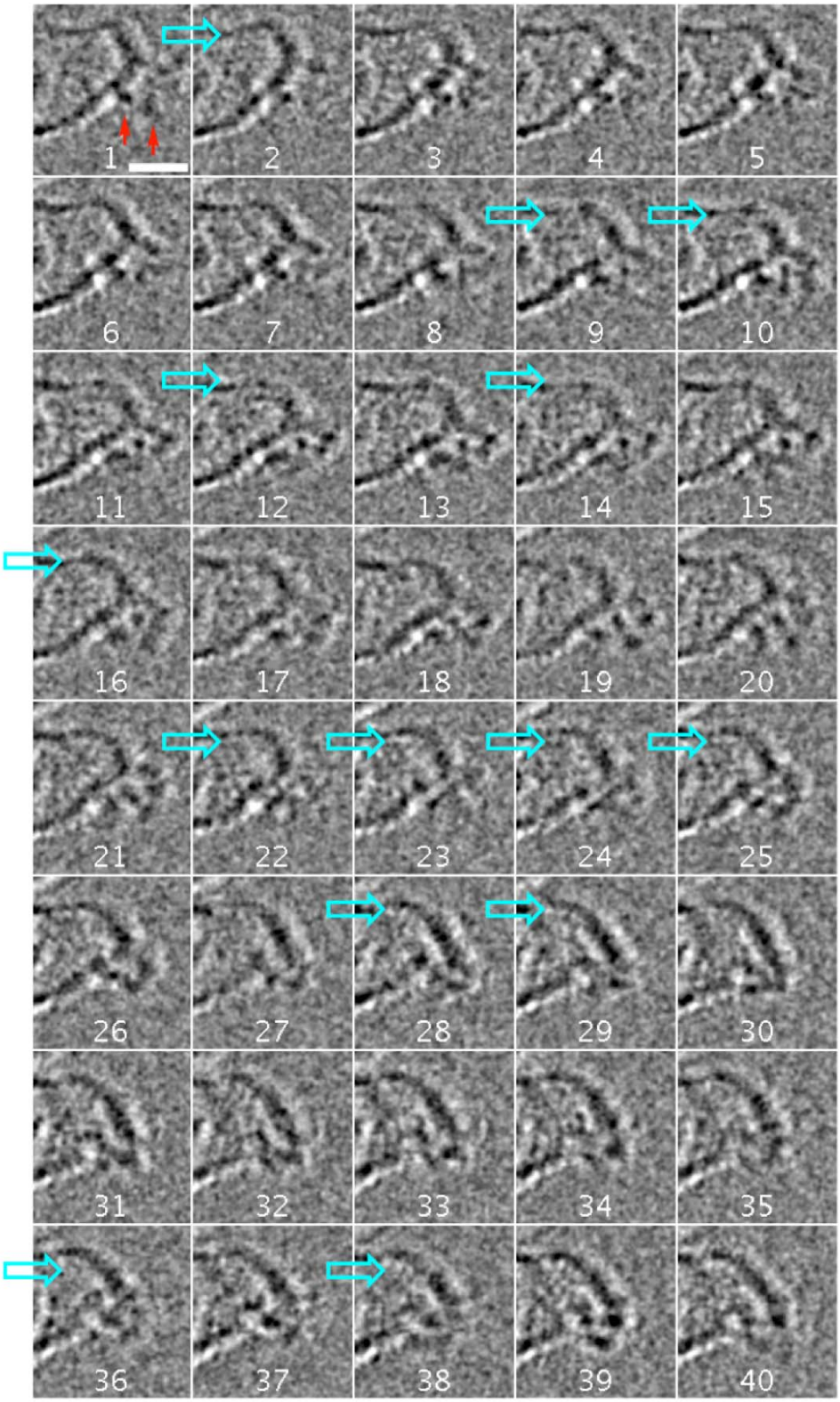

Figure 2-11. SMART-TEM images of Br-substituted biphenyl rotor on CNH taken at 120 kV, 1.5 × 10^4 electrons $Å^{-2}$ s^{-1}. Images were processed by contrast inversion, bandpass filter, and contrast modification. Red and blue arrows indicate two Br atoms and the apparent motion between the connected two frames, and white letters show frame number, respectively. Scale bar is 1 nm.

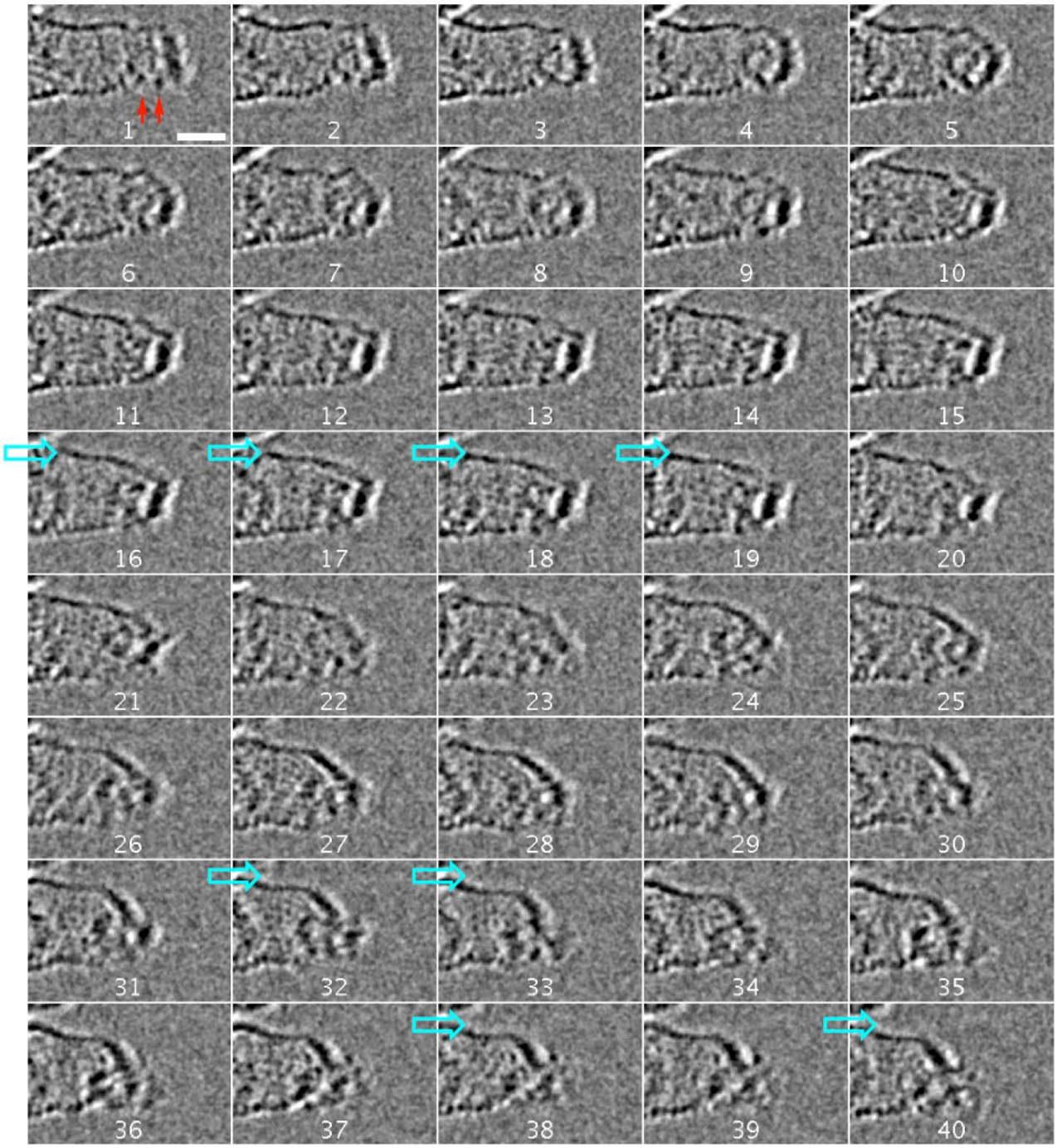

Figure 2-12. SMART-TEM images of Br-substituted biphenyl rotor on CNH taken at 120 kV, 5.1 × 10^4 electrons $Å^{-2}$ s^{-1}. Images were processed by contrast inversion, bandpass filter, and contrast modification. Red and blue arrows indicate two Br atoms and the apparent motion between the connected two frames, and white letters show frame number, respectively. Scale bar is 1 nm.

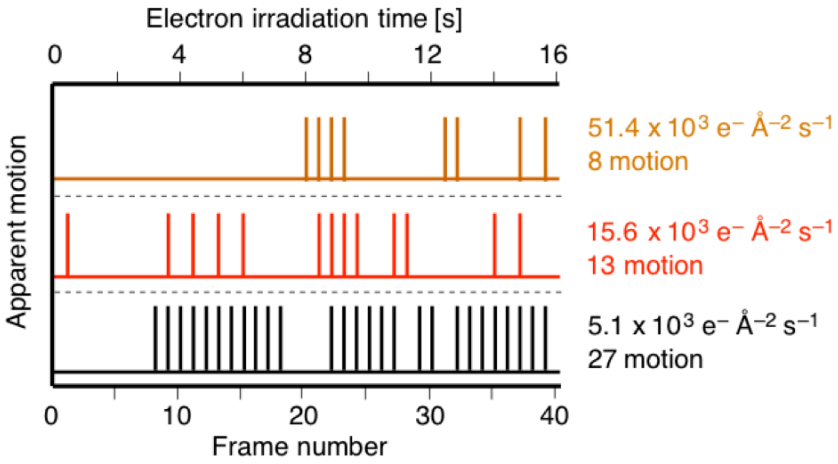

Figure 2-13. Appearance of apparent motions in SMART-TEM images of Br-substituted biphenyl rotor. Bars represent the apparent motion events.

2-6 Apparent Motion Frequencies of I-Substituted Biphenyl Rotor

In order to provide an additional proof that the quantum mechanics of internal rotor are imaged in TEM, iodine-substituted biphenyl rotor was also examined. The rotational inertia $g_{\theta\theta}$ was calculated using the coordinates obtained by B3LYP/6-31G(d) level of theory because higher split valence double zeta basis sets (e.g. 6-31G) are not applicable for iodine and thus not suitable for direct comparison of Br- and I-analogues. The substitution of bromine to iodine atoms increases $g_{\theta\theta}$ by 1.5 times from 9.3×10^3 to 13.9×10^3 Da Å^2. Eq. 2-4 suggests that large $g_{\theta\theta}$ give dense eigenstates and leads to increase the probability of the rotor to be found around equilibrium position. This means that iodine substitution is expected to decrease in apparent motion is expected. Thus iodine-substituted biphenyl rotor was synthesized in similar manner to the bromine analogue, attached onto CNH to afford **Y_I-CNH**, and observed in SMART-TEM (Scheme 2-2).

Scheme 2-2. Functionalization of iodine-substituted Y-shaped rotor on CNH.

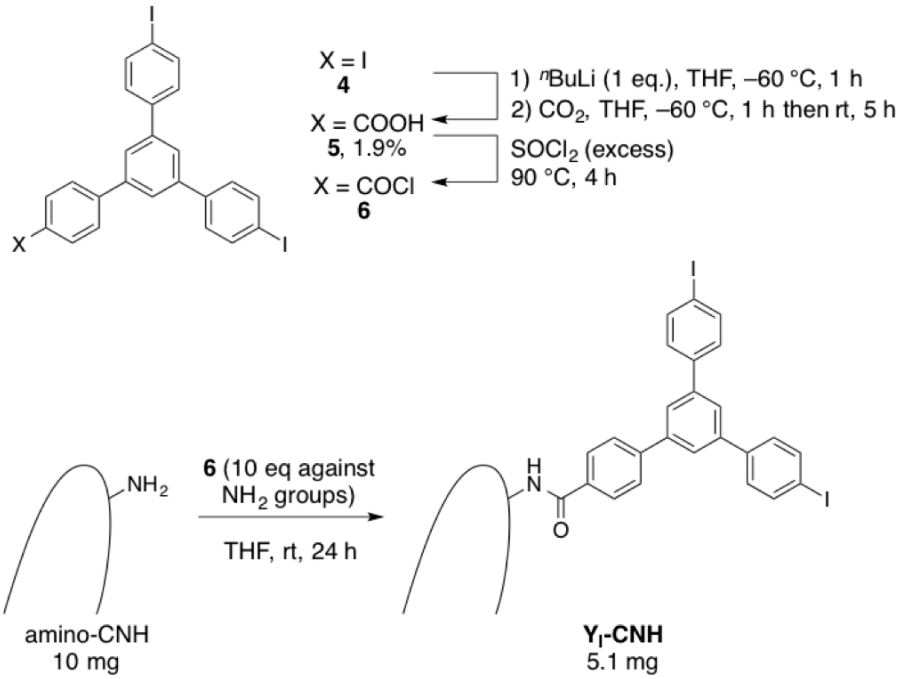

TEM images show less apparent C-C bond rotation in SMART-TEM (Figure 2-14–Figure 2-17). When the electron dose was increased from 6.4×10^3 to 5.1×10^4 electrons $Å^{-2}$ s^{-1}, the number of apparent motion decreased from 6 to 4. The apparent motion frequencies of I-substituted rotor was fewer than that of Br-substituted rotor (8 apparent motions at 5.1×10^4 electrons $Å^{-2}$ s^{-1}). This decrease in apparent motion qualitatively matches with the assumption based on quantum mechanics.

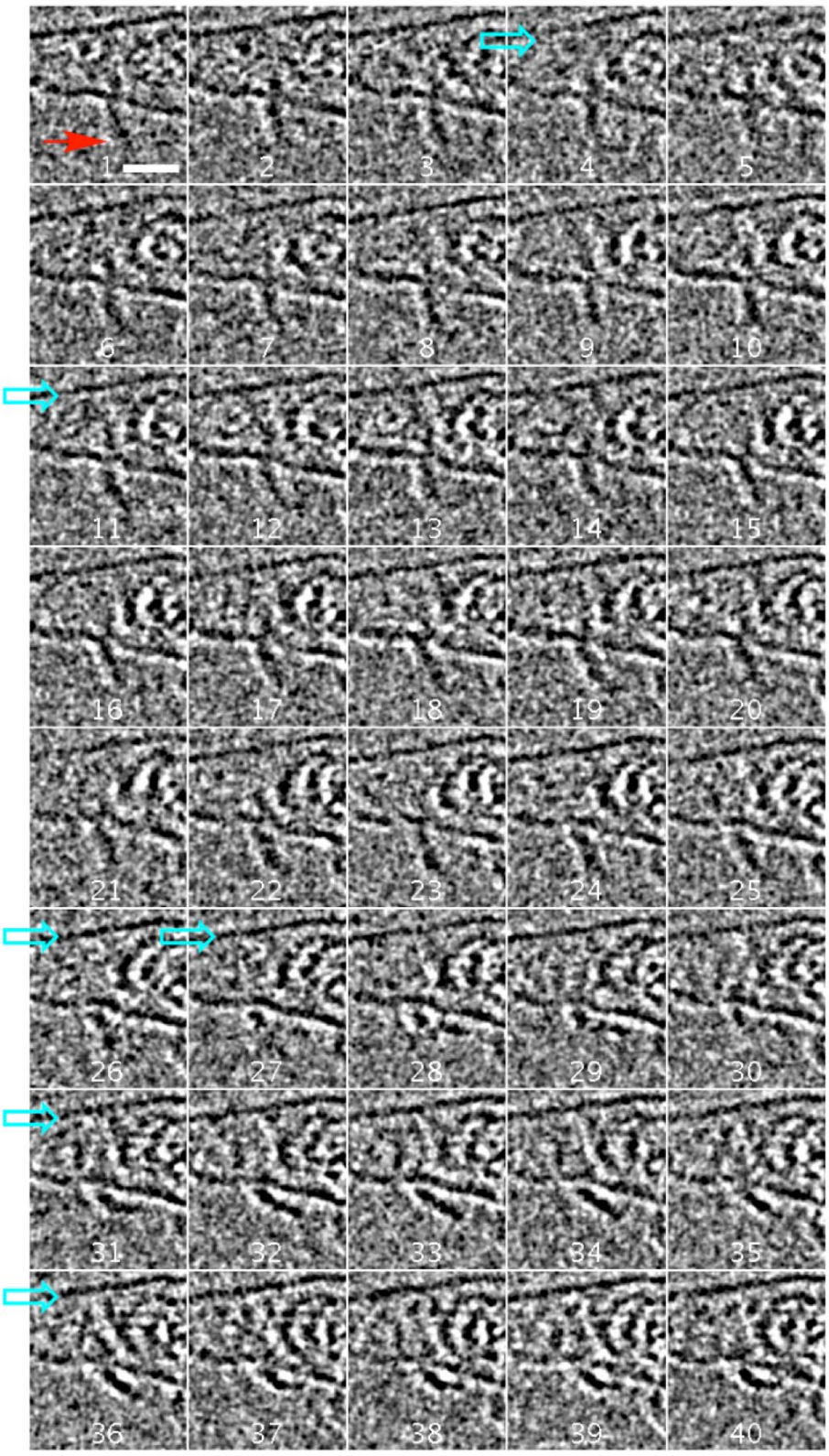

Figure 2-14. SMART-TEM images of I-substituted biphenyl rotor on CNH taken at 120 kV, 6.4 × 10^3 electrons $Å^{-2}$ s^{-1}. Images were processed by contrast inversion, bandpass filter, and contrast modification. Red and blue arrows indicate overlapped I atoms and the apparent motion between the connected two frames, and white letters show frame numbers, respectively. Scale bar is 1 nm.

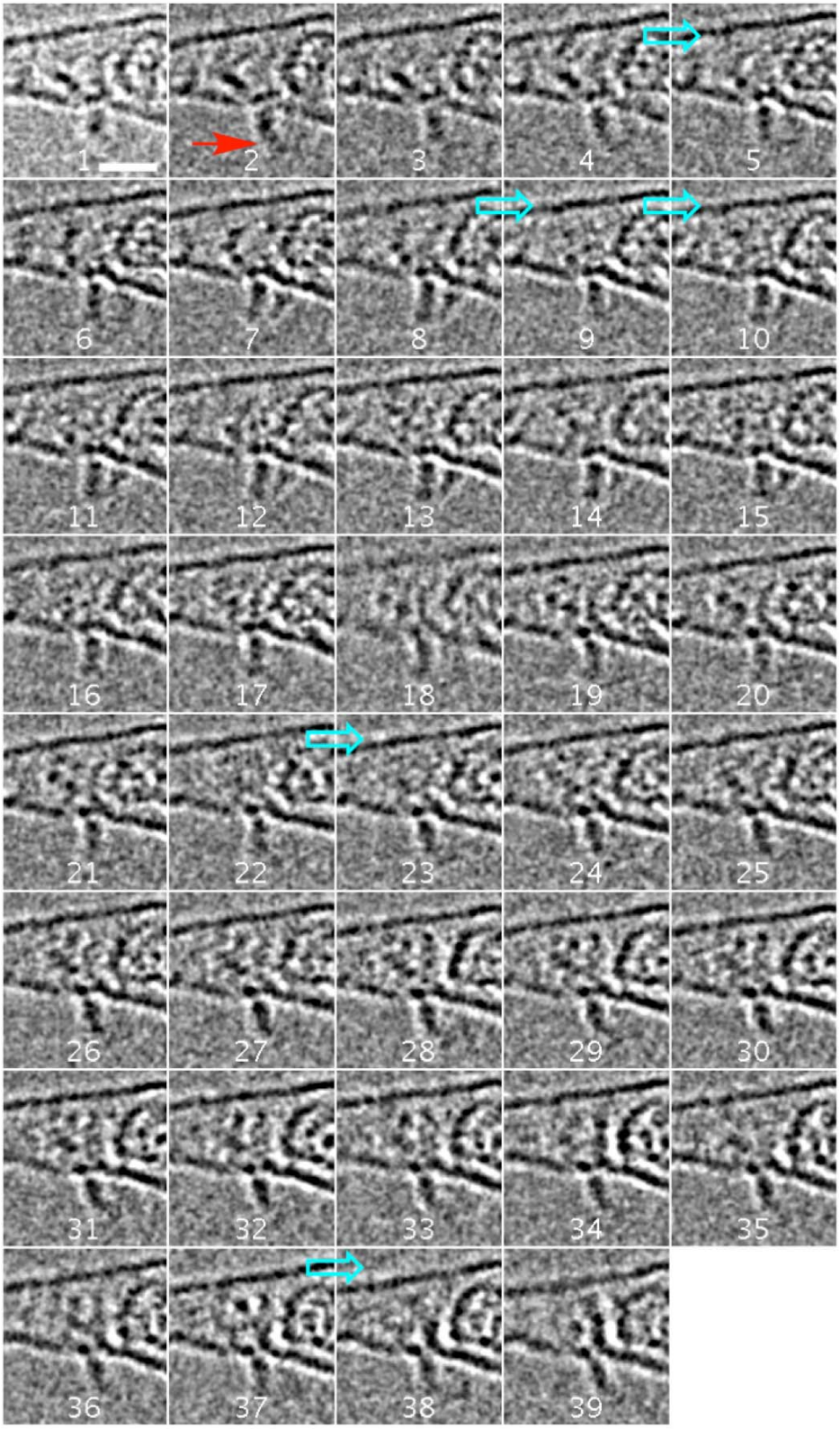

Figure 2-15. SMART-TEM images of I-substituted biphenyl rotor on CNH taken at 120 kV, 1.9 × 10^4 electrons $Å^{-2}$ s^{-1}. Images were processed by contrast inversion, bandpass filter, and contrast modification. Red and blue arrows indicate overlapped I atoms and the apparent motion between the connected two frames, and white letters show frame numbers, respectively. Scale bar is 1 nm.

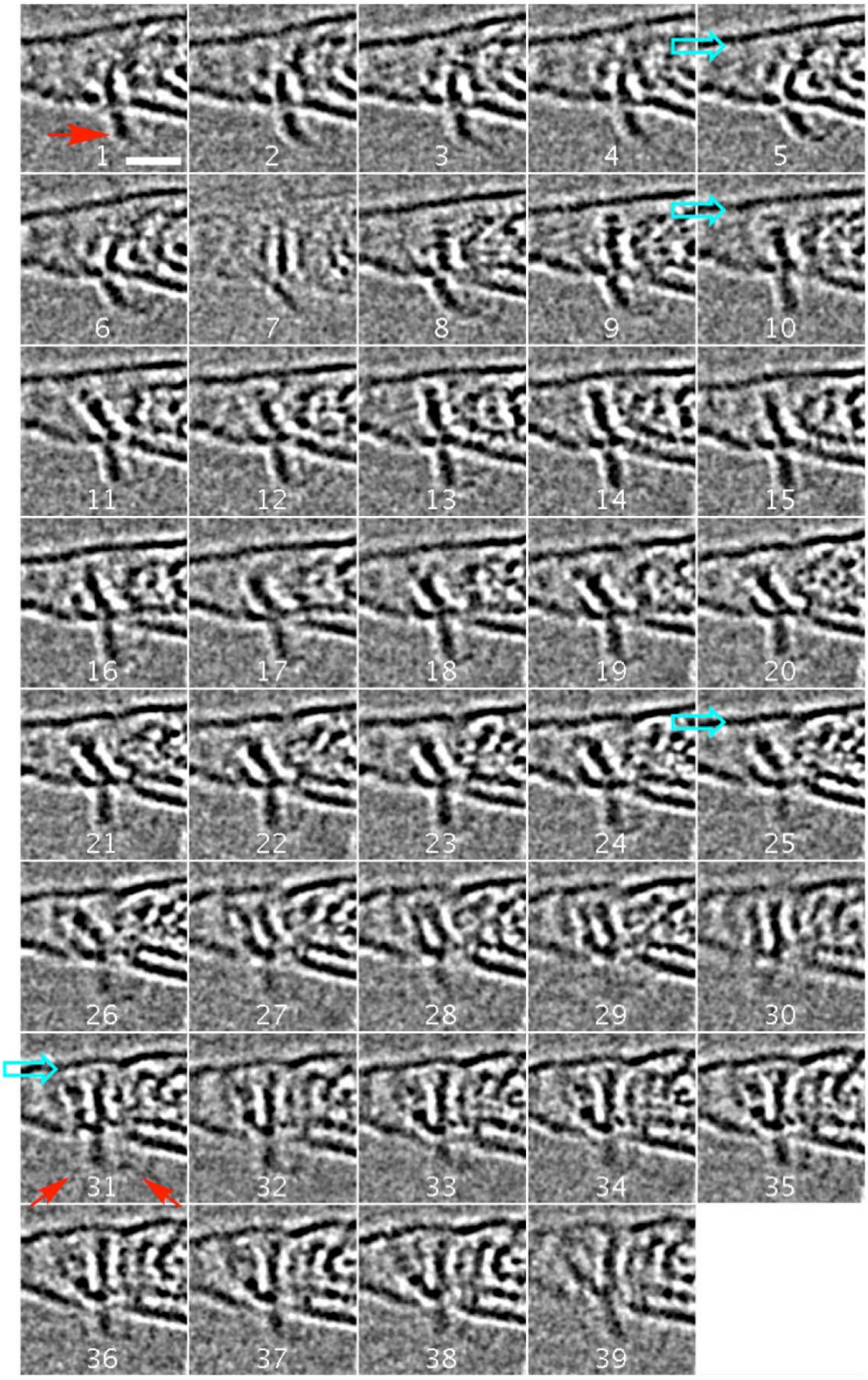

Figure 2-16. SMART-TEM images of I-substituted biphenyl rotor on CNH taken at 120 kV, 5.8 × 10^4 electrons $Å^{-2}$ s^{-1}. Images were processed by contrast inversion, bandpass filter, and contrast modification. Red and blue arrows indicate overlapped I atoms and the apparent motion between the connected two frames, and white letters show frame numbers, respectively. Scale bar is 1 nm.

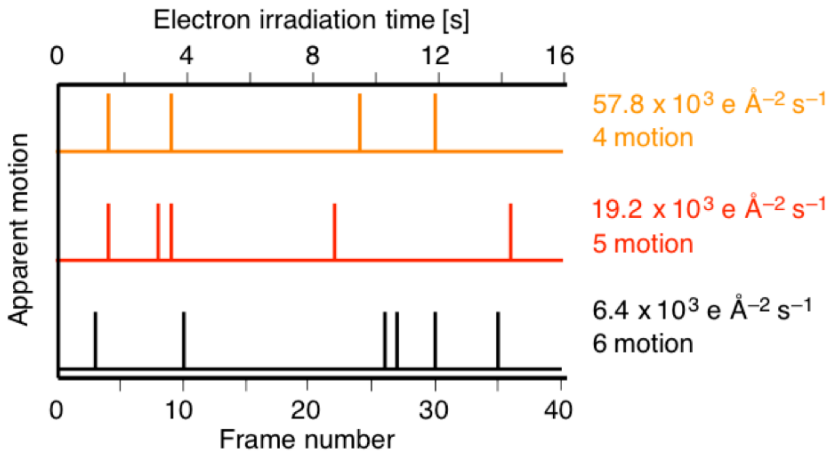

Figure 2-17. Appearance of apparent motions in SMART-TEM images of I-substituted biphenyl rotor. Bars represent the apparent motion events.

2-7 Conclusion

In summary, I have shown that the apparent motion in SMART-TEM movies are the consequence of the deviation of quantum mechanical motion sampled by electron beam. The electron-sample interactions within the order of 10^{-17} sec are significantly faster than that of C-C bond rotation, and each irradiated electron snapshots the atom position of the specimen molecules. Thus obtained information of the molecules from interacted electrons is accumulated within a single frame to construct a TEM image. The probability to acquire multiple electrons with information on the similar atomic position is proportional to the total number of electrons, and sharp images are obtained at high electron dose. From the viewpoint of SMART-TEM imaging, the probability density of the atom position can be regarded as an inevitable factor that causes blurring. Most of the organic molecules possess free-rotating bonds or ring structures with conformational flexibility such as alkyl chains and cyclohexane rings, respectively, and their quantum mechanical motion inevitably generates blurring. This in turn implies the possibility to apply the degree of blurring as a tool to discuss the mobility and flexibility of molecules and chemical bonds.

2-8 Experimental Section

General.

All reactions were carried out in a dry reaction vessel under nitrogen or argon. The reactions were traced by analytical thin-layer chromatography was performed on glass plates coated with 0.25 mm 230–400 mesh silica gel containing a fluorescent indicator (Merck). Flash silica gel column chromatography was performed on silica gel 60N (Kanto, spherical and neutral, 140–325 mesh) as described by Still.[13] Gel permeation column chromatography was performed on a Japan Analytical Industry LC-9260 II NEXT (eluent: chloroform) with JAIGEL 1H and 2H polystyrene columns. NMR spectra were measured on JEOL ECX-400 and ECA-500 spectrometers and reported in parts per million from the reference peaks. ^{1}H NMR spectra in $CDCl_3$ were referenced internally to tetramethylsilane as a standard, and ^{1}H NMR spectra in DMSO and ^{13}C NMR spectra to the solvent resonance. Methyl, methylene, and methyne signals in ^{13}C NMR spectra were assigned by DEPT spectra. High-resolution mass spectra (HRMS) were acquired by atmospheric pressure ionization (APCI) using a time-of-flight mass analyzer on Bruker micrOTOF spectrometer with a calibration standard of polyethylene glycol (MW 600). Quantum chemical calculation was carried out on a Gaussian 09 package at MP2/6-31G(d,p) (for bond rotation) or B3LYP/3-21G(d) (for calculation of rotational inertia) level of theory.[14] Frequency calculation ensured the existence of all the structures as local minimums (no imaginary frequencies) or transition state (only one imaginary frequency), and coordinate scan followed by energy minimization of the forward and backward conformational isomers further confirmed that the obtained transition state is involving in the bond rotation. Thermodynamic parameters were calculated at 298.15 K, 1 atm. SMART-TEM imaging was performed on JEM-ARM200F equipped with a thermal field-emission gun, CEOS CETCOR aberration-corrector, and GATAN Ultrascan CCD camera, and a double-tilt sample holder operated at 10^{-5} Pa, 293 K, 120-kV acceleration voltage and spherical aberration C3 = –10 μm, C5 = –1 mm. Sequential images were obtained at 1024 × 1024 pixels resolution in ×2.0 M magnification with the exposure time of 0.4 sec followed by data readout of 0.79 sec. SMART-TEM image analyses were performed on ImageJ software. TEM images were simulated by xHREM 4.0 software using Cartesian coordinated of molecular models constructed on a Materials Studio 8.0 software.

Materials.

Unless otherwise noted, materials were purchased from Tokyo Kasei Co., Aldrich Inc., and other commercial suppliers and used after appropriate purification before use. Carbon nanohorn

(batch #131-3-1) was purchased from Nippon Denki Co., Ltd. and used as received. Carbon-supported copper microgrid was purchased from Okenshoji Co., Ltd. Gaseous ammonia was purchased from Jyotou Gas. Co., Ltd. and dried with solid NaOH column before introduction to a reaction vessel.

1,3,5-Tris(4-bromophenyl)benzene (1)[15]

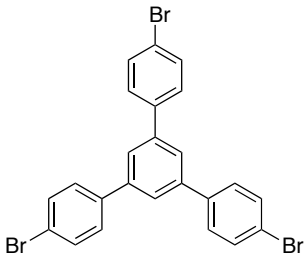

To a solution of 4´-bromoacetophenone (30.0 g, 151 mmol) in ethanol (200 mL) in a 500-mL 2-neck round-bottom flask, silicon tetrachloride (50.5 g, 297 mmol, 2.00 equiv) was added dropwise over 20 min at room temperature with vigorous stirring. The colorless solution gradually turned into yellow then orange, and yellowish precipitates were formed. The reaction mixture was stirred for 5 h at room temperature. Water (100 mL) was added to the mixture and the resulting suspension was immediately extracted four times with dichloromethane (150 mL). Combined organic phase was concentrated under vacuum and recrystallized from dichloromethane/methanol to obtain pinky needle solid (19.9 g, 73%). ^{1}H NMR (500 MHz, $CDCl_3$) δ 7.54 (d, 6H, J = 8.6 Hz), 7.61 (d, 6H, J = 8.6 Hz), 7.69 (s, 3H) and matched with the published report. mp 257–258 °C (needle crystals). The title compound can be further purified by sublimation (190 °C, 0.8–2 x 10^{-2} Torr) if necessary.

4´´-Bromo-5´-(4-bromophenyl)-[1,1´:3´,1´´-terphenyl]yl-4-carboxylic acid (2)[9]

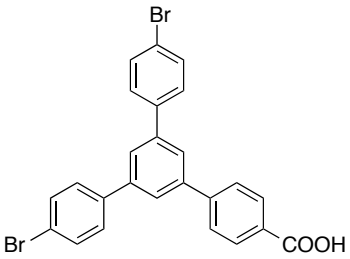

1,3,5-Tris(4-bromophenyl)benzene (1.09 g, 2.00 mmol, 2.00 eq) was dissolved in THF (40 mL) in a 100-mL 2-neck flask was cooled to –60 °C in $CHCl_3$/dry ice bath. 1.52 M BuLi in THF (0.658 mL, 1.00 mmol) was added dropwise to the solution over 5 min and stirred at –60 °C. After stirring for 1 hour, CO_2 gas dried over $CaCl_2$ tube was bubbled into the mixture for 3 hours. The reaction mixture was warmed to room temperature and stirred for 30 min. 3M aqueous HCl (10 mL) was added to the mixture and the resulting suspension was extracted three times with ethyl

acetate (50 mL). Combined organic phase was washed with brine, dried over $MgSO_4$, and concentrated under vacuum. The crude material was purified by silica gel column chromatography (eluent: CH_2Cl_2 to separate **Y** and other impurities, then ethyl acetate) to give the title compound (289 mg, 57%) as a colorless solid with a mixture of 4''-bromo-5'-phenyl-[1,1':3',1''-terphenyl] -4-carboxylic acid. ^{1}H NMR (500 MHz, $CDCl_3$) δ 7.56 (d, 4H, *J* = 8.6 Hz), 7.62 (d, 4H, *J* = 8.6 Hz), 7.74 (s, 1H), 7.78 (s, 2H), 7.78 (d, 2H, *J* = 8.3 Hz), 8.22 (d, 2H, *J* = 8.3 Hz). ^{1}H NMR (500 MHz, DMSO-d_6) δ 7.69 (d, 4H, *J* = 8.6 Hz), 7.87 (d, 4H, *J* = 8.6 Hz), 7.95 (d, 1H , $^4J_{HH}$ = 1.5 Hz), 7.98 (d, 2H, $^4J_{HH}$ = 1.5 Hz), 8.00 (d, 2H, *J* = 8.3 Hz), 8.04 (d, 2H, *J* = 8.3 Hz). These values matched with the published report. mp 200–205 °C (powder, decomposed). The title compound can be further purified by sublimation (200 °C, 0.8–2 x 10^{-2} Torr).

Note: Increase in the amount of BuLi results in di-carboxylation, which is difficult to separate by column chromatography.

1,3,5-Tris(4-iodophenyl)benzene (4)[16]

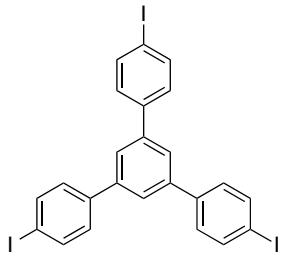

To a solution of 4´-iodoacetophenone (5.06 g, 21 mmol) in ethanol (6 mL) in a 30-mL 2-neck round-bottom flask, $SOCl_2$ (5.15 g, 43 mmol, 2.1 eq) was added dropwise with stirring over 20 min. The solution color changed from brown suspension to dark red solution upon addition. The reaction mixture was heated to 80 °C and refluxed for 1.5 h. The reaction mixture was poured into saturated $NaHCO_3$ aq, extracted with dichloromethane, (30 mL) twice, and the organic layer was washed with water (10 mL), filtered, and concentrated under vacuum. The dark red solid was dissolved in minimum amount of dichloromethane, and methanol was added slowly to form precipitate. The precipitate was filtered, washed with methanol, and dried under vacuum to obtain the title compound (3.43 g, 73%) as a brown solid. ^{1}H NMR ($CDCl_3$, 500 MHz) δ 7.40 (6H, d, *J* = 8.2 Hz), 7368 (s, 3H), 7.81 6H, d, *J* = 8.2 Hz) and matched with the published report. HRMS (APCI+) $C_{24}H_{15}I_3$ $[M]^+$ Calcd 683.8302 found 683.8307.

4´´-Iodo-5´-(4-iodophenyl)-[1,1´:3´,1´´-terphenyl]yl-4-carboxylic acid (5)

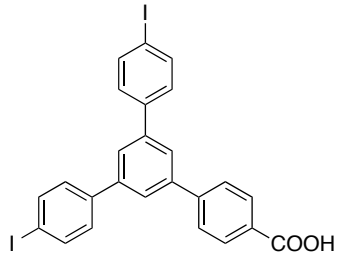

A solution of 1,3,5-tris(4-iodophenyl)benzene (1.64 g, 2.40 mmol, 1.2 eq) in THF (50 mL) in a 100-mL 2-neck round-bottom flask was cooled down to –60 °C in $CHCl_3$/dry ice bath. To this solution ^{n}BuLi in THF (1.51 M, 1.33 mL, 2.00 mmol) was added dropwise using a syringe pump over 20 min and stirred for 1 h. During addition, the red solution became dark red. CO_2 gas was bubbled and stirred for 1 h, and then the reaction vessel was allowed to heat to rt with bubbling. After 5 h, 1 M HCl aq was added to quench the reaction. The mixture was added ethyl acetate (20 mL), washed with brine (20 mL) three times, and the organic layer was dried over $MgSO_4$, filtered, and concentrated under vacuum to obtain the crude product. The crude in toluene was passed through a pad of silica gel to elute tris(4-iodophenyl)benzene and other impurities, then ethyl acetate was eluted, concentrated under vacuum followed by GPC to obtain the title compound as a white solid (27 mg, 1.9%). ^{1}H NMR (DMSO-d_6, 400 MHz) δ 7.70 (4H, d, J = 8.5 Hz), 7.85 (4H, d, J = 8.5 Hz), 7.92 (1H, t, $^4J_{HH}$ = 1.5 Hz), 7.96 (2H, d, $^4J_{HH}$ = 1.5 Hz), 8.00 (2H, d, J = 8.4 Hz), 8.04 (2H, d, J = 8.4 Hz). ^{13}C (DMSO-d_6, 100 MHz) δ 94.43 (2C), 124.72 (1C, CH), 124.74 (2C, CH), 127.38 (2C, CH), 129.46 (4C, CH), 129.89 (2C, CH), 130.12 (1C), 137.66 (4C, CH), 139.26 (2C), 140.71 (1C), 140.71 (2C), 143.90 (1C), 137.19 (1C). MS (APCI+) $C_{25}H_{17}O_2I_2$ $[M+H]^+$ Calcd 602.9234 found 602.9232.

Amino-CNH

The amount of reagents was modified from the previous report to ensure high functionalization.[17] To a dispersion of CNH (501 mg) in liquid ammonia (800 mL) in a 2-L three-necked round-bottom flask equipped with dry ice condenser at –78 °C, sodium amide (501 mg) was added and stirred for 10 min. The reaction mixture was refluxed (–33 °C) for 3 h in a flask equipped with a dry-ice condenser. A black solid was obtained after removal of ammonia at room temperature under dried condition with solid NaOH columns. The crude material was dispersed in water (50 mL), washed with a saturated NH_4Cl aq (250 mL) then ten times with milliQ (50 mL) and dried under vacuum to obtain amino-CNH (523 mg) as a black solid. The obtained amino-CNH dispersion in water (0.1 mg/mL) prepared by one-minute sonication was stable for days.

The amount of amino group was determined by UV/Vis measurement of a

2,4-dinitrophenyl adduct. Briefly, amino-CNH (5.00 mg) and 1-fluoro-2,4-dinitro- benzene (500 mg) in ethanol (50 μL) and 0.1 M aqueous solution of $NaHCO_3$ (100 μL) in an Schlenck tube was heated at 60 °C for 10 min, filtered on a PTFE membrane filter (0.2-μm pore), washed with methanol (40 mL), dichloromethane (15 mL), and methanol (15 mL), and dried under vacuum. The UV/Vis spectrogram of 1.00 mg/mL dispersion in water has a peak at 355 nm with a broad background originating from Mie scattering from CNH, and the intensity from 2,4-dinitrophenyl group was calculated by subtracting background. The amount of amino group was determined to be 110 nmol/mg using the molar absorption coefficient $\varepsilon = 1.7 \times 10^3\ M^{-1}\ cm^{-1}$.[18]

Bromine-substituted rotor on carbon nanohorn

To 4´´-bromo-5´-(4-bromophenyl)-[1,1´:3´,1´´-terphenyl]ylcarboxyl acid (28 mg, 55 μmol) in a Schlenck tube, $SOCl_2$ (0.67 g, 5.65 mmol, 103 eq) was added, sealed, stirred and heated at 90 °C for 4 h under argon atmosphere. The solution became wine red upon heating. $SOCl_2$ was evaporated to obtain an orange solid. Amino-CNH (110 nmol/mg NH_2 groups, 30 mg) dispersion in THF (10 mL) was added and stirred for 24 h, filtered, and washed with toluene to obtain the title material as a black solid (26 mg).

Iodine-substituted rotor on carbon nanohorn

To 4´´-iodo-5´-(4-iodophenyl)-[1,1´:3´,1´´-terphenyl]ylcarboxyl acid (4.6 mg, 7.6 μmol) in a Schlenck tube, $SOCl_2$ (0.11 g, 0.92 mmol) was added, sealed, stirred and heated at 90 °C for 4 h under argon atmosphere. The solution became wine red upon heating. $SOCl_2$ was evaporated to obtain an orange solid. Amino-CNH (110 nmol/mg NH_2 groups, 10 mg) dispersion in THF (3 mL) was added and stirred for 24 h, filtered, and washed with toluene to obtain the title material as a black solid (5.1 mg).

Sample preparation for TEM imaging

TEM samples were dispersed in methanol by five times repeated sonication for 2 sec in a sonication bath, 2 μL was placed on a TEM microgrid NS-C15 (Okenshoji Co., Ltd.), blotted from the backside of the grid by a filter paper, and dried in a grease-free desiccator under $< 10^{-2}$ Torr for more than 2 h.

SMART-TEM imaging

TEM samples were observed under aberration-corrected condition with negative C3 and overfocus so that high contrast is achieved.[19] The molecules were searched at the dose rate of 5–20 $\times 10^4$ electrons $Å^2\ s^{-1}$ and then set the dose rate to ca. 5×10^4 electrons $Å^2\ s^{-1}$. After manual image acquisition for 40 frames, the dose rate was increased to ca. 15×10^4 electrons $Å^2\ s^{-1}$ by narrowing

the beam diameter. After manual image acquisition for 40 frames, the dose rate was increased to ca. 50×10^4 electrons Å^2 s^{-1} by narrowing the beam diameter. Finally the dose rate was recovered to 5–20×10^4 electrons Å^2 s^{-1} to search another molecule.

The obtained images were processed in ImageJ. The images were converted to a stacked movie, image shift was corrected by Stackreg plugin, and the target part was cropped. The cropped image was treated with bandpass filter to remove noise, contrast was inverted for visibility, and the contrast and brightness were modified.

Note: **Classical mechanical assumption on the molecular motion based on quantum mechanical parameters**

In Rice-Ramsperger-Kassel-Marcus theory, the rate constant k_{rot} for C-C bond rotation is expressed as

$$k_{\mathrm{rot}} = \frac{k_B T}{h} \frac{q_{\ddagger}}{q_i} \exp\left(-\frac{\epsilon_0^*}{k_B T}\right) \qquad \text{(eq.2-6)}$$

where $q_{\ddagger}$ and q_{i} are partition functions for transition state and initial state, respectively, and ε_0^* is the difference in zero-point energy for the rotation, $q_{\ddagger}$, q_{i} and ε_0^* are calculated to be 9.13×10^{14}, 2.52×10^{15}, and 1.29×10^{-20} J/molecule, respectively.[20] These values give

$$k_{\mathrm{rot}} = 2.03 \times 10^{11} [\mathrm{s}^{-1}] \qquad \text{(eq.2-7)}$$

and this value is consistent with the conclusion given in section 1.2.1 based on Eyring equation.

Calculation results.

1) Bond rotation energies (Figure 2-2)

Biphenyl (**Figure 2-18**)

MP2/6-31G(d,p)

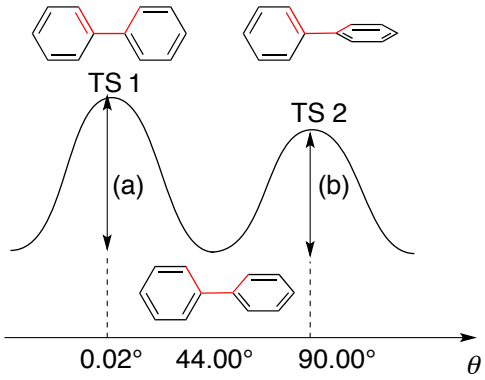

	$\Delta H^{\ddagger}$ [kJ mol^{-1}]	$\Delta G^{\ddagger}$ [kJ mol^{-1}]
(a)	8.31	13.71
(b)	5.82	10.23

Figure 2-18. An energy diagram for C-C bond rotation of biphenyl. Horizontal axis indicates the dihedral angle of the atoms shown in red color.

Ground state

SCF Done: E(RHF) = -460.269824947 A.U. after 9 cycles

Center Number	Atomic Number	Atomic Type	Coordinates (Angstroms) X	Y	Z
1	6	0	0.000000	0.000000	-0.738609
2	6	0	-0.452423	1.119889	-1.453294
3	6	0	-0.449307	1.120639	-2.847832
4	6	0	0.000000	0.000000	-3.549464
5	6	0	0.449307	-1.120639	-2.847832
6	6	0	0.452423	-1.119889	-1.453294
7	6	0	0.000000	0.000000	0.738609
8	6	0	0.452423	1.119889	1.453294
9	6	0	0.449307	1.120639	2.847832
10	6	0	0.000000	0.000000	3.549464
11	6	0	-0.449307	-1.120639	2.847832
12	6	0	-0.452423	-1.119889	1.453294
13	1	0	-0.827877	1.979253	-0.910576
14	1	0	-0.807402	1.989461	-3.386034
15	1	0	0.000000	0.000000	-4.632055
16	1	0	0.807402	-1.989461	-3.386034
17	1	0	0.827877	-1.979253	-0.910576
18	1	0	0.827877	1.979253	0.910576
19	1	0	0.807402	1.989461	3.386034
20	1	0	0.000000	0.000000	4.632055
21	1	0	-0.807402	-1.989461	3.386034
22	1	0	-0.827877	-1.979253	0.910576

Transition state 1 (TS1)

SCF Done: E(RHF) = -460.267374285 A.U. after 14 cycles

Center Number	Atomic Number	Atomic Type	Coordinates (Angstroms) X	Y	Z
1	6	0	0.000000	0.000000	0.742125
2	6	0	-0.854459	0.854477	1.452165
3	6	0	-0.854253	0.854271	2.847684
4	6	0	0.000000	0.000000	3.547886
5	6	0	0.854253	-0.854271	2.847684
6	6	0	0.854459	-0.854477	1.452165
7	6	0	0.000000	0.000000	-0.742125
8	6	0	-0.854459	-0.854477	-1.452165
9	6	0	-0.854253	-0.854271	-2.847684
10	6	0	0.000000	0.000000	-3.547886
11	6	0	0.854253	0.854271	-2.847684
12	6	0	0.854459	0.854477	-1.452165
13	1	0	-1.515760	1.515792	0.904989
14	1	0	-1.518271	1.518305	3.386936
15	1	0	0.000000	0.000000	4.630488
16	1	0	1.518271	-1.518305	3.386936
17	1	0	1.515760	-1.515792	0.904989
18	1	0	-1.515760	-1.515792	-0.904989
19	1	0	-1.518271	-1.518305	-3.386936
20	1	0	0.000000	0.000000	-4.630488
21	1	0	1.518271	1.518305	-3.386936
22	1	0	1.515760	1.515792	-0.904989

Transition state 2 (TS2)

SCF Done: E(RHF) = -460.264464851 A.U. after 8 cycles

Center Number	Atomic Number	Atomic Type	Coordinates (Angstroms) X	Y	Z
1	6	0	0.000000	0.000000	-0.744870
2	6	0	-0.000174	1.199907	-1.479790
3	6	0	-0.000163	1.201048	-2.873552
4	6	0	0.000000	0.000000	-3.582378
5	6	0	0.000163	-1.201048	-2.873552
6	6	0	0.000174	-1.199907	-1.479790
7	6	0	0.000000	0.000000	0.744870
8	6	0	0.000174	1.199907	1.479790
9	6	0	0.000163	1.201048	2.873552
10	6	0	0.000000	0.000000	3.582378
11	6	0	-0.000163	-1.201048	2.873552
12	6	0	-0.000174	-1.199907	1.479790
13	1	0	-0.000520	2.154108	-0.972427
14	1	0	-0.000310	2.145261	-3.403817
15	1	0	0.000000	0.000000	-4.664829
16	1	0	0.000310	-2.145261	-3.403817
17	1	0	0.000520	-2.154108	-0.972427
18	1	0	0.000520	2.154108	0.972427
19	1	0	0.000310	2.145261	3.403817
20	1	0	0.000000	0.000000	4.664829
21	1	0	-0.000310	-2.145261	3.403817
22	1	0	-0.000520	-2.154108	0.972427

***N*-Methyl benzamide (Figure 2-19)**

MP2/6-31G(d,p)

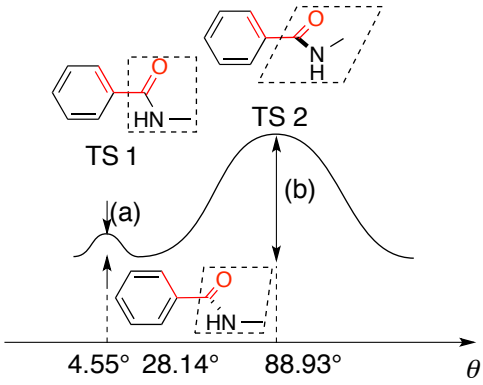

	$\Delta H^{\ddagger}$ [kJ mol^{-1}]	$\Delta G^{\ddagger}$ [kJ mol^{-1}]
(a)*	1.93	5.01
(b)	12.28	9.42

**Note*: almost no conformational change

Figure 2-19. An energy diagram for aryl C-carbonyl C bond rotation in *N*-methyl benzamide. Horizontal axis indicates the dihedral angle of the atoms shown in red color.

Ground state

SCF Done: E(RHF) = -437.532874045 A.U. after 7 cycles

Center Number	Atomic Number	Atomic Type	Coordinates (Angstroms) X	Y	Z
1	6	0	0.791982	-1.162869	-0.257472
2	6	0	0.240523	0.110518	-0.064162
3	6	0	1.080263	1.201731	0.187083
4	6	0	2.458376	1.015968	0.271286
5	6	0	3.007783	-0.256706	0.093655
6	6	0	2.173522	-1.342400	-0.178381
7	1	0	0.152013	-2.000036	-0.508122
8	1	0	0.634593	2.180588	0.304988
9	1	0	3.104941	1.860510	0.473509
10	1	0	4.079200	-0.399104	0.155693
11	1	0	2.598554	-2.325196	-0.338900
12	6	0	-1.231206	0.371918	-0.143622
13	8	0	-1.690024	1.460900	-0.501550
14	7	0	-2.031897	-0.685292	0.197770
15	1	0	-1.618097	-1.422236	0.744675
16	6	0	-3.470377	-0.505792	0.259502
17	1	0	-3.949483	-1.481567	0.256156
18	1	0	-3.780310	0.047102	1.148050
19	1	0	-3.783140	0.055575	-0.615372

Transition state 1 (TS 1)

SCF Done: E(RHF) = -437.531523513 A.U. after 10 cycles

Center Number	Atomic Number	Atomic Type	Coordinates (Angstroms) X	Y	Z
1	6	0	-1.090858	1.199045	-0.029468
2	6	0	-0.242964	0.084585	0.002093
3	6	0	-0.804243	-1.199472	0.035796
4	6	0	-2.189994	-1.360940	0.030614
5	6	0	-3.029007	-0.246481	-0.004702
6	6	0	-2.473757	1.034550	-0.035106
7	1	0	-0.638335	2.180941	-0.047994
8	1	0	-0.186798	-2.088943	0.064906
9	1	0	-2.612964	-2.357208	0.057268
10	1	0	-4.103777	-0.376157	-0.008315
11	1	0	-3.118624	1.903804	-0.061981
12	6	0	1.233113	0.371910	0.010924
13	8	0	1.663476	1.528957	0.074968
14	7	0	2.076471	-0.695178	-0.094488
15	1	0	1.716027	-1.628028	-0.007683
16	6	0	3.510038	-0.495849	-0.003883
17	1	0	3.838453	-0.334809	1.024201
18	1	0	4.013236	-1.369851	-0.409387
19	1	0	3.775709	0.380746	-0.586943

Transition state 2 (TS 2)

SCF Done: E(RHF) = -437.526092584 A.U. after 6 cycles

Center Number	Atomic Number	Atomic Type	Coordinates (Angstroms) X	Y	Z
1	6	0	-0.928285	-1.211384	0.059473
2	6	0	-0.235011	-0.000002	0.158218
3	6	0	-0.928283	1.211383	0.059485
4	6	0	-2.308911	1.209263	-0.142676
5	6	0	-2.999866	0.000003	-0.244658
6	6	0	-2.308914	-1.209259	-0.142688
7	1	0	-0.388600	-2.146653	0.147490
8	1	0	-0.388596	2.146650	0.147512
9	1	0	-2.844166	2.147431	-0.217210
10	1	0	-4.071197	0.000005	-0.400009
11	1	0	-2.844171	-2.147425	-0.217231
12	6	0	1.243973	-0.000004	0.417839
13	8	0	1.722670	-0.000013	1.554090
14	7	0	1.993794	0.000000	-0.723680
15	1	0	1.508446	0.000021	-1.605236
16	6	0	3.442392	0.000008	-0.697910
17	1	0	3.844403	-0.887571	-1.185693
18	1	0	3.844397	0.887660	-1.185566
19	1	0	3.739005	-0.000064	0.346487

***N*-Methyl acetamide (Figure 2-20)**

MP2/6-31G(d,p)

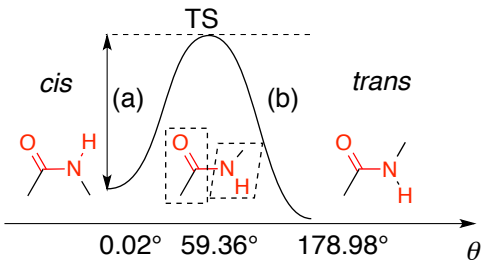

	$\Delta H^{\ddagger}$ [kJ mol^{-1}]	$\Delta G^{\ddagger}$ [kJ mol^{-1}]
(a)	64.62	53.63
(b)	55.01	50.06

Figure 2-20. An energy diagram for carbonyl C-amine N bond rotation in *N*-methyl acetamide. Horizontal axis indicates the dihedral angle of the atoms shown in red color.

cis-ground state

SCF Done: E(RHF) = -247.013169591 A.U. after 7 cycles

Center Number	Atomic Number	Atomic Type	Coordinates (Angstroms) X	Y	Z
1	6	0	0.619085	-0.156837	-0.008523
2	8	0	1.604880	-0.892162	0.054306
3	7	0	-0.64876	-0.671427	-0.116949
4	1	0	-0.674911	-1.674352	-0.009242
5	6	0	0.725429	1.353490	-0.015570
6	1	0	0.331406	1.766959	-0.943601
7	1	0	0.168720	1.794635	0.810791
8	1	0	1.774717	1.612353	0.076880
9	6	0	-1.884318	0.066199	0.056134
10	1	0	-2.708180	-0.558088	-0.280357
11	1	0	-2.071433	0.353924	1.093814
12	1	0	-1.879223	0.964740	-0.556339

trans-ground state

SCF Done: E(RHF) = -247.017176911 A.U. after 9 cycles

Center Number	Atomic Number	Atomic Type	Coordinates (Angstroms) X	Y	Z
1	6	0	-2.423957	-0.271277	-0.373180
2	8	0	-1.966814	0.505872	-1.212665
3	7	0	-2.085996	-1.595081	-0.320102
4	1	0	-2.509481	-2.175706	0.382667
5	6	0	-3.438682	0.170088	0.661604
6	1	0	-4.415684	0.250575	0.187358
7	1	0	-3.513179	-0.513268	1.505644
8	1	0	-3.156705	1.156334	1.019099
9	6	0	-1.173221	-2.192147	-1.272338
10	1	0	-0.335650	-2.668342	-0.764089
11	1	0	-1.676502	-2.930030	-1.897223
12	1	0	-0.802564	-1.387965	-1.900194

Transition state

SCF Done: E(RHF) = -246.990557447 A.U. after 8 cycles

Center Number	Atomic Number	Atomic Type	Coordinates (Angstroms) X	Y	Z
1	6	0	0.437038	0.141778	-0.190002
2	8	0	0.191716	1.168109	0.424956
3	7	0	-0.493989	-0.971779	-0.274499
4	1	0	-0.655010	-1.264312	0.688243
5	6	0	1.712170	-0.097866	-0.947055
6	1	0	2.198136	-0.990793	-0.555605
7	1	0	1.472274	-0.303081	-1.989926
8	1	0	2.371258	0.761422	-0.868394
9	6	0	-1.789230	-0.509483	-0.806253
10	1	0	-2.488441	-1.341854	-0.783673
11	1	0	-2.208424	0.333750	-0.253417
12	1	0	-1.653778	-0.211262	-1.844769

1-aminomethyl-1-methyl-cyclohexa-2,5-diene (**Figure 2-21**)

MP2/6-31G(d,p)

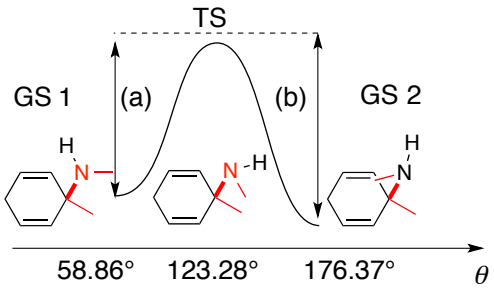

	$\Delta H^{\ddagger}$ [kJ mol^{-1}]	$\Delta G^{\ddagger}$ [kJ mol^{-1}]
(a)	8.87	8.82
(b)	25.85	30.42

Figure 2-21. An energy diagram for C-N bond rotation in 1-aminomethyl-1-methyl-cyclohexa-2,5-diene. Horizontal axis indicates the dihedral angle of the atoms shown in red color.

Ground state1

SCF Done: E(RHF) = -364.937582402 A.U. after 7 cycles

Center Number	Atomic Number	Atomic Type	Coordinates (Angstroms) X	Y	Z
1	7	0	1.801294	-0.430479	-0.095248
2	1	0	2.423355	-0.211771	0.680310
3	6	0	0.635921	0.475807	-0.003549
4	6	0	-0.177128	0.238828	1.242378
5	1	0	0.359002	0.348766	2.182113
6	6	0	1.194404	1.901511	0.009760
7	1	0	1.809619	2.064277	-0.874715
8	1	0	0.382246	2.626661	0.027004
9	1	0	1.814222	2.058194	0.895790
10	6	0	-0.192649	0.274248	-1.240826
11	1	0	0.337196	0.406048	-2.178663
12	6	0	-1.472796	-0.105618	1.256666
13	1	0	-1.975853	-0.264414	2.204563
14	6	0	-1.492859	-0.051943	-1.238683

15	1	0	-2.013932	-0.169076	-2.182704
16	6	0	-2.290055	-0.268428	0.011606
17	1	0	-2.743033	-1.266601	-0.007627
18	1	0	-3.138966	0.425157	0.034653
19	6	0	1.460742	-1.850927	-0.035594
20	1	0	0.884351	-2.144050	0.849354
21	1	0	0.875246	-2.112769	-0.915000
22	1	0	2.384000	-2.427944	-0.058891

Ground state 2

SCF Done: E(RHF) = -364.937578024 A.U. after 7 cycles

Center Number	Atomic Number	Atomic Type	Coordinates (Angstroms) X	Y	Z
1	7	0	1.493372	-0.235154	-0.867838
2	1	0	1.031706	0.116334	-1.702699
3	6	0	0.461624	-0.271469	0.196626
4	6	0	-0.562853	-1.263045	-0.281983
5	1	0	-0.174338	-2.250982	-0.504106
6	6	0	1.099098	-0.794063	1.487507
7	1	0	1.804552	-0.075342	1.904830
8	1	0	0.322471	-0.974192	2.229081
9	1	0	1.627180	-1.72677	1.286590
10	6	0	-0.161274	1.078790	0.441142
11	1	0	0.503598	1.863422	0.787238
12	6	0	-1.860368	-0.986495	-0.472871
13	1	0	-2.522648	-1.766333	-0.832701
14	6	0	-1.457267	1.365409	0.246555
15	1	0	-1.814688	2.372549	0.433231
16	6	0	-2.467771	0.355962	-0.203634
17	1	0	-2.981952	0.718066	-1.101521
18	1	0	-3.256302	0.261481	0.552456
19	6	0	2.671125	0.590093	-0.606262
20	1	0	2.463307	1.626021	-0.313207
21	1	0	3.277949	0.132492	0.172457
22	1	0	3.271665	0.614693	-1.514389

Transition state

SCF Done: E(RHF) = -364.927689014 A.U. after 9 cycles

Center Number	Atomic Number	Atomic Type	Coordinates (Angstroms) X	Y	Z
1	7	0	-1.703683	0.008246	-0.659983
2	1	0	-1.501926	0.236898	-1.628224
3	6	0	-0.538455	0.481256	0.159070
4	6	0	0.483191	1.062841	-0.780384
5	1	0	0.137261	1.897898	-1.384375
6	6	0	-1.066017	1.575955	1.094116
7	1	0	-1.840759	1.163756	1.741248
8	1	0	-0.262712	1.982518	1.710035
9	1	0	-1.510992	2.378522	0.506051
10	6	0	0.071355	-0.614042	0.994123
11	1	0	-0.562363	-1.039919	1.765112
12	6	0	1.739614	0.619474	-0.924825
13	1	0	2.393379	1.095197	-1.647608

14	6	0	1.335519	-1.046285	0.880507
15	1	0	1.692792	-1.820866	1.550482
16	6	0	2.308963	-0.509387	-0.122571
17	1	0	2.639257	-1.313741	-0.790604
18	1	0	3.219187	-0.176755	0.389422
19	6	0	-2.016072	-1.417686	-0.603657
20	1	0	-1.171543	-2.085049	-0.810232
21	1	0	-2.415537	-1.675639	0.375973
22	1	0	-2.798853	-1.613291	-1.335670

2) Rotation inertia

1,3,5-Tris(4-bromophenyl)benzene

B3LYP/3-21G(d)

SCF Done: E(RB3LYP) = -8604.65668444 A.U. after 7 cycles

Center Number	Atomic Number	Atomic Type	Coordinates (Angstroms) X	Y	Z
1	6	0	-0.879726	1.829651	-0.224643
2	6	0	-2.104407	2.047303	0.406497
3	6	0	-2.778588	0.999393	1.033172
4	6	0	-2.218811	-0.277114	1.025910
5	6	0	-0.987307	-0.523102	0.396349
6	6	0	-0.328617	0.549396	-0.227442
7	1	0	-3.722927	1.184484	1.527602
8	1	0	-2.728845	-1.086628	1.534645
9	6	0	-0.394635	-1.887921	0.389287
10	1	0	0.609721	0.373420	-0.739976
11	1	0	-0.371716	2.649739	-0.714555
12	35	0	-2.865549	3.797039	0.413098
13	6	0	-1.199113	-3.011733	0.150627
14	6	0	-0.651366	-4.302705	0.143736
15	6	0	0.722563	-4.460189	0.374689
16	6	0	1.546447	-3.350693	0.611434
17	6	0	0.977008	-2.069141	0.619404
18	1	0	-2.248755	-2.876502	-0.081774
19	6	0	-1.51018	-5.485880	-0.134309
20	1	0	1.154352	-5.453983	0.367990
21	6	0	3.000623	-3.533719	0.869722
22	1	0	1.596809	-1.211951	0.854621
23	6	0	-2.778457	-5.609084	0.456900
24	6	0	-3.587043	-6.714443	0.196379
25	6	0	-3.127997	-7.711821	-0.663763
26	6	0	-1.872064	-7.613472	-1.262367
27	6	0	-1.070940	-6.504355	-0.996329
28	1	0	-4.559701	-6.808033	0.660896
29	35	0	-4.230452	-9.225378	-1.030911
30	1	0	-1.532869	-8.389758	-1.935261
31	1	0	-0.106457	-6.413635	-1.481882
32	1	0	-3.123378	-4.844990	1.143569
33	6	0	3.457779	-4.557016	1.716471
34	1	0	2.740147	-5.202172	2.209500
35	6	0	4.819569	-4.734495	1.955850
36	6	0	5.739932	-3.882541	1.345455

37	1	0	5.165489	-5.518963	2.615817
38	6	0	5.311466	-2.858512	0.500967
39	35	0	7.605370	-4.121433	1.668868
40	6	0	3.947696	-2.689086	0.267357
41	1	0	6.036940	-2.210806	0.026794
42	1	0	3.614488	-1.910169	-0.408295

1,3,5-Tris(4-iodophenyl)benzene

B3LYP/3-21G(d)

SCF Done: E(RB3LYP) = -21590.4312600 A.U. after 6 cycles

Center Number	Atomic Number	Atomic Type	Coordinates (Angstroms) X	Y	Z
1	6	0	-0.881359	1.832537	-0.219997
2	6	0	-2.109489	2.051314	0.408544
3	6	0	-2.782379	0.996510	1.029828
4	6	0	-2.220386	-0.279726	1.020508
5	6	0	-0.987280	-0.522688	0.393937
6	6	0	-0.328761	0.552083	-0.224947
7	1	0	-3.729448	1.168553	1.524053
8	1	0	-2.731529	-1.090778	1.525915
9	6	0	-0.393348	-1.886961	0.385310
10	1	0	0.611116	0.379523	-0.736079
11	1	0	-0.365231	2.648040	-0.709212
12	6	0	-1.197200	-3.010873	0.145199
13	6	0	-0.649068	-4.301604	0.138446
14	6	0	0.724569	-4.458990	0.370636
15	6	0	1.547667	-3.349237	0.608986
16	6	0	0.978118	-2.067769	0.616777
17	1	0	-2.246793	-2.876012	-0.087566
18	6	0	-1.508466	-5.484889	-0.137363
19	1	0	1.156604	-5.452675	0.364324
20	6	0	3.001413	-3.532544	0.869460
21	1	0	1.597498	-1.210586	0.853118
22	6	0	-2.774717	-5.606791	0.457199
23	6	0	-3.584925	-6.712759	0.201013
24	6	0	-3.131235	-7.715348	-0.659204
25	6	0	-1.874573	-7.614894	-1.260720
26	6	0	-1.072203	-6.504654	-0.998540
27	1	0	-4.554729	-6.796063	0.673504
28	1	0	-1.528293	-8.387531	-1.934415
29	1	0	-0.108944	-6.415836	-1.487170
30	1	0	-3.118086	-4.841876	1.143907
31	6	0	3.456824	-4.555842	1.716304
32	1	0	2.738638	-5.200643	2.209253
33	6	0	4.818881	-4.735572	1.956609
34	6	0	5.745129	-3.885691	1.347476
35	1	0	5.153257	-5.523821	2.618113
36	6	0	5.313887	-2.859933	0.503117
37	6	0	3.949651	-2.688906	0.268791
38	1	0	6.032498	-2.207281	0.025169
39	1	0	3.618621	-1.908967	-0.406952
40	53	0	-2.967487	4.013888	0.420375
41	53	0	7.839434	-4.160400	1.708166
42	53	0	-4.371906	-9.415683	-1.062246

References

[1] Chen, X.; Wen, J. *Nanoscale Res. Lett.* **2012**, *7*, 598.

[2] Schäffel, F.; Wilson, M.; Warner, J. H. *ACS Nano* **2011**, *5*, 9428–9441.

[3] (a) Gao, K. W.; Li, S.; Qiao, J.; Chu, W. Y. *Mater. Sci. Technol.* **2002**, *18*, 1109–1114. (b) Robach, J. S.; Robertson, I. M.; Wirth, B. D.; Arsenlis, A. *Philos. Mag.* **2003**, *83*, 955–967. (c) Abe, H.; Sekimura, N.; Tadokoro, T. *Mater. Trans.* **2005**, *46*, 433–439. (d) Vives, G.; Tour, J. M. *Acc. Chem. Res.* **2009**, *42*, 473–487. (e) Schneider, S.; Surrey, A.; Pohl, D.; Schultz, L.; Rellinghaus, B. *Micron* **2014**, *63*, 52–56. (f) Zhou, W.; Li, X.; Zhu, G.-Z. *Microsc. Microanal.* **2015**, *21*, 617–625.

[4] (a) Khlobystov, A. N.; Porfyrakis, K.; Kanai, M.; Britz, D. A.; Ardavan, A.; Shinohara, H.; Dennis, T. J. S.; Briggs, G. A. D. *Angew. Chem. Int .Ed.* **2004**, *43*, 1386–1389. (b) Chuvilin, A.; Bichoutskaia, E.; Gimenez-Lopez, M. C.; Chamberlain, T. W.; Rance, G. A.; Kuganathan, N.; Biskupek, J.; Kaiser, U.; Khlobystov, A. N. *Nat. Mater.* **2011**, *10*, 687–692.

[5] (a) Ring, E. A.; de Jonge, N. *Micron* **2012**, *43*, 1078–1084. (b) Protetto, M. T.; Rush. A. M.; Chien, M.-P.; Baeza, P. A.; Patterson, J. P.; Thompson, M. P.; Olson, N. H.; Moore, C. E.; Rheingold, A. L.; Andolina, C.; Millstone, J.; Howell, S. B.; Browning, N. D.; Evans, J. E.; Gianneschi, N. C. *J. Am. Chem. Soc.* **2014**, *136*, 1162–1165.

[6] (a) Koshino, M.; Tanaka, T.; Solin, N.; Suenaga, K.; Isobe, H.; Nakamura, E. *Science* **2007**, *316*, 853. (b) Koshino, M.; Solin, N.; Tanaka, T.; Isobe, H.; Nakamura, E. *Nat. Nanotechnol.* **2008**, *3*, 595–597.

[7] Harano, K.; Takenaga, S.; Okada, S.; Niimi, Y.; Yoshikai, N.; Isobe, H.; Suenaga, K.; Kataura, H.; Koshino, M.; Nakamura, E. *J. Am. Chem. Soc.* **2014**, *136*, 466–473.

[8] Solin, N.; Koshino, M.; Tanaka, T.; Takenaga, S.; Kataura, H.; Isobe, H.; Nakamura, E. *Chem. Lett.* **2007**, *36*, 1208–1209.

[9] Harano, K.; Homma, T.; Niimi, Y.; Koshino, M.; Suenaga, K.; Leibler, L.; Nakamura, E. *Nat. Mater.* **2012**, *11*, 877–881.

[10] (a) Nakamura, E.; Koshino, M.; Tanaka, T.; Niimi, Y.; Harano, K.; Nakamura, Y.; Isobe, H. *J. Am. Chem. Soc.* **2008**, *130*, 7808–7809. (b) Gorgoll, R. M.; Yücelen, E.; Kumamoto, A.; Shibata, N.; Harano, K.; Nakamura, E. *J. Am. Chem. Soc.* **2015**, *137*, 3474–3477.

[11] (a) Bambynek, W.; Crasemann, B.; Fink, R. W.; Freund, H.-U.; Mark, H.; Swift, C. D.; Price, R. E.; Rao, P. V. *Rev. Mod. Phys.* **1972**, *44*, 716–813. (b) Drescher, M.; Hentschel, M.; Kienberger, R.; Uiberacker, M.; Yakovlev, V.; Scrinzi, A.; Westerwalbesloh, T.; Kleineberg, U.; Heinzmann,

U.; Krausz, F. *Nature* **2002**, *419*, 803–807.

[12] (a) Guldi, D. M.; Marcaccio, M.; Paolucci, D.; Paolucci, F.; Tagmatarchis, N.; Tasis, D.; Vázquez, E.; Prato, M. *Angew. Chem. Int. Ed.* **2003**, *2003*, 4206–4209. (b) Guldi, D. M.; Rahman, G. M. A.; Jux, N.; Tagmatarchis, N.; Prato, M. *Angew. Chem. Int. Ed.* **2004**, *43*, 5526–5530. (c) Guldi, D. M.; Taieb, H.; Rahman, G.; Tagmatarchis, N.; Prato, M. *Adv. Mater.* **2005**, *2005*, 871–875. (d) Herranz, M. A.; Ehli, C.; Campidelli, S.; Gutiérrez, M.; Hug, G. L.; Ohkubo, K.; Fukuzumi, S.; Prato, M.; Martín, N.; Guldi, D. M. *J. Am. Chem. Soc.* **2008**, *130*, 66–73.

[13] Still, W. C.; Kahn, M.; Mitra, A. *J. Org. Chem.* **1978**, *43*, 2923-2925.

[14] Gaussian 09, Revision **D.01**, Frisch, M. J.; Trucks, G. W.; Schlegel, H. B.; Scuseria, G. E.; Robb, M. A.; Cheeseman, J. R.; Scalmani, G.; Barone, V.; Mennucci, B.; Petersson, G. A.; Nakatsuji, H.; Caricato, M.; Li, X.; Hratchian, H. P.; Izmaylov, A. F.; Bloino, J.; Zheng, G.; Sonnenberg, J. L.; Hada, M.; Ehara, M.; Toyota, K.; Fukuda, R.; Hasegawa, J.; Ishida, M.; Nakajima, T.; Honda, Y.; Kitao, O.; Nakai, H.; Vreven, T.; Montgomery, J. A.; Jr., Peralta, J. E.; Ogliaro, F.; Bearpark, M.; Heyd, J. J.; Brothers, E.; Kudin, K. N.; Staroverov, V. N.; Kobayashi, R.; Normand, J.; Raghavachari, K.; Rendell, A.; Burant, J. C.; Iyengar, S. S.; Tomasi, J.; Cossi, M.; Rega, N.; Millam, J. M.; Klene, M.; Knox, J. E.; Cross, J. B.; Bakken, V.; Adamo, C.; Jaramillo, J.; Gomperts, R.; Stratmann, R. E.; Yazyev, O.; Austin, A. J.; Cammi, R.; Pomelli, C.; Ochterski, J. W.; Martin, R. L.; Morokuma, K.; Zakrzewski, V. G.; Voth, G. A.; Salvador, P.; Dannenberg, J. J.; Dapprich, S.; Daniels, A. D.; Farkas, Ö.; Foresman, J. B.; Ortiz, J. V.; Cioslowski, J.; Fox, D. J. Gaussian, Inc., Wallingford CT, 2009.

[15] Elmorsy, S. S.; Pelter, A.; Smith, K. *Tetrahedron Lett.* ***1991,*** *32*, 4175–4176.

[16] Zhao, S.; Kang, L.; Ge, H.; Yang, F.; Wang, C. *Synth. Commun.* **2012**, *42*, 3569–3579.

[17] Isobe, H.; Tanaka, T.; Maeda, R.; Noiri, E.; Solin, N.; Yudasaka, M.; Iijima, S.; Nakamura, E. *Angew. Chem. Int. Ed.* **2006**, *45*, 6676–6680.

[18] Rehak, V.; Kaderabek, V. *Coll. Czech. Chem. Commun.* **1979**, *44*, 1613–1618.

[19] Urban, K. W.; Jia, C.-L.; Houben, L.; Lentzen, M.; Mi, S.-B.; Tillmann, K. *Philos. Trans. A* **2009**, *367*, 3735–3753.

[20] Marcus, R. A. *J. Chem. Phys.* **1952**, *20*, 359–364.

Chapter 3. Intermolecular Reaction Kinetics Based on Single-Molecule Transmission Electron Microscopic Imaging

3-1 Introduction

When a molecule is electronically excited, the molecule undergoes chemical reaction at the potential energy surface (PES) different from that of ground state, showing unique reactivity and selectivity.[1] Thermal activation cannot excite molecules in conventional conditions, but photons and electrons can electronically excite molecules. Once molecule is excited, the excess vibrational energy is relaxed in the time order of 10^{-14} to 10^{-13} seconds, and the vibrational ground state in the PES is the only concern for the reaction mechanism.[2] This in turn shows that we have rarely considered reactions that undergo before energy relaxation, though this pathway is one of the possibilities based on the PES.

Here I show the first observation and analysis of unimolecular reactions of [60] fullerene molecules at electronic excited states with excess energy. We have previously observed van der Waals (vdW) dimer complexes of C_{60} under one-dimensional confinement in single-walled carbon nanotube (CNT) undergoing dimerization (step 1) followed by bond rearrangement (step 2) to form tubular C_{120} through single-molecule atomic real-time transmission electron microscopy (SMART-TEM, Figure 3-1).[3] I noted that SMART-TEM is an appropriate methodology to investigate excited-state chemistry since electron-specimen interactions excite molecules as in photochemistry. The reaction frequencies were analyzed at the stage temperature T_s of 4 to 793 K to figure out the four features; (1) the reaction frequencies follow the first-order kinetics at each temperature, (2) the temperature dependency of the reaction rate follows the statistical reaction theory, (3) the activation energy of the reaction, the most fundamental parameters in reaction kinetics, can be elucidated, and (4) the reaction rate depends on the beam energy. The reaction contained two reaction paths; temperature-dependent path with the activation energy of 13.3–42.6 kJ/mol that is dominant at high temperature, and temperature-insensitive path dominant at low temperature. The latter path undergoes from extremely high-energy state generated by electron impact.

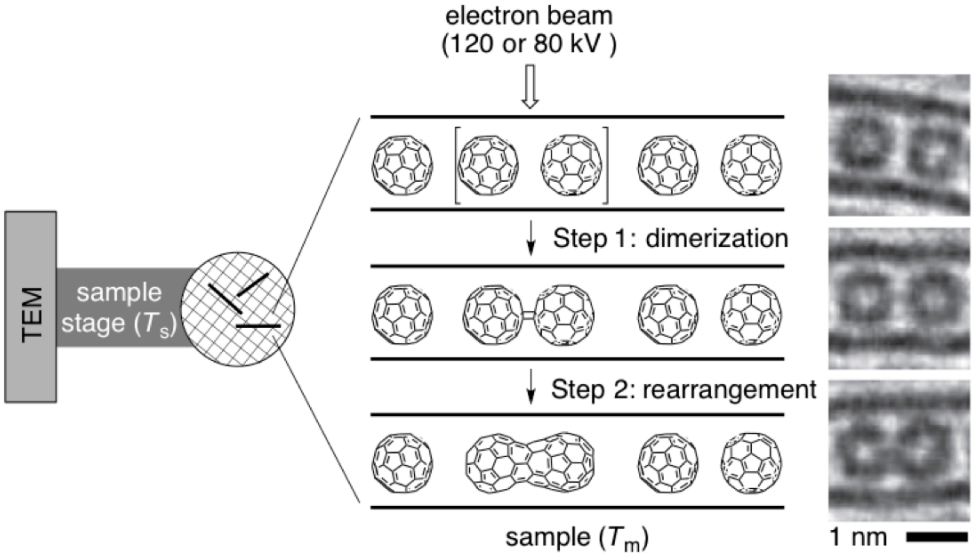

Figure 3-1. SMART-TEM imaging of fullerene dimerization followed by rearrangement inside CNT. Images were taken at 120 kV, 293 K. TEM images were reproduced from ref. 3 with permission from Nature Publishing Group.

3-2 Dimerization of C_{60}

Fullerene undergo [2 + 2] cycloaddition by photoirradiation, compression, and chemical reactions to afford C_{120} with D_{2h} symmetry, where C-C bonds between two hexagons are connected. The first observed reaction was the polymerization of face-centered cubic fullerene crystal was irradiated with 300-W mercury lamp in the absence of O_2 and H_2O.[4] The photoirradiation condition was calculated to have the energy barrier of 25 kJ/mol at the singlet state.[5] This low energy barrier would be attributed to the symmetrical allowance of [2 + 2] dimerization in frontier orbital theory accompanied with the high ring strain of curved π system in fullerene. On the other hand, the symmetrically forbidden reaction in the ground state can also take place at high pressure (> 1 GPa)[6] with the activation energy of 134 ± 6 kJ/mol.[7] The dimerization is an exothermic reaction with the stabilization energy of 60.8 kJ/mol (BP86-D/SVP level of theory),[8] and the dimer is further stabilized by successive rearrangement toward carbon nanotube.[9] The dimerization proceeds at radical state as well as chemically neutral state, and a cation radical of fullerene generated by single electron transfer from fullerene to iron(III) chloride can facilitate [2 + 2] dimerization.[10]

In addition to the fullerene dimerization induced by photon, pressure, and radical species, electron beam also induces dimerization inside carbon nanotube to afford C_{120} with C_s symmetry where pentagon and hexagon edges are connected to each other (Figure 3-2).[3] CNT with diameters

ranging from 1.2 to 1.5-nm was oxidized to remove the end cap. This treatment partially destroyed the conjugation of CNT and increased the ionization potential (IP) to somewhat higher than that of pristine CNT of 4.8 eV.[11] To this open-ended CNT, fullerene was sublimed at 773 K to be encapsulated into CNT. Thus obtained C_{60} peapod is placed onto a carbon-supported copper microgrid and observed in TEM by irradiating 120- or 80-keV electrons at the dose rate in the order of 10^5 electrons s^{-1} $molecule^{-1}$ (Figure 3-1). Note that the dose rate varies by the temperature because of the difference in machine setup. The SMART-TEM images show that the reaction is composed from two steps; dimerization of vdW dimer of C_{60} in [2 + 2] manner (step 1) followed by C-C bond rearrangement toward short CNTs (step 2, Figure 3-1), and also give the appearance of reaction events, or the total electron dose (TED) at which the fullerene molecules reacted. The reaction rates and activation energies for step 1 and step 2 are obtained here from the observed reaction frequencies.

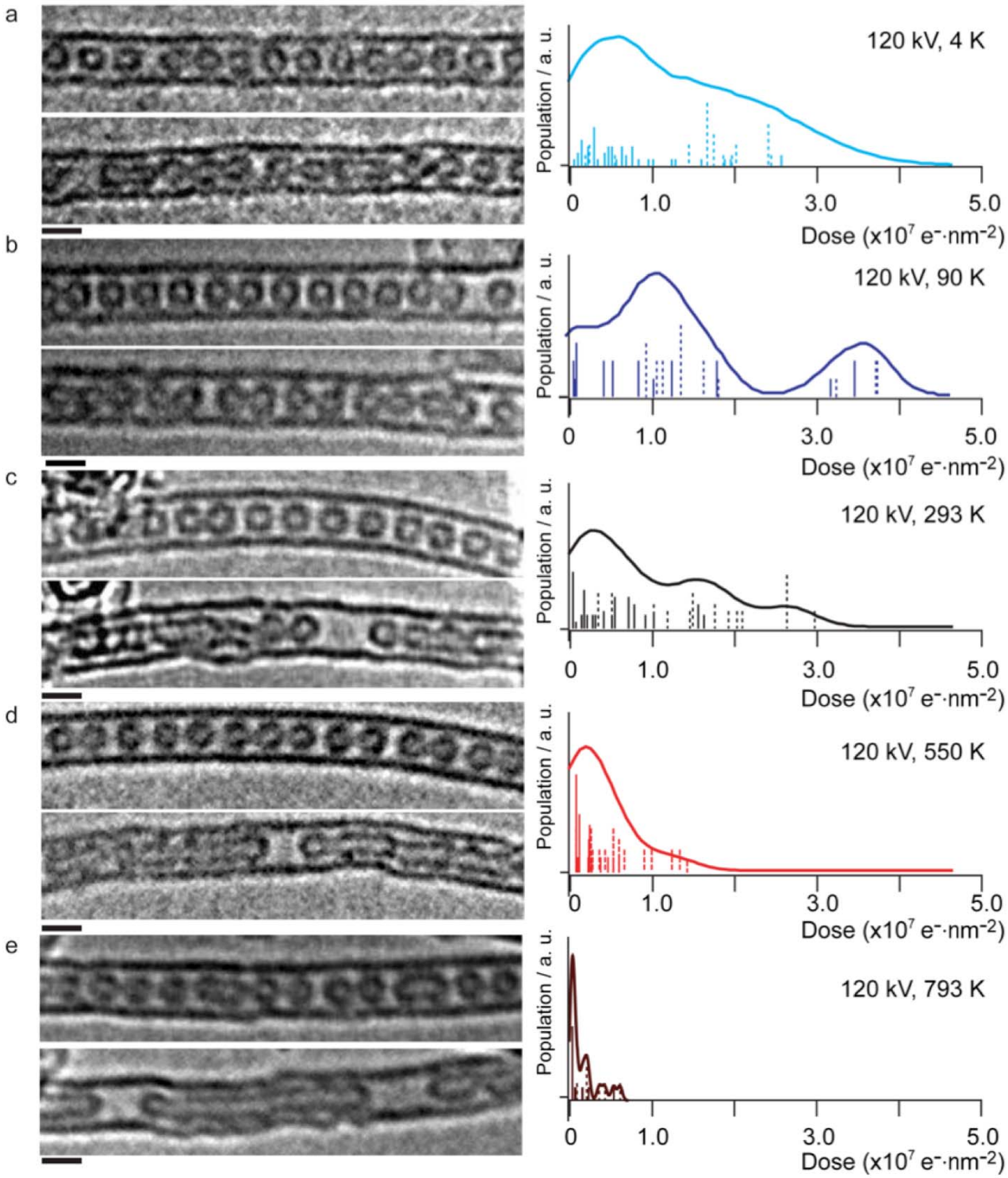

Figure 3-2. Temperature dependence of step 1 and step 2 reactions observed in VT-SMART-TEM. Temperatures are (a) 4, (b) 90, (c) 293, (d) 550 and (e) 793 K. (Left) Upper and lower images are taken at the TED of 1.3×10^6 e nm^{-2} and 2.5×10^7 e nm^{-2} (1.3×10^7 e nm^{-2} for (e)), respectively. Scale bars are 1 nm. (Right) Distributions of step 1 and 2 are depicted as solid and broken lines, and broadened with a Gaussian curve that has a full width at half maximum of the corresponding standard deviations. Reprinted from ref. [3] with permission from Nature Publishing Group.

3-3 Reaction Mechanism

The reaction mechanism of step 1 is summarized in Figure 3-3 based on the fact that unreacted C_{60} were observed at the initial frame of the image sequences. This indicates that electron-specimen interaction initiated the reaction. The most plausible mechanism involves in ionization of C_{60} followed by chemical reactions at PES above ground state. First, electron beam ionizes C_{60} to give radical cation of van der Waals dimer of C_{60}. When 120- or 80-keV electrons interact with C_{60}, C_{60} acquire energy up to 26.4 or 17.1 eV, respectively.[12] These maximum energies are large enough to eject valence and inner-shell electrons in C_{60} (cf. calculated 2s orbital of carbon in C_{60}: 26.3 eV, HOMO 5.99 eV, experimental IP 7.6 eV[13]). The radical cation possesses excess vibrational energy, which is enough to drive C-C bond formation to obtain [2 + 2] dimer with the rate constant of k_{rad} (path 1). Van der Waals dimer that did not undergo chemical reaction releases excess vibrational energy in the time order of $k_{rx} = 10^{14}$–10^{11} s^{-1}.[2] The radical cation is surrounded by oxidized CNT with the IP larger but close to 4.8 eV, and single electron transfer (SET) from CNT to the radical cation with the rate constant of $k_{et} \sim 10^{8}$–10^{10} s^{-1} considering the through-space charge recombination in a system where an anion fullerene derivative is non-covalently attached on CNT radical cation (9.7×10^{8} s^{-1}).[14] This electron transfer finally gives neutral and triplet electronic excited state of C_{60} van der Waals dimer since the singlet excited state of C_{60} undergo intersystem crossing (ISC) to triplet state within 10^{-9} s. Some of the triplet states are thermally activated to undergo symmetrically allowed [2 + 2] cycloaddition over the energy barrier of E_d with the rate constant of k_{neu} (path 1) within the lifetime of triplet states of ~1 μs.[15] Those did not react are further quenched to ground state by ISC. Throughout the reaction, the nature of CNT including the helicity and diameter does not significantly contribute to the reaction kinetics, since vibrational relaxation and electron transfer are the only steps where CNT contributes to the reaction. The similar diagram would be applicable to step 2. These mechanisms also indicate that the each reaction event occurs independently considering the 10-μs time order of electron irradiation to vdW dimer.

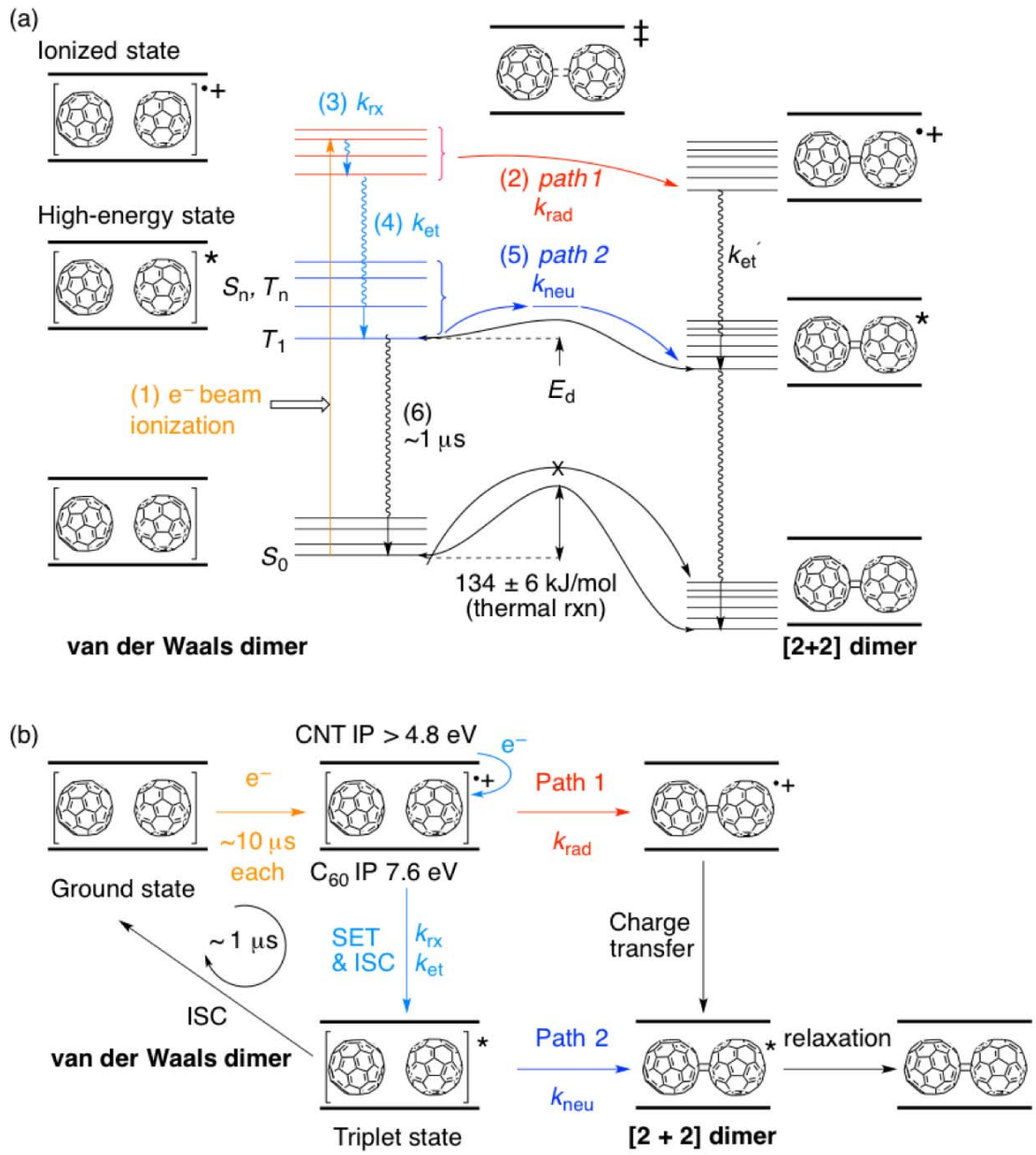

Figure 3-3. Reaction mechanism of step 1 (C_{60} dimerization) reaction. (a) Energy diagram. (1) Electron-C_{60} interaction, (2) thermal relaxation of vibrational states, (3) electron transfer, (4) intersystem crossing, (5) thermally activated chemical reactions at the triplet state, and (6) reaction at radical cation state. (b) A scheme of energy and charge states involving in step 1 reaction.

The PES of the step 1 reaction further suggests that vibrationally activated state is involved in path 1 (Figure 3-4). The PES at radical cation state either possesses activation energy or monotonic decrease in energy along the reaction coordinate. However, temperature dependence of the reaction would be less obvious in the latter case since radical cation formation by electron-specimen interaction is temperature-independent. Therefore, the PES possesses activation energy. This illustration also infers the temperature dependence of k_{rad} and relaxation path (2). This

conclusion indicate that the reaction rate strongly depends on the beam energy and less dependent on temperature since the path 1 proceeds from vibrational excited state, and the excess vibrational energy is given by electron-specimen interaction.

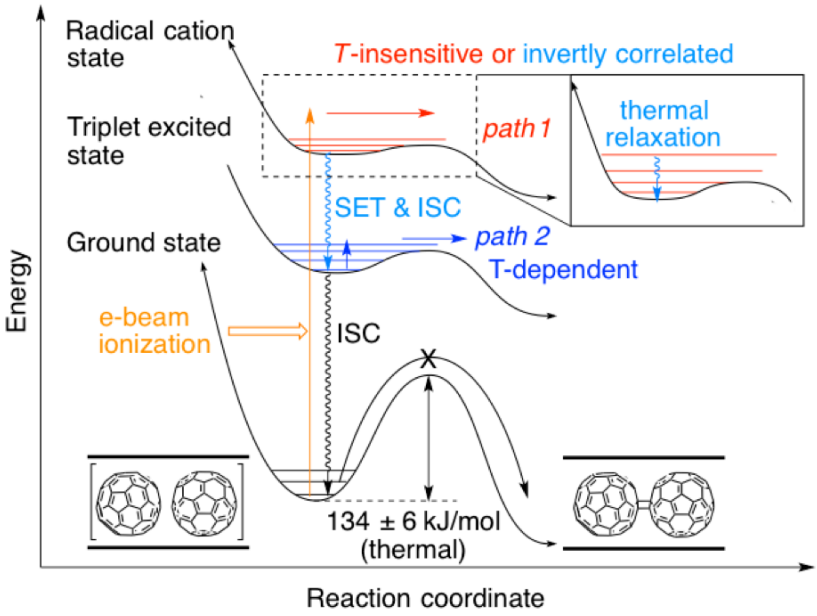

Figure 3-4. PES of step 1 reaction.

One may think that the temperature of the molecules T_m may be different from that of stage temperature T_s, which affect the discussion on the temperature dependence of reaction rate. It is possible that there is a deviation between T_m and T_s because of temperature gradient from the microgrid and the TEM holder and heating by electron beam. However, even though we assume T_m is 50 or 200 K higher than T_s, the final conclusion of the existence of two reaction paths did not change, though activation energy changes. Here we assume T_m is the same as T_s for simplicity.

3-4 Dimerization Kinetics at Each Temperature

Figure 3-5 shows the appearance of C_{60} dimerization reaction events observed in VT-SMART-TEM under constant electron dose at 4, 90, 293, 550, and 793 K at the beam voltage of 120 kV and at 293 K at the beam voltage of 80 kV. This plot shows the number of reaction events plotted against TED with the unit of e nm^{-2} that is equivalent to the reaction time under constant electron dose rate. For instance, 53 reaction events were observed within 2.0 x 10^7 e nm^{-2} at 4 K, or one reaction event by 10^5 electrons irradiated to a vdW dimer. This frequency is reasonable considering the ionization cross section of carbon in the order of 10^{-2} nm^2, indicating ca. 0.1% probability of reaction against the ionization event.[16] The reaction speed is the fastest at 793 K and it slows down by decreasing the stage temperature. The reaction rate is sensitive to the

electron beam energy, and the reaction significantly slowed down under 80-kV electron beam. Notably, the reaction even proceeded at 4 K, where thermally activated reaction rarely proceeds. This fact is one of the proofs that excess energy for reaction in addition to energy for ionization is given by electron-specimen interactions.

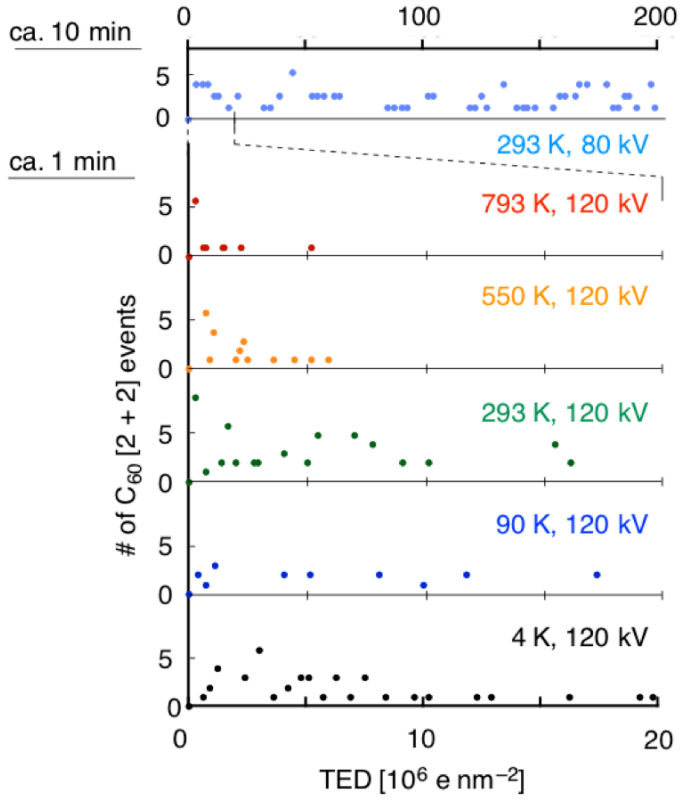

Figure 3-5. Appearance of fullerene dimerization events against TED. Colors indicate reactions at 4 (black), 90 (blue), 293 (green), 550 (orange), and 793 K (red) at 120 kV, and at 293 K, 80 kV (cyan).

The single-molecule reaction events were cumulated for statistical kinetic analysis (Figure 3-6a). The total number of events increases and the increasing speed decreases over electron dose. The y-axis is converted to the extent of reaction P_1 by normalization by the total number of reaction events at each temperature (Figure 3-6b);

$$P_1 = \frac{N(e_t)}{N(\infty)} \qquad \text{(eq.3-1)}$$

where $N(e)$ is the cumulative number of reactions at the TED of e_t that has the unit of [e nm^{-2}], and $N(\infty)$ is the total number of observed reaction events.

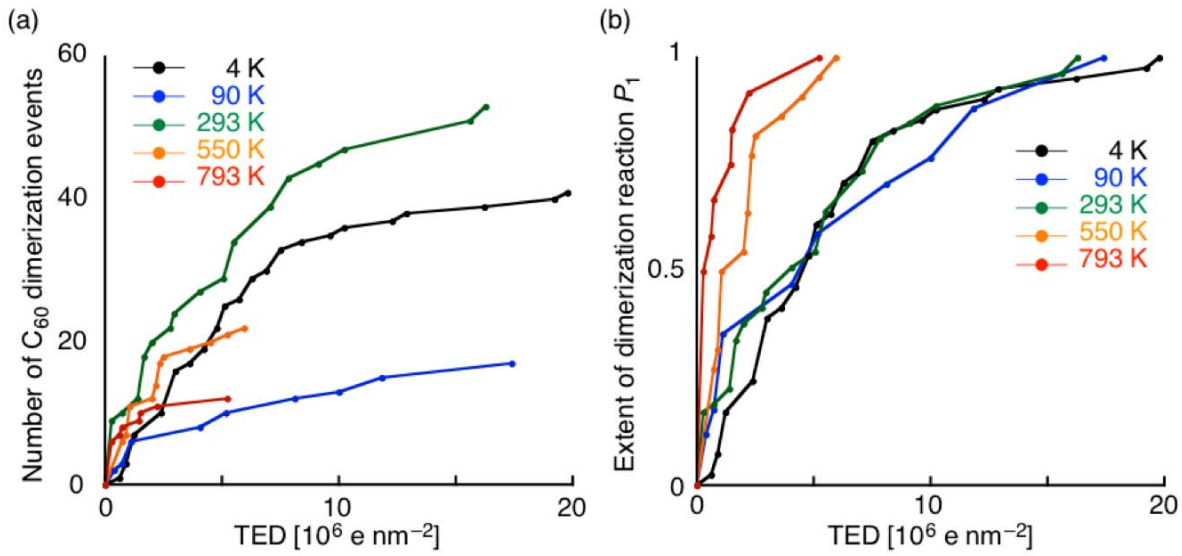

Figure 3-6. Cumulated fullerene dimerization events. (a) Total number of dimerization events and (b) extent of reaction are plotted against TED. Colors indicate reactions at 4 (black), 90 (blue), 293 (green), 550 (orange), and 793 K (red) at 120 kV.

The cumulative reaction events were semi-logarithmically plotted against the total dose to determine the reaction rate against e_t in the unit of e^{-1} nm^2 following the equation (Figure 3-7);

$$y = \ln\left(1 - P_1\right) \qquad \text{(eq.3-2)}$$

This semi-logarithmically plotted reaction events show linear relation against TED. These data points were fitted in a linear equation

$$y = -k_d\left(e_t\right) \qquad \text{(eq.3-3)}$$

where k_d is the reaction rate of step 1 that has the unit of [e^{-1} nm^2]. The existence of linear relation with the Pearson product-moment correlation coefficient of 0.957–0.994 proves that summation of sporadic single molecular events explains thermodynamic behavior. In addition, the linear relation shows the first-order reaction kinetics of C_{60} dimerization, indicating that the dimerization started from a van der Waals complex, or molecular diffusion before intermolecular collision can be neglected.

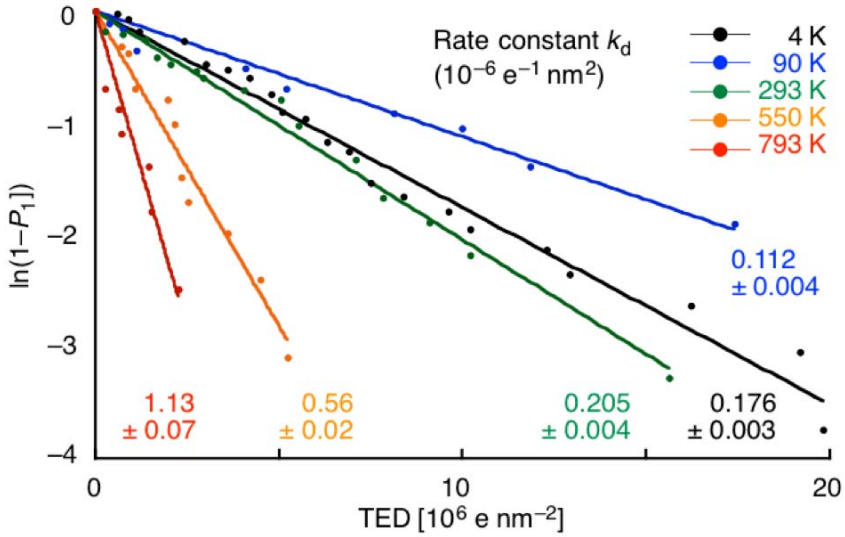

Figure 3-7. A semi-logarithmic plot of fullerene dimerization events at various temperatures and fitting parameters following eq. 3-3. Colors indicate reactions at 4 (black), 90 (blue), 293 (green), 550 (orange), and 793 K (red) at 120 kV.

The reaction rate at 80 kV, 293 K was 1.5% of that at 120 kV, showing the significant contribution of the electron beam energy onto the reaction kinetics (Figure 3-8). This result imply the existence of activation energy at the PES of radical cation state since 80-keV electrons gives rise to radical cation state with lower vibrational states than that excited by 120-keV electrons.

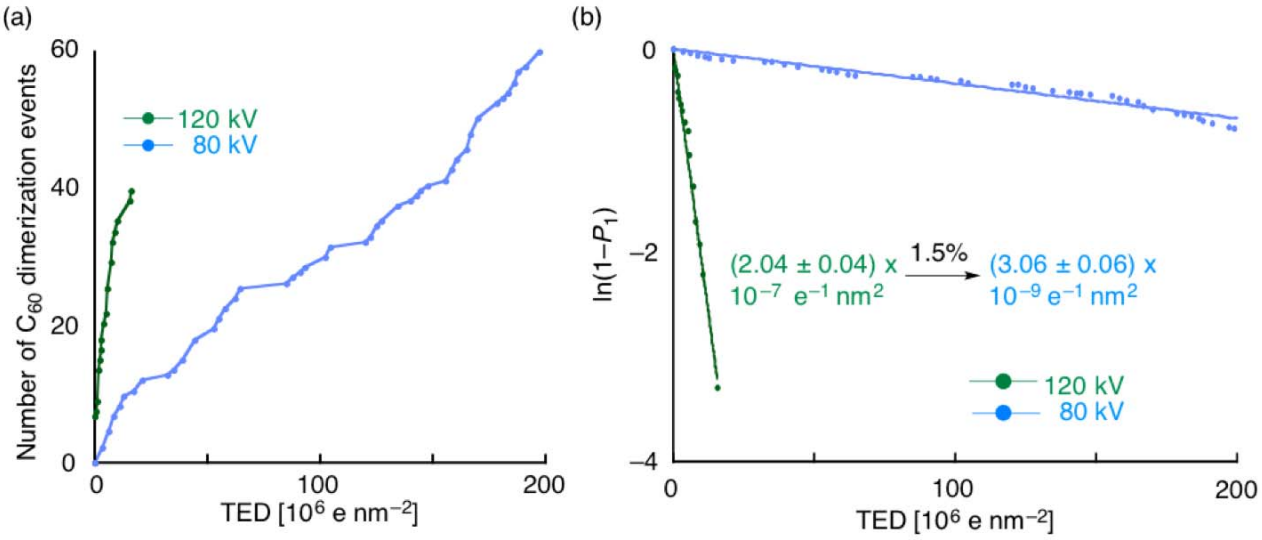

Figure 3-8. Analysis of step 1 reaction at 293 K at 120 kV (green) and 80 kV (cyan). (a) Total number of dimerization events. (b) A semi-logarithmic plot of fullerene dimerization events at various temperatures and fitting parameters following eq. 3-3.

Regarding the reactivity of molecules, it is noteworthy that the reactivity of molecules

under TEM depends on the IP of the molecules. Alkyl-tethered carboranes inside CNT[17] and amides,[18] alkanes, and perfluoroalkanes[19] attached outside CNT with IP higher than 10 did not show any reaction within 10^6 e nm^{-2}, while fullerenes,[20] CNT and their analogues,[21] sulfur-terminated graphene nanoribbons,[22] buckymetallocenes[23] and some metallated fullerenes[24] with IP less than 8 reacted or decomposed. This difference in reactivity can be explained by admitting the formation of excited states and radical cation states by electron-specimen interactions.

3-5 Temperature Dependence of Reaction Kinetics

The obtained k_d was plotted against stage temperature. The reaction rate was almost constant up to 293 K, and increases rapidly at higher temperature. This temperature dependence was fitted based on Rice-Ramsperger-Kassel-Marcus (RRKM) theory and the energy diagram in Figure 3-4.[25] RRKM theory describes the unimolecular reaction kinetics from the viewpoint of quantum states of reactants and transition states, and has been applied for bulk reaction systems such as decomposition[26] and bond formation reactions.[27] In the current dimerization system of the excited-state dynamics of path 2, excitation and relaxation mechanisms are constant, and the reaction rate is governed by the transformation of excited state to transition state. Therefore, the reaction rate is governed by

$$k_{neu} = \frac{N^{\ddagger}}{h\rho(E)} \qquad \text{(eq.3-4)}$$

where $N^{\ddagger}$ is the number of states at transition states and responds exponentially against the reverse temperature, h is the Planck's constant, and ρ(E) is the density of states at the initial state that slightly depends on temperature. This expression can be simplified as

$$k_{neu} \cong a_d \exp\left(-\frac{E_d}{RT_m}\right) \qquad \text{(eq.3-5)}$$

where a_d is the pre-exponential factor and R is the gas constant. In the first approximation, path 1 depends only on the beam energy and E_d, and can be considered as a constant c_d, i.e.

$$k_{rad} \cong c_d \qquad \text{(eq.3-6)}$$

Based on the discussion, the rate constant was fitted by

$$k_d = k_{neu} + k_{rad} = a_d \exp\left(-\frac{E_d}{RT_m}\right) + c_d \qquad \text{(eq.3-7)}$$

This fitting curve well explained the temperature dependence of k_d, and E_d was calculated to be 13.3 kJ/mol assuming $T_m = T_s$ (Figure 3-9a). The obtained E_d was smaller than that of

pressure-induced fullerene dimerization (134 ± 6 kJ/mol)[7] or semi-empirical calculation at ground state (143 kJ/mol)[28] and close to the calculated value at excited state (25 kJ/mol),[29] implying that the dimerization is taking place at electronic excited state.

Both the temperature-sensitive k_{neu} and temperature-insensitive k_{rad} are required to explain the temperature dependence of k_d, since the fitting curve did not match without c_d term (Figure 3-9b). One may think that T_m deviates from T_s because indirect heating of molecules that can cool down T_m than T_s, i.e. heat from TEM holder is transferred to the specimen molecules through CNT loosely attached on TEM grid, and direct heating by electron-specimen interaction. However, the T_m shift of +50 or +200 K from T_s only resulted in slight change in E_d (15.7 and 24.1 kJ/mol, respectively) and two paths were required for good fit (Figure 3-9c, d). These results indicate the coexistence of the temperature-insensitive path through the radical cation state and the temperature-dependent path that shows exponential response to the inverse temperature.

The smaller k_d than fitted line at 90 K can be explained by the kinetics of the thermal relaxation path (Figure 3-4). Intramolecular vibration contributes to energy re-distribution within a molecule to relax local vibrational energy, and the vibration is more restricted at low temperature. Therefore, vibrational relaxation takes place quicker at 90 K than at 4 K. However, the 90-K temperature would not be enough to thermally activate the radical cation of van der Waals dimer of C_{60}, resulting in decrease in apparent k_{rad}.

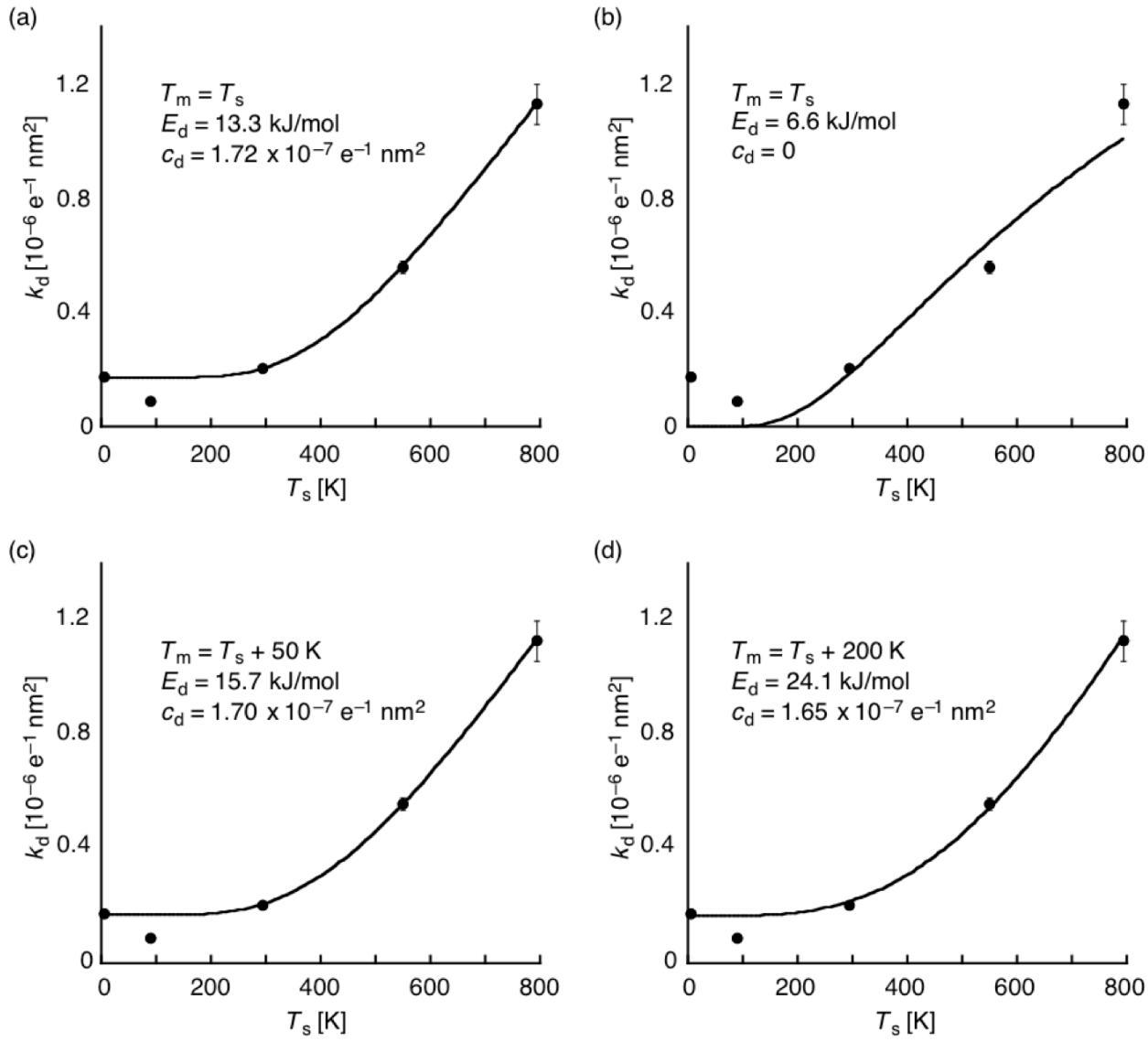

Figure 3-9. Plot and fitting of temperature-dependent reaction rate of step 1. Fitting curves were based on eq. 12 (a) without any modification, (b) fixed c_d value to be zero, (c) assuming $T_m = T_s$ + 50 K, and (d) assuming $T_m = T_s$ + 200 K.

The contribution of path 1 is calculated from the obtained fitting parameter (Figure 3-10). Path 2 does not contribute at 4 K and 90 K, and it only contributes more than 1% at T > 193 K. This also indicates that the reaction rate at 4 and 90 K is insensitive to the deviation of stage temperature. At 293 K, both path 1 and path 2 coexist, and the contribution of path 2 is 15%. Path 1 becomes more dominant at higher temperature. Note that the contribution shown here does not necessarily represent the exact values because of the discussion above and the possibility to overcome the energy barrier on the PES of radical cation state at high temperature regions.

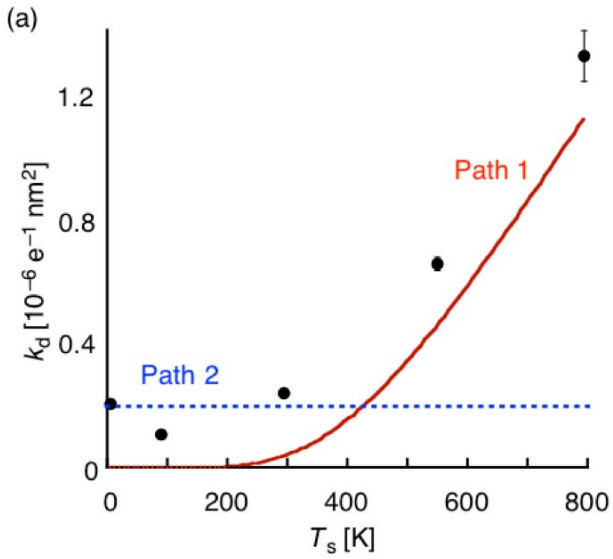

(b)

T [K]	Contribution from path 1 [%]
4	~0
90	1.4×10^{-5}
293	15
550	70
793	85

Figure 3-10. Contribution of T-dependent reaction pathway. (a) Plot of reaction rate and contributions from T-dependent process (red) and T-insensitive process (blue) for C_{60} dimerization. (b) Ratio of T-dependent process.

3-6 Kinetics of C_{60}-C_{60} dimer rearrangement

Step 2 reaction was similarly analyzed. The reaction event plot shows that the reaction appearance is few at small TED and being almost constant along TED (Figure 3-11). The rearrangement events are composed of several possible mechanisms of bond cleavage and bond formation, and the averaged reaction kinetics of these mechanisms are observed in TEM because the spatial resolution is not enough to clarify each mechanism and it is difficult to distinguish the rearrangement that do not change inter-fullerene distance. Rearrangement reaction was not observed till the TED of 7×10^6 e nm^{-2} at 90 K, 120 kV, and till 45×10^6 e nm^{-2} at 293 K, 80 kV. This is obviously because step 2 reaction takes place after step 1, and because step 1 reaction at 90 K is slower than those at other temperatures due to fast vibrational relaxation and insufficient energy to overcome energy barrier at triplet PES. This graph also shows that step 2 is slower than step 1 since otherwise the appearance of reaction events show similar trends with that of step 1. The slow kinetics of step 2 indicates the higher activation energy at triplet PES than that of step 1.

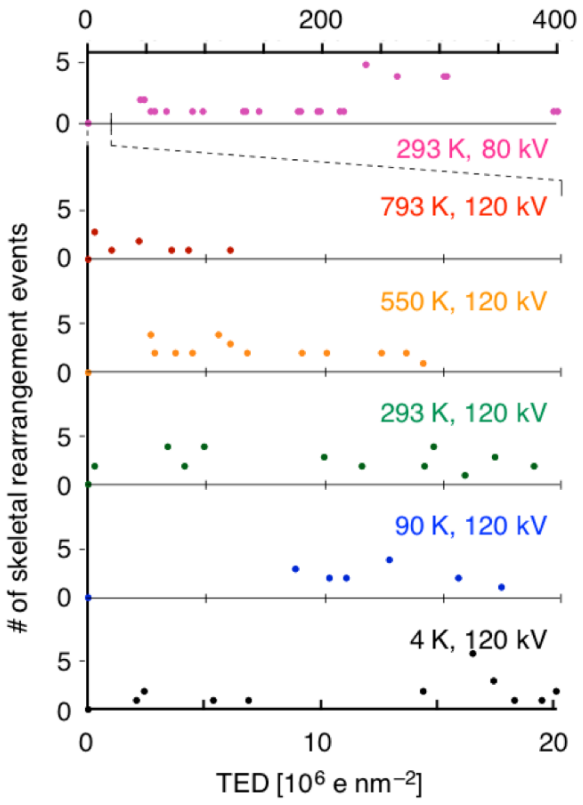

Figure 3-11. Appearance of C_{60} rearrangement events against TED. Colors indicate reactions at 4 (black), 90 (blue), 293 (green), 550 (orange), and 793 K (red) at 120 kV, and 293 K, 80 kV (pink).

The reaction rate of step 2 (k_r) was obtained based on the fact that the step 2 reaction is unimolecular and the kinetics is explained in first-order equation. The reaction events were cumulated (Figure 3-12a) and normalized to obtain the reaction progress P_2. For the two sequential first-order reactions;

$$\underset{\text{vdW complex}}{C_{60} + C_{60}} \xrightarrow{k_d} \underset{\text{[2+2] dimer}}{C_{60}-C_{60}} \xrightarrow{k_r} \underset{\text{fused dimer}}{C_{120}} \qquad \text{(eq.3-8)}$$

the overall rate constant is derived by solving the concentration of each species at the TED as

$$P_2 = 1 - \frac{1}{k_r - k_d}\left[k_r \exp\left(-k_d e_t\right) - k_d \exp\left(-k_r e_t\right)\right] \qquad \text{(eq.3-9)}$$

and tis equation was applied for fitting (Figure 3-12b). The larger error in k_r (15–45%) than that of k_d (3–6%). would be attributed to the difficulty in identification of the progress of rearrangement reaction with minute change in the inter-atom distances and the nature of rearrangement reaction that contains multiple reaction paths.

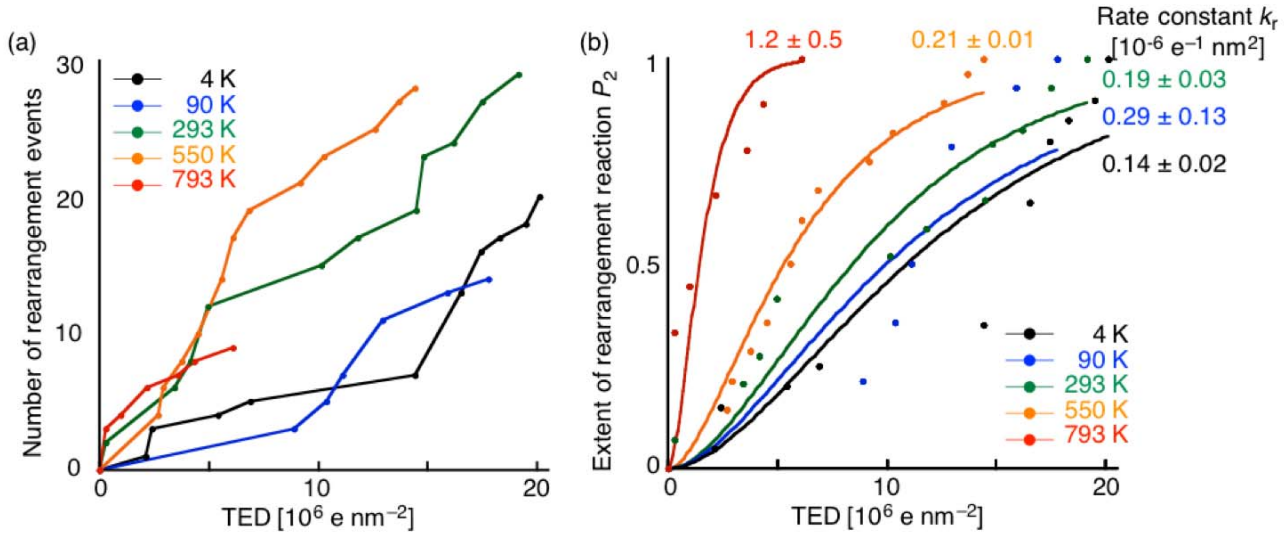

Figure 3-12. Cumulated fullerene dimerization events plotted against TED. (a) Total number of dimerization events. (b) Extent of reaction with fitting curves following eq. 3-9. Colors indicate reactions at 4 (black), 90 (blue), 293 (green), 550 (orange), and 793 K (red) at 120 kV.

The reaction rate at 80 kV, 293 K was 1.5% of that at 120 kV, 293 K, again showing the significant contribution of the electron beam energy onto the reaction kinetics (Figure 3-13). This result imply the existence of activation energy at the PES of radical cation state since 80-keV electrons gives rise to radical cation state with lower vibrational states than that excited by 120-keV electrons.

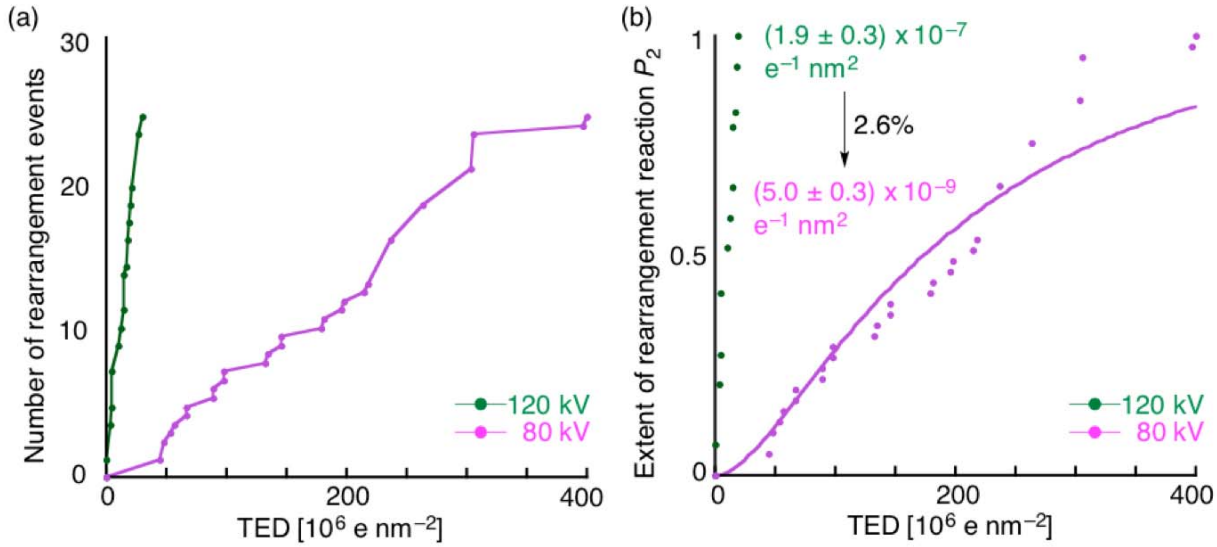

Figure 3-13. Analysis of step 2 reaction at 293 K at 120 kV (green) and 80 kV (purple) plotted against TED. (a) Total number of dimerization events. (b) Extent of reaction with fitting curves following eq. 3-9.

The temperature dependence of k_r was plotted and fitted by

$$k_r = a_r \exp\left(-\frac{E_r}{RT_m}\right) + c_r \qquad \text{(eq.3-10)}$$

where a_r is the pre-exponential factor, E_r is the averaged activation energy of the to several possible paths for path 2, and c_r is the kinetics of path 1 for step 2 reaction, respectively. The fitting explained the temperature dependence of k_r and E_r of 42.6 kJ/mol was obtained (Figure 3-14a). Again, the fitting did not match without c_r as apparent from the fact that k_r is almost constant from 4 to 550 K (Figure 3-14b). The two-paths conclusion was applicable even assuming the deviation of T_m from T_s, and E_r is 49.4 and 72.7 kJ/mol by assuming T_m as 50 or 200 K higher than T_s (Figure 3-14c, d). The difference of step 2 from step 1 is the significantly higher activation energy due to multiple C-C bond cleavage. The trend of the energy barrier would also appear in radical cation PES, requiring high vibrational states to proceed reaction, and resulting in small c_r value of 1.38 x 10^{-7} e^{-1} nm^2 than c_d of 1.72 x 10^{-7} e^{-1} nm^2.

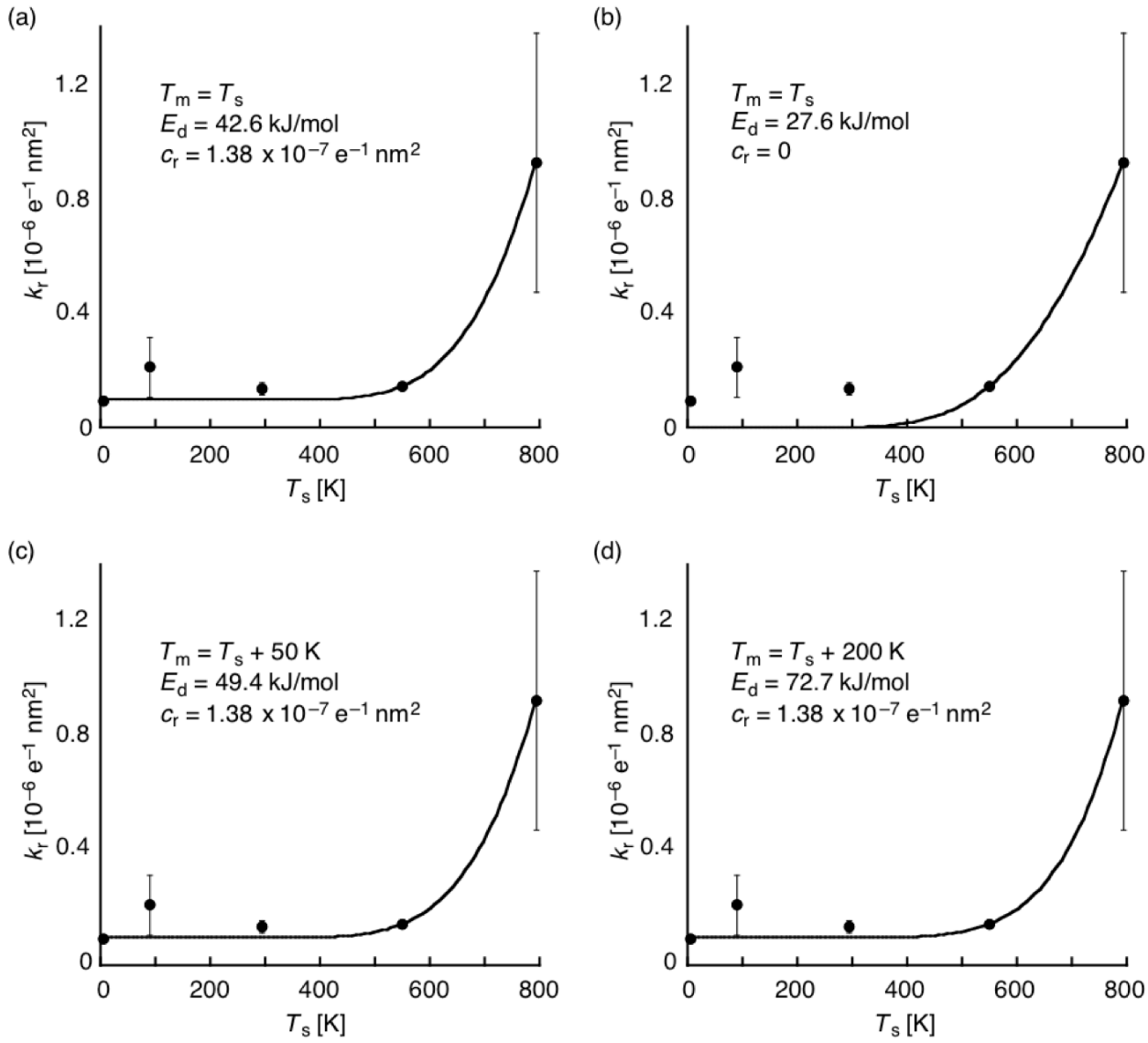

Figure 3-14. Plot and fitting of temperature-dependent reaction rate of step 2. Fitting curves were based on eq. 12 (a) without any modification, (b) fixed c_d value to be zero, (c) assuming $T_m = T_s$ + 50 K, and (d) assuming $T_m = T_s$ + 200 K.

3-7 Conclusion

In summary, I have shown the unimolecular reaction kinetics of C_{60} in one-dimensionally confined space through observation of individual reaction events by SMART-TEM. The VT-SMART-TEM analysis of fullerene dimerization followed by rearrangement revealed the following two facts.

(1) I have proven that the reaction frequency of each molecule follows the statistical reaction theory. The analysis of the reaction events of both step 1 and step 2 revealed that they follow first-order kinetics. Especially, the dimerization reaction of two C_{60} molecules starts from

van der Waals complex and can be considered as a unimolecular reaction. This result shows that molecular diffusion is negligible in the one-dimensionally confined CNT interior. Also, it is noteworthy that the analysis was conducted in yoctomole (10^{-24} mole) scale, and this is the minimum number of molecules involved in kinetics analysis.

(2) Two reaction paths coexists in the chemical reaction under SMART-TEM; thermally activated path from electronic excited state that shows exponential response to temperature, and radical cation path that is insensitive to temperature but sensitive to beam energy. Both paths were explained within the RRKM framework. The latter path is dominant at low temperature, and high vibrational state before thermal relaxation is involved in the reaction events. It is noteworthy that the chemical reaction before thermal relaxation has been so far remained as an imaginary path due to intermolecular collision at conventional experimental conditions.

The discovery of the radical cation path will pave the way toward the deep understanding of the chemistry under TEM, which has been only explained by the atom ejection called knock-on damage. The observation also addresses the applicability of SMART-TEM imaging to trace fast chemical reactions at excited state generated by electron-sample interaction, and indicates further expansion to study photochemistry.

3-8 Experimental section

Data analysis

The reaction data were manually collected from Figure 3-2 and plotted. The weighted nonlinear fitting was performed on KaleidaGraph software.

Derivation of fitting graph in step 2

In order to derive the total rate constant of the two sequential first-order reaction

$$\underset{\text{vdW complex}}{C_{60} + C_{60}} \xrightarrow{k_d} \underset{[2+2]\ \text{dimer}}{C_{60}-C_{60}} \xrightarrow{k_r} \underset{\text{fused dimer}}{C_{120}} \qquad \text{(eq.3-8)}$$

the concentration (i.e. the number of molecules) of each species should be calculated. The consumption of each chemical species is

$$\begin{cases} \dfrac{d}{dt}\left[C_{60}+C_{60}\right] = -k_d\left[C_{60}+C_{60}\right] \\ \dfrac{d}{dt}\left[C_{60}-C_{60}\right] = k_d\left[C_{60}+C_{60}\right] - k_r\left[C_{60}-C_{60}\right] \\ \dfrac{d}{dt}\left[C_{60}-C_{60}\right] = k_r\left[C_{60}-C_{60}\right] \end{cases} \qquad \text{(eq.3-20)}$$

and the concentration is

$$\begin{cases} \left[C_{60}+C_{60}\right] = \left[C_{60}+C_{60}\right]_0 \exp\left(-k_d t\right) \\ \left[C_{60}-C_{60}\right] = \left[C_{60}+C_{60}\right]_0 \dfrac{k_d}{k_r-k_d}\left(\exp\left(-k_d t\right) - \exp\left(-k_r t\right)\right) \\ \left[C_{60}-C_{60}\right] = \left[C_{60}+C_{60}\right]_0 \left(1 - \dfrac{1}{k_r-k_d}\left[k_r \exp\left(-k_d e_t\right) - k_d \exp\left(-k_r e_t\right)\right]\right) \end{cases} \qquad \text{(eq.3-21)}$$

Calculation of C_{60} energy states to evaluate C_{60} ionization by electron beam

Calculation was performed on Gaussian 09 software package at B3LYP/6-31G(d) level of theory.[30]

C_{60} coordinates

SCF Done: E(RB3LYP) = -2286.17415573 A.U. after 15 cycles

Center Number	Atomic Number	Atomic Type	Coordinates (Angstroms) X	Y	Z
1	6	0	1.803154	-0.846281	2.938273
2	6	0	0.638256	-0.172218	3.486966
3	6	0	0.779486	1.251065	3.229073
4	6	0	2.031602	1.456600	2.520258
5	6	0	2.664079	0.160451	2.340403
6	6	0	1.665185	-2.095718	2.332163
7	6	0	2.382259	-2.389787	1.102725
8	6	0	3.209185	-1.423307	0.528625
9	6	0	3.353300	-0.122211	1.160297

10	6	0	3.438077	0.879559	0.110615
11	6	0	2.830602	2.124072	0.283165
12	6	0	2.113326	2.418543	1.512559
13	6	0	0.945966	3.214542	1.172019
14	6	0	-0.256388	3.017045	1.852332
15	6	0	-0.341262	2.015403	2.901812
16	6	0	-1.649646	1.388317	2.819788
17	6	0	-1.785493	0.021653	3.068071
18	6	0	-0.618098	-0.774348	3.408453
19	6	0	0.356290	-2.722431	2.249768
20	6	0	-0.762167	-2.075334	2.776944
21	6	0	3.204784	-1.225717	-0.911318
22	6	0	0.941274	3.411551	-0.267873
23	6	0	-2.373667	2.002570	1.719514
24	6	0	-1.512765	3.009509	1.121568
25	6	0	-2.018463	-2.083568	2.046369
26	6	0	-2.650859	-0.787335	2.226151
27	6	0	1.516888	-3.199009	0.260908
28	6	0	0.264814	-3.404118	0.969627
29	6	0	2.018748	2.083774	-2.046440
30	6	0	2.651201	0.787429	-2.226242
31	6	0	2.373774	-2.002603	-1.719556
32	6	0	1.512707	-3.009493	-1.121631
33	6	0	-1.516926	3.198966	-0.26098
34	6	0	-0.264786	3.404223	-0.969659
35	6	0	-3.346336	-0.197585	1.169683
36	6	0	-3.204734	1.225710	0.911230
37	6	0	-2.106195	-2.738176	0.817059
38	6	0	-0.941258	-3.411492	0.267780
39	6	0	-2.382311	2.389793	-1.102809
40	6	0	-3.209156	1.423271	-0.528677
41	6	0	1.785725	-0.021760	-3.068039
42	6	0	-0.945975	-3.214473	-1.172070
43	6	0	0.256365	-3.017057	-1.852420
44	6	0	0.617967	0.774158	-3.407411
45	6	0	0.341297	-2.015350	-2.901958
46	6	0	-3.438086	-0.879600	-0.110596
47	6	0	-2.830631	-2.124061	-0.283143
48	6	0	-2.113468	-2.418505	-1.512544
49	6	0	-3.353364	0.122077	-1.160293
50	6	0	-0.638553	0.172091	-3.487088
51	6	0	-0.779577	-1.250988	-3.228902
52	6	0	-2.031883	-1.456672	-2.520375
53	6	0	-2.664319	-0.160588	-2.340513
54	6	0	-1.665178	2.095747	-2.332326
55	6	0	2.106274	2.738190	-0.817045
56	6	0	3.346409	0.197621	-1.169660
57	6	0	1.649775	-1.388354	-2.819858
58	6	0	-0.356259	2.722556	-2.249814
59	6	0	-1.803180	0.846150	-2.938165
60	6	0	0.762214	2.075504	-2.776798

Eigenstates [Hartree]

-10.25980	-10.24981	-10.23801	-10.23800	-10.23085	-10.23084	-10.22736	-10.22697
-10.22414	-10.22368	-10.22352	-10.22352	-10.21955	-10.21954	-10.21921	-10.21879
-10.21851	-10.21826	-10.21808	-10.21804	-10.21782	-10.21770	-10.21765	-10.21756
-10.21741	-10.21740	-10.21729	-10.21704	-10.21701	-10.21699	-10.21693	-10.21684
-10.21680	-10.21651	-10.21649	-10.21634	-10.21630	-10.21628	-10.21612	-10.21583
-10.21572	-10.21569	-10.21556	-10.21556	-10.21550	-10.21550	-10.21508	-10.21508
-10.21478	-10.21477	-10.21460	-10.21460	-10.21457	-10.21456	-10.21441	-10.21410
-10.21379	-10.21355	-10.21227	-10.21226				
-0.98967	-0.97242	-0.96994	-0.96211	-0.93459	-0.93235	-0.93220	-0.92502
-0.92054	-0.89790	-0.88900	-0.88509	-0.84944	-0.84816	-0.84644	-0.83977
-0.80396	-0.80153	-0.80081	-0.79762	-0.79645	-0.77729	-0.77587	-0.77528
-0.77144	-0.71973	-0.71873	-0.71770	-0.71752	-0.71439	-0.71381	-0.71339
-0.71180	-0.66763	-0.66506	-0.66355	-0.62939	-0.62777	-0.62652	-0.62349
-0.62234	-0.62093	-0.61969	-0.61815	-0.60605	-0.56399	-0.56259	-0.56211
-0.55765	-0.53310	-0.53249	-0.53146	-0.52803	-0.52701	-0.52155	-0.52063
-0.51656	-0.49319	-0.48948	-0.48564	-0.48378	-0.47244	-0.47173	-0.46988
-0.46940	-0.46928	-0.46669	-0.46281	-0.44722	-0.44565	-0.44511	-0.44385
-0.44076	-0.43114	-0.42765	-0.42543	-0.42520	-0.42465	-0.42436	-0.42377
-0.42297	-0.42197	-0.41921	-0.41735	-0.41487	-0.39965	-0.39831	-0.39554
-0.39228	-0.37088	-0.36783	-0.36688	-0.36230	-0.36062	-0.35942	-0.35918
-0.35739	-0.35024	-0.34918	-0.34902	-0.34782	-0.34592	-0.34025	-0.33829
-0.33495	-0.33426	-0.27369	-0.27286	-0.27146	-0.27134	-0.27131	-0.26788
-0.26633	-0.26448	-0.26388	-0.22165	-0.21770	-0.21446	-0.21268	-0.21123

References

[1] Klán, P.; Wirz, J. *Photochemistry of Organic Compounds: From Concepts to Practice*; John Wiley & Sons: West Sussex, 2009.

[2] (a) Jaffe, H. H.; Miller, A. L. *J. Chem. Educ.* **1966**, *43*, 469–473. (b) Martínez-Fernández, L.; Corral, I.; Granucci, G. *Chem. Sci.* **2014**, *5*, 1336–1347.

[3] Koshino, M.; Niimi, Y.; Nakamura, E.; Kataura, H.; Okazaki, T.; Suenaga, K.; Iijima, S. *Nat. Chem.* **2010**, *2*, 117–124.

[4] Rao, A. M.; Zhou, P.; Wang, K.-A.; Hager, G. T.; Holden, J. M.; Wang, Y.; Lee, W.-T.; Bi, X.-X.; Eklund, P. C.; Cornett, D. S.; Duncan, M. A.; Amster, I. J. *Science* **1993**, *259*, 955–957.

[5] Zobač, V.; Leuis, J P.; Abad, E.; Mendieta-Moreno J. I.; Hapala, P.; Jelínek, P.; Ortega, J. *J. Phys. Condens. Matter* **2015**, *27*, 175002.

[6] (a) Davydov, V. A.; Kashevarova, L. S.; Rakhamianina, A. V.; Senyavin, V. M.; Agafonov, V.; Céolin, R.; Szwarc, H. *JETP Lett.* **1998**, *68*, 628–634. (b) Moret, R.; Launois, P.; Wågberg, T.; Sundqvist, B.; Agafonov, V.; Davydov, V. A.; Rakhamianina, A. V. *Eur. Phys. J. B* **2004**, *37*, 25–37.

[7] Davydov, V. A.; Kashevarova, L. S.; Rakhamianina, A. V.; Senyavin, V. M.; Pronina, O. P.; Oleynikov, N. N.; Agafonov, V.; Céolin, R.; Allouchi, H.; Szwarc, H. *Chem. Phys. Lett.* **2001**, *333*, 224–229.

[8] Bihlmeier, A.; Samson, C. C. M.; Klopper, W. *ChemPhysChem* **2005**, *6*, 2625–2632.

[9] Kaur, N.; Dharamvir, K.; Jindal, V. K. *Chem. Phys.* **2008**, *344*, 176–184.

[10] Hashiguchi, M.; Inada, H.; Matsuo, Y. *Carbon* **2013**, *61*, 418–422.

[11] (a) Shiraishi, M.; Ata, M. *Carbon* **2001**, *39*, 1913–1917. (b) Tanaka, Y.; Hirana, Y.; Niidome, Y.; Kato, K.; Saito, S.; Nakashima, N. *Angew. Chem. Int. Ed.* **2009**, *48*, 7655–7659. (c) Kang, S. J.; Song, Y.; Yi, Y.; Choi, W. M.; Yoon, S. M.; Choi, J. Y. *Carbon* **2010**, *48*, 520–524. (d) Hirana, Y.; Juhasz, G.; Miyauchi, Y.; Mouri, S.; Matsuda, K.; Nakashima, N. *Sci. Rep.* **2013**, *3*, 2959.

[12] Williams, D. B.; Carter, C. B. Inelastic Scattering and Beam Damage. In *Transmission Electron Microscopy*, Springer: New Work, 2009; pp 53–71.

[13] Zimmerman, J. A.; Eyler, J. R.; Bach, S.; McElvany, S. W. *J. Chem. Phys.* **1991**, *94*, 3556–3562.

[14] Vizuete, M.; Gómez-Escalonilla, M. J.; Fierro, J.; Ohkubo, K.; Fukuzumi, S.; Yudasaka, M.; Iijima, S.; Nierengarten, J.-F.; Fernando, L. *Chem. Sci.* **2014**, *5*, 2072–2080.

[15] (a) Kim, D.; Lee, M.; Suh, Y. D.; Kim, S. K. *J. Am. Chem. Soc.* **1992**, *114*, 4430–4432. (b) Guldi, D. M.; Prato, M. *Acc. Chem. Res.* **2000**, *33*, 696–703. (c) Yao, C. B.; Kponou, E.; Zhang, Y.

D.; Wang, J. F. *Opt. Photon. J.* **2011**, *1*, 81–84.

[16] (a) Rudd, M. E.; Goffe, T. V.; Itoh, A. *Phys. Rev. A* **1985**, *32*, 2128–2133. (b) Rudd, M. E.; DuBois, R. D.; Toburen, L. H.; Ratcliffe, C. A. *Phys. Rev. A* **1983**, *28*, 3243–3257. (c) Egerton, R. P. *Rep. Prog. Phys.* **2009**, *72*, 016502.

[17] Koshino, M.; Tanaka, T.; Solin, N.; Suenaga, K.; Isobe, H.; Nakamura, E. *Science* **2007**, *316*, 853.

[18] (a) Solin, N.; Koshino, M.; Tanaka, T.; Takenaga, S.; Kataura, H.; Isobe, H.; Nakamura, E. *Chem. Lett.* **2007**, *36*, 1208–1209. (b) Nakamura, E.; Koshino, M.; Tanaka, T.; Niimi, Y.; Harano, K.; Nakamura, Y.; Isobe, H. *J. Am. Chem. Soc.* **2008**, *130*, 7808–7809. (c) Harano, K.; Homma, T.; Niimi, Y.; Koshino, M.; Suenaga, K.; Leibler, L.; Nakamura, E. *Nat. Mater.* **2012**, *11*, 877–881. (d) Gorgoll, R. M.; Yücelen, E.; Kumamoto, A.; Shibata, N.; Harano, K.; Nakamura, E. *J. Am. Chem. Soc.* **2015**, *137*, 3474–3477.

[19] Harano, K.; Takenaga, S.; Okada, S.; Niimi, Y.; Yoshikai, N.; Isobe, H.; Suenaga, K.; Kataura, H.; Koshino, M.; Nakamura, E. *J. Am. Chem. Soc.* **2014**, *136*, 466–473.

[20] IP of C_{60}. Zimmerman, J. A.; Eyler, J. R.; Bach, S.; McElvany, S. W. *J. Chem. Phys.* **1991**, *94*, 3556–3562.

[21] (a) Smith, B. W.; Luzzi, D. E. *J. Appl. Phys.* **2001**, *90*, 3509–3515. (b) Zobelli, A.; Gloter, A.; Ewels, C. P.; Seifert, G.; Colliex, C. *Phys. Rev. B* **2007**, *75*, 245402.

[22] Chuvilin, A.; Bichoutskaia, E.; Gimenez-Lopez, M. C.; Chamberlain, T. W.; Rance, G. A.; Kuganathan, N.; Biskupek, J.; Kaiser, U.; Khlobystov, A. N. *Nat. Mater.* **2011**, *10*, 687–692.

[23] (a) Nakamura, E.; Koshino, M.; Saito, T.; Niimi, Y.; Suenaga, K.; Matsuo, Y. *J. Am. Chem. Soc.* **2011**, *133*, 14151–14153. (b) Koshino, M. *Dalton Trans.* **2014**, *43*, 7359–7365. For IP, see: (c) Sawamura, M.; Kuninobu, Y.; Toganoh, M.; Matsuo, Y.; Yamanaka, M.; Nakamura, E. *J. Am. Chem. Soc.* **2002**, *124*, 9354–9355. (d) Matsuo, Y.; Kuninobu, Y.; Ito, S.; Nakamura, E. *Chem. Lett.* **2004**, *333*, 68–69. (e) Matsuo, Y.; Fujita, T.; Nakamura, E. *Chem. Asian J.* **2007**, *2*, 948–955.

[24] (a) Chamberlain, T. W.; Champness, N. R.; Schröder, M.; Khlobystov, A. N. *Chem. Eur. J.* **2010**, *17*, 668–674. (b) Chamberlain, T. W.; Meyer, J. C.; Biskupek, J.; Leschner, J.; Santana, A.; Besley, N. A.; Bichoutskaia, E.; Kaiser, U.; Khlobystov, A. N. *Nat. Chem.* **2011**, *3*, 732–737.

[25] Marcus, R. A. *J. Chem. Phys.* **1952**, *20*, 359–364.

[26] (a) Marinov, N. M. *Int. J. Chem. Kinet.* **1999**, *31*, 183–220. (b) Zhao, Z.; Chaos, M.; Kazakov, A.; Dryer, F. L. *J. Chem. Kinet* **2008**, *40*, 1–18. (c) Croiset, E.; Rice, S. F.; Hanush, R. G. *AiCHe J.* **1997**, *43*, 2343–2352.

[27] Wang, H.; Frenklach, M. *J. Phys. Chem.* **1994**, *44*, 11465–11489.

[28] Sheka, E. F. *Chem. Phys. Lett.* **2007**, *438*, 119–126.

[29] (1) Zobač, V.; Lewis, J. P.; Abad, E.; Mendieta-Moreno, J. I.; Hapala, P.; Jelínek, P.; Ortega, J. *J. Phys. Condens. Matter* **2015**, *27*, 175002.

[30] Gaussian 09, Revision **D.01**, Frisch, M. J.; Trucks, G. W.; Schlegel, H. B.; Scuseria, G. E.; Robb, M. A.; Cheeseman, J. R.; Scalmani, G.; Barone, V.; Mennucci, B.; Petersson, G. A.; Nakatsuji, H.; Caricato, M.; Li, X.; Hratchian, H. P.; Izmaylov, A. F.; Bloino, J.; Zheng, G.; Sonnenberg, J. L.; Hada, M.; Ehara, M.; Toyota, K.; Fukuda, R.; Hasegawa, J.; Ishida, M.; Nakajima, T.; Honda, Y.; Kitao, O.; Nakai, H.; Vreven, T.; Montgomery, J. A.; Jr., Peralta, J. E.; Ogliaro, F.; Bearpark, M.; Heyd, J. J.; Brothers, E.; Kudin, K. N.; Staroverov, V. N.; Kobayashi, R.; Normand, J.; Raghavachari, K.; Rendell, A.; Burant, J. C.; Iyengar, S. S.; Tomasi, J.; Cossi, M.; Rega, N.; Millam, J. M.; Klene, M.; Knox, J. E.; Cross, J. B.; Bakken, V.; Adamo, C.; Jaramillo, J.; Gomperts, R.; Stratmann, R. E.; Yazyev, O.; Austin, A. J.; Cammi, R.; Pomelli, C.; Ochterski, J. W.; Martin, R. L.; Morokuma, K.; Zakrzewski, V. G.; Voth, G. A.; Salvador, P.; Dannenberg, J. J.; Dapprich, S.; Daniels, A. D.; Farkas, Ö.; Foresman, J. B.; Ortiz, J. V.; Cioslowski, J.; Fox, D. J. Gaussian, Inc., Wallingford CT, 2009.

Chapter 4. Crystal Nucleation of π-conjugated Donor Molecules Induced on Acidic Substrates

This chapter was published in the following paper and reproduced with the permission from 2015 WILEY-VCH Verlag GmbH & Co. KGaA, Weinheim.

Koji Harano, Satoshi Okada, Shunsuke Furukawa, Hideyuki Tanaka, Eiichi Nakamura "Formation of a Polycrystalline Film of Donor Material on PEDOT:PSS Buffer Induced by Crystal Nucleation", *Journal of Polymer Science Part B: Polymer Physics* **2014**, *52*, 833–841.

4-1 Introduction

Poly(3,4-ethylenedioxythiophene): poly(styrene sulfonate) (PEDOT:PSS) is one of the standard anode buffer materials in organic photovoltaic (OPV) solar cells.[1] Its water-solubility, hole transparency, appropriate valence band energy level of 5.3 eV,[2] and surface smoothness are beneficial to work as an interlayer between indium tin oxide (ITO) substrate[3] and the organic donor layer despite the degradation of ITO by the acidity of PEDOT:PSS.[4] The benefits to improve inorganic-organic contact are well studied, while the other interface; organic-organic interface has not been well understood although underlayer of donor molecules plays a major role in determination of film morphology.[5] This is because of the methodological inaccessibility to investigate the interface and appropriate models to investigate interfacial interactions.

The state-of-the-art scanning electron microscopy (SEM) with < 1 nm spatial resolution was found to be a powerful methodology for investigation of organic-organic interfaces. It enables imaging of the surface details without any metallic coatings.[6] A small-molecule OPV system using 21*H*,23*H*-tetrabenzo[*b*,*g*,*l*,*q*]porphyrin (BP) as a donor molecule was selected as a structural model to study interface due to a robust crystalline structure and solvent-insoluble nature of BP.[7]

Using this system, I show that PEDOT:PSS induces crystal nucleation of BP on its surface to obtain polycrystalline film with uniform thickness. PEDOT:PSS possesses acidic sites and they nucleate BP, as confirmed by the appearance of submicron dispersed crystal morphologies on graphitic surfaces that lack acidic sites (Figure 4-1). Similar acid-base mechanism was also found in polymer system using poly(3-hexylthiophene) (P3HT) as a donor material, which is a standard polymer used as an electron donor in OPVs. These results indicate that the chemical interaction at organic-organic interface is critical to control crystallization and the final morphology.

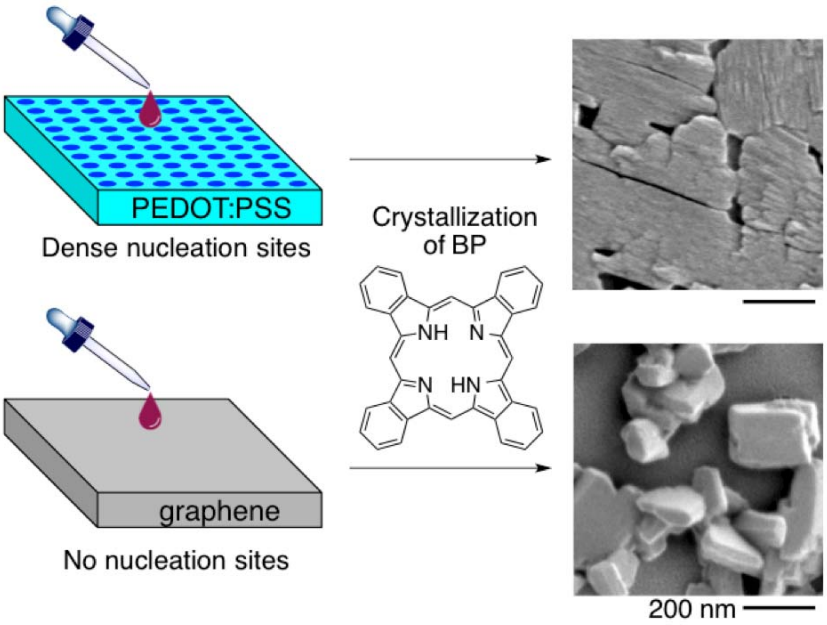

Figure 4-1. A schematic image of morphological change of tetrabenzoporphyrin thin films depending on the density of nucleation sites.

4-2 Surface Morphology of BP on Various Substrates

Crystalline BP film was fabricated following the published procedure, from its 0.5-wt% precursor 1,4:8,11:15,18:22,25-tetraethano-29*H*,31*H*-tetrabenzo[*b*.*g*.*l*.*q*]porphyrin (CP) solution in chloroform/chlorobenzene mixture spin-coated on the substrates and heated at 180 °C for 20 min to remove four ethylene molecules by retro-Diels-Alder reaction (Figure 4-2). As substrates, PEDOT:PSS, ITO and highly oriented pyrolytic graphite (HOPG) were initially selected. Among these substrates, PEDOT:PSS exposes acidic sites on their surfaces.

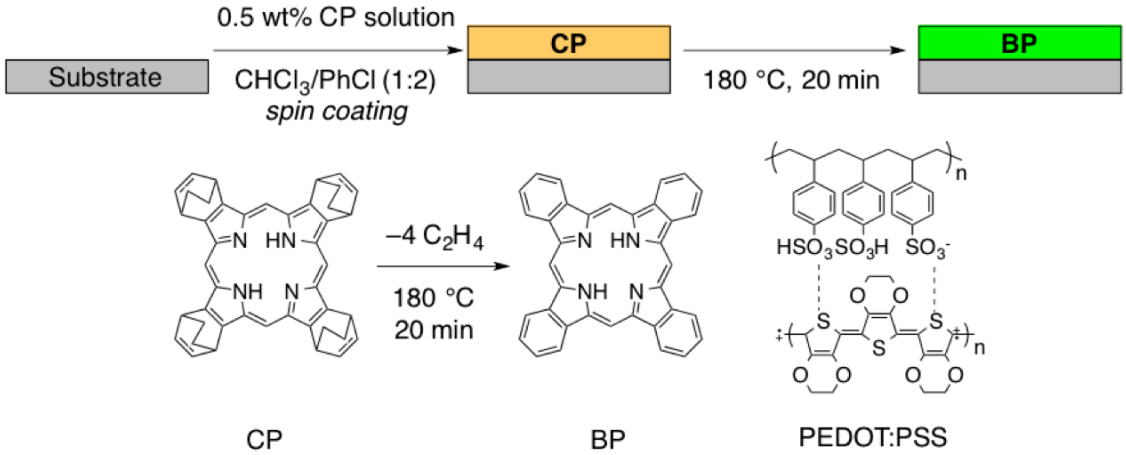

Figure 4-2. A general procedure to fabricate BP films and structures of materials.

The low landing voltage imaging enabled analysis of surface fine structure.[8] Low landing

voltage was achieved by applying electric bias in the opposite direction to that of the electron beam. Here 1-kV electron beam was irradiated to the sample specimen with 800-V anti-bias to achieve 200-V landing voltage. The mean-free path of electrons at 200 V of organic molecules are 0.8–1.0 nm and the position of secondary electrons generated after multiple scattered events (SE2) does not deviate from those from the incident beam position (SE1), while the mean free path at 1 kV is 2.5–3.5 nm and generation position of SE2 deviates from that of SE1 much (Figure 4-3).[9] In addition, the emission yields of secondary electrons become close to 1 at low landing voltage typically around 200–500 V, contributing suppression of charging up.[10] Therefore, the surface sensitive imaging is achieved at low landing voltage without metallic coating that deteriorate single-nm morphology of the specimen.

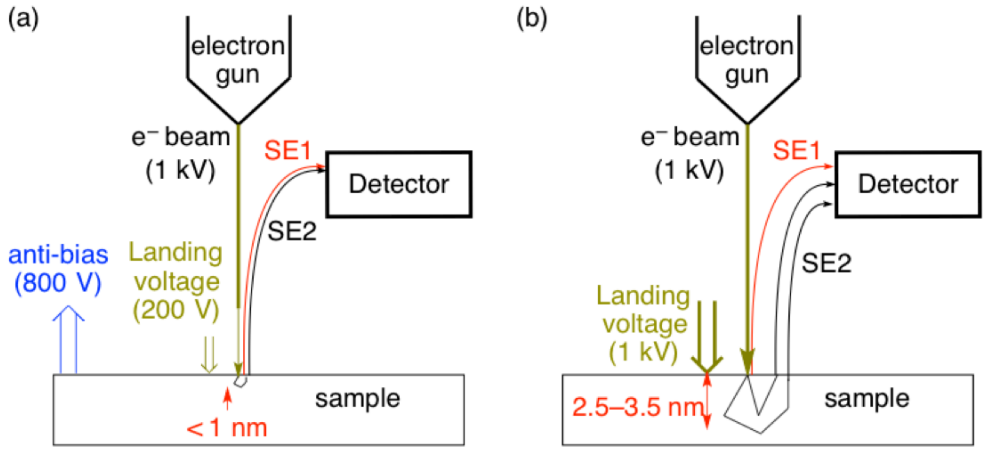

Figure 4-3. SEM observation at low landing voltage. (a) Landing voltage of 200 V is applied by decelerating 1-kV electron beam with 800-V anti-bias. (b) 1-kV electron beam is applied without anti-bias.

The SEM images of the BP crystals are classified into two morphologies, flat film and submicron crystals. Flat film morphologies were observed on PEDOT:PSS with the typical crystal size of 10 nm × 100 nm (Figure 4-4a). On ITO, flat morphologies with the typical crystal size of 50 nm × 150 nm and submicron crystals were observed (Figure 4-4b). On HOPG, submicron crystalline morphologies were only observed (Figure 4-4c). These morphological difference originates from the nature of the substrate; PEDOT:PSS possesses acidic and flat surface, ITO has neutral and rough surface, and HOPG surface is neutral and flat. Some reports insist that the surface roughness induces nucleation,[11] and the observed two morphologies on ITO would be originating from the surface roughness and the inhomogeneity of columnar ITO domains.

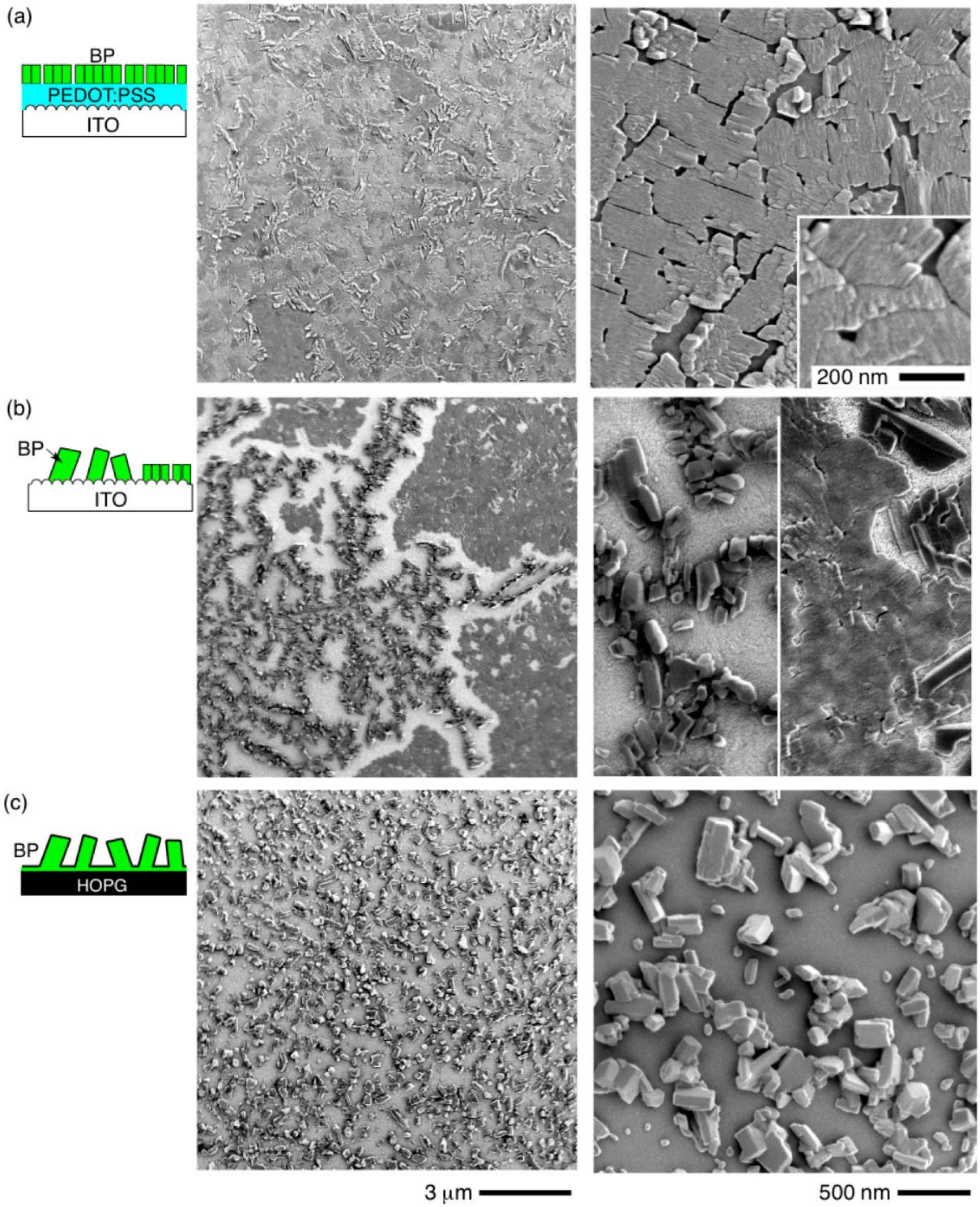

Figure 4-4. Top view SEM images of BP crystals. (a) PEDOT:PSS, (b) ITO, and (c) HOPG were used as substrates.

4-3 Crystallization of BP on Graphene-Coated PEDOT:PSS[12]

4-3-1 Surface Modification of PEDOT:PSS with Graphene

The smooth morphology of BP on PEDOT:PSS was assumed to be due to the acidic sites on the surface that induce crystal nucleation by chemically interacting with the porphyrin core of BP that can accept protons. In order to prove this hypothesis, the surface of PEDOT:PSS was covered by chemically neutral thin layer, graphene. Graphene was selected because of its high electron conductivity that do not interfere charge transport,[13] chemically neutral surface, and the possibility of surface functionalization for solution processing.[14] In order to utilize the solution processability, I selected the chemical exfoliation followed by thermal reduction that enables large-scale preparation.[15]

Dispersible graphene precursor was synthesized by modified Hummers' method[16] followed by functionalization with isothiocyanate to obtain phenyl-modified graphene oxide flakes (Ph-iGO) that disperses in organic solvents such as DMF and DMSO (Scheme 4-1). The size of Ph-iGO was confirmed by dynamic light scattering (DLS) to be 917 ± 78 nm. The single-layered nature was confirmed by atomic force microscopy (AFM) and molecular model. AFM image shows the 450-nm wide, 0.6-nm thick curled film morphology, and a simulated molecular model shows that this thickness corresponds to monolayer of Ph-iGO (Figure 4-5).

Scheme 4-1. Synthesis of graphene oxide and its derivatives

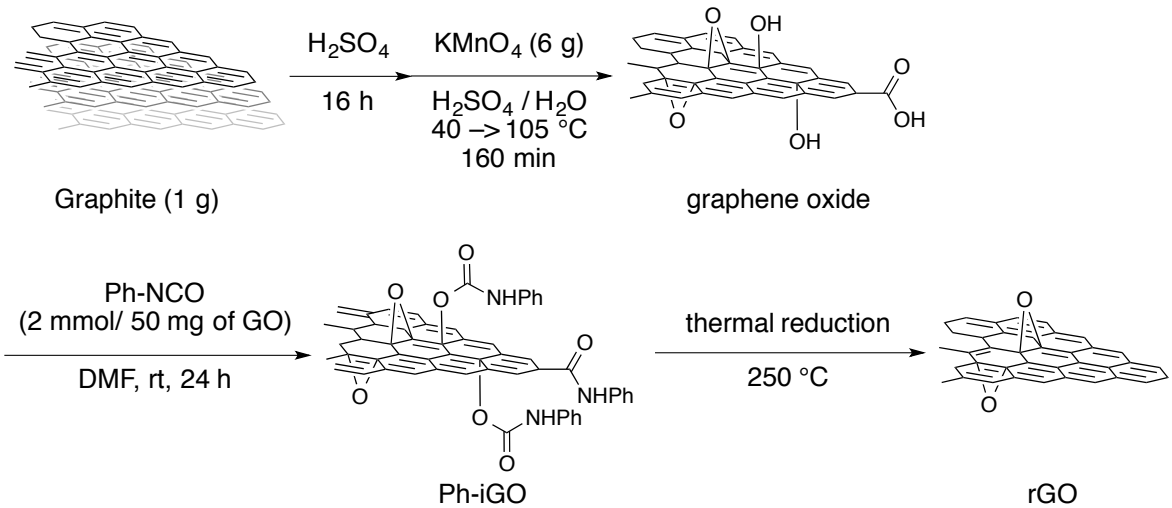

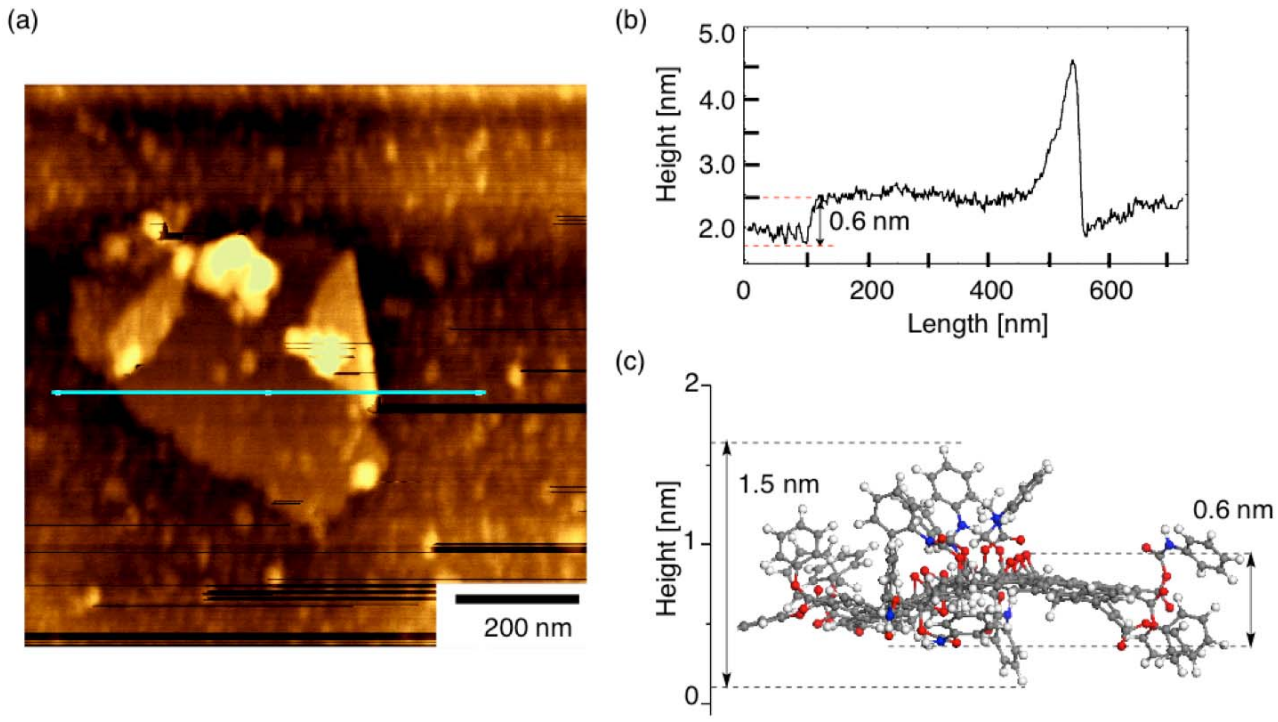

Figure 4-5. An AFM image of a single layered sheet of Ph-iGO on mica. (a) Topographic image and (b) Height profile of the blue line in (a). (c) Ball and stick structural modeling of Ph-iGO after structural optimization. White: hydrogen, gray: carbon, red: oxygen, blue: nitrogen.

Thermal defunctionalization of Ph-iGO was observed by thermogravimetric (TG) analysis under nitrogen or dry air gas flow (Figure 4-6a). TG analysis showed that defunctionalization proceeded mainly at 170–220 °C. After heating at 300 °C, reduced graphene oxide (rGO) was obtained as a black powder and dispersibility in solvents was lost. Infrared (IR) spectrogram showed that broad signals at 3300 cm^{-1} disappeared and peaks at 1000–1600 cm^{-1} became weak in rGO, indicating the partial removal of functional groups. (Figure 4-6b). Elemental analyses and IR spectroscopy suggested that the remained functional groups contain epoxides and carbonyl groups remained (Table 4-1). Since PEDOT:PSS degrades at > 280 °C in nitrogen atmosphere,[17] the defunctionalization temperature was set at 250 °C, at which point most of the functional groups are removed.

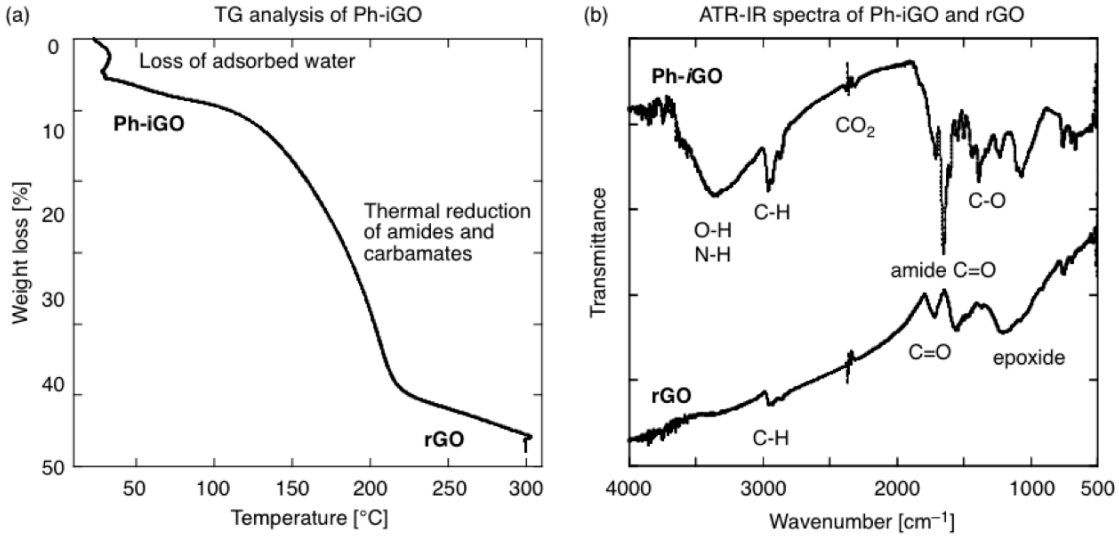

Figure 4-6. Thermal reduction of Ph-iGO into rGO. (a) TG analysis of Ph-iGO. (b) IR spectra before (Ph-iGO) and after (rGO) TG analysis.

Table 4-1. Elemental analysis and C/N ratio of functionalized graphenes. GO: before functionalization by phenyl isocyanate; Ph-iGO and rGO: before and after TG analysis.

	C [%]	H [%]	N [%]	C/N
GO	41.50	3.64	0	–
Ph-iGO	52.50	3.52	4.22	7.51
rGO	70.76	2.24	2.82	22.27

The ITO/PEDOT:PSS substrate was coated with a Ph-iGO dispersion in DMF followed by thermal decomposition. Ph-iGO dispersion in DMF was initially centrifuged and the supernatant was used to avoid μm-sized aggregates. The surface coverage of clearly visible Ph-iGO layers was controlled by the number of spin coating process (Figure 4-7). Dark-contrasted regions observed in SEM have various contrasts, indicating that these objects are multilayered Ph-iGO. Thus obtained PEDOT:PSS/Ph-iGO substrates were heated at 250 °C to convert into PEDOT:PSS/rGO.

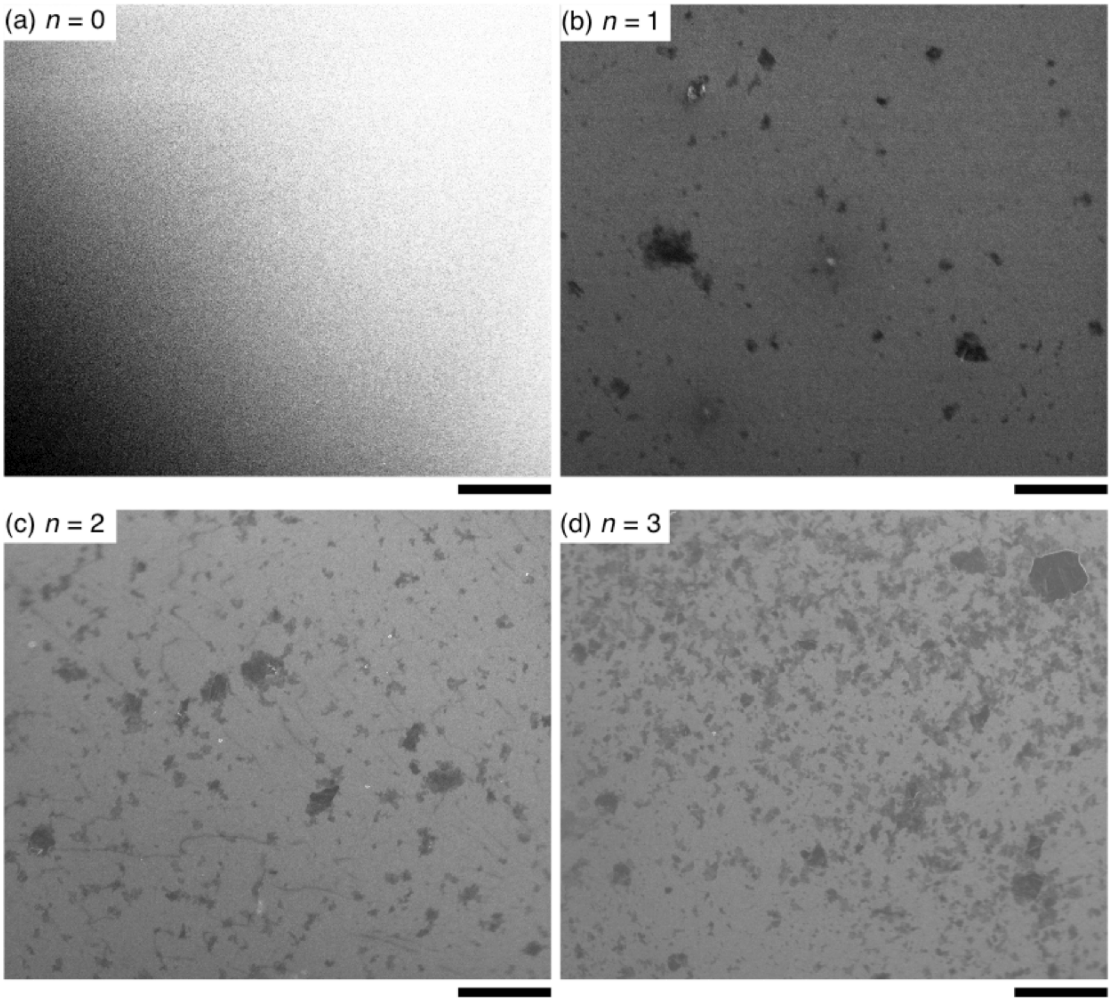

Figure 4-7. SEM images of Ph-iGO flakes on ITO/PEDOT:PSS surface. (a) ITO/PEDOT:PSS, (b)-(d) ITO/PEDOT:PSS/Ph-iGO with different times of spin-coating of Ph-iGO dispersion in DMF. Scale bars: 5 μm.

4-3-2 Crystal Morphologies of BP on Graphene-Coated PEDOT:PSS

The SEM images of BP morphologies on ITO/PEDOT:PSS/rGO is shown in Figure 4-8. Dispersed submicron crystals of BP were only observed on ITO/PEDOT:PSS/rGO prepared by three times coating of Ph-iGO, while both polycrystalline morphology and dispersed submicron crystals were observed on ITO/PEDOT:PSS/rGO prepared by coating Ph-iGO once (Figure 4-8). This indicates that some PEDOT:PSS is exposed to the surface when Ph-iGO was coated once, and three times coating totally changed the surface properties. This also proves that the surface acidity contributes to the crystal nucleation of BP.

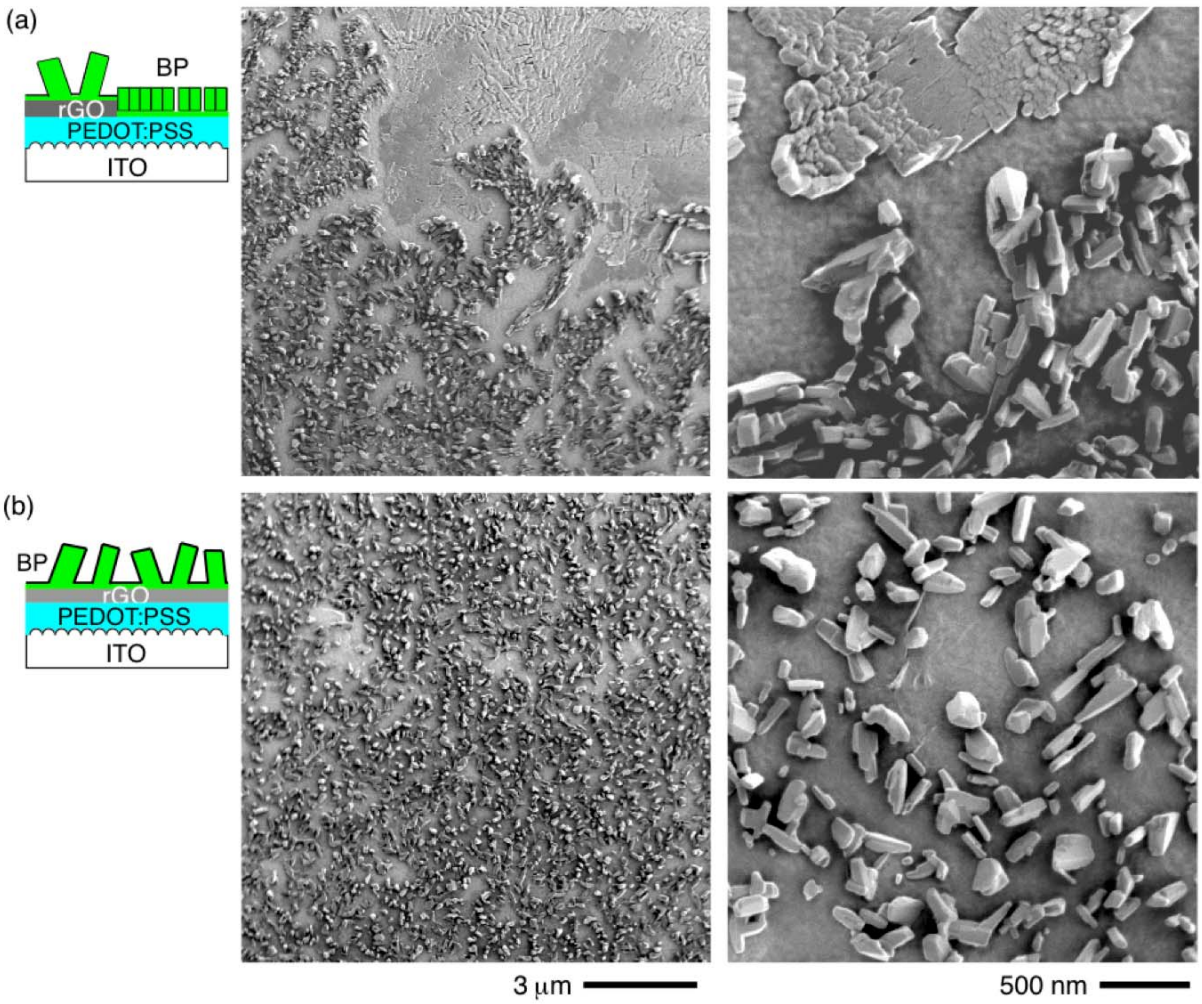

Figure 4-8. SEM images of BP on rGO-coated PEDOT:PSS. BP was fabricated on PEDOT:PSS/rGO prepared by coating Ph-iGO dispersion (a) once and (b) three times.

4-3-3 Crystal Orientations of BP

The crystallinity of BP films was investigated by glazing incidence X-ray diffraction (GIXD, Figure 4-9). The signals were assigned as (002), (012), (004), (114) from small diffraction angle θ, respectively, by comparison with the single crystal diffractogram of BP.[18] The matching of GIXD spectra with single crystal pattern spectra of bulk BP crystal showed the same polymorph of the nanocrystals as bulk state. The small deviation in the GIXD spectra indicates the minor change in the habit of crystal orientation by insertion of rGO underlayer. This supports the hypothesis that the crystal nucleation is induced on PEDOT:PSS surface, not on graphitic rGO surface.

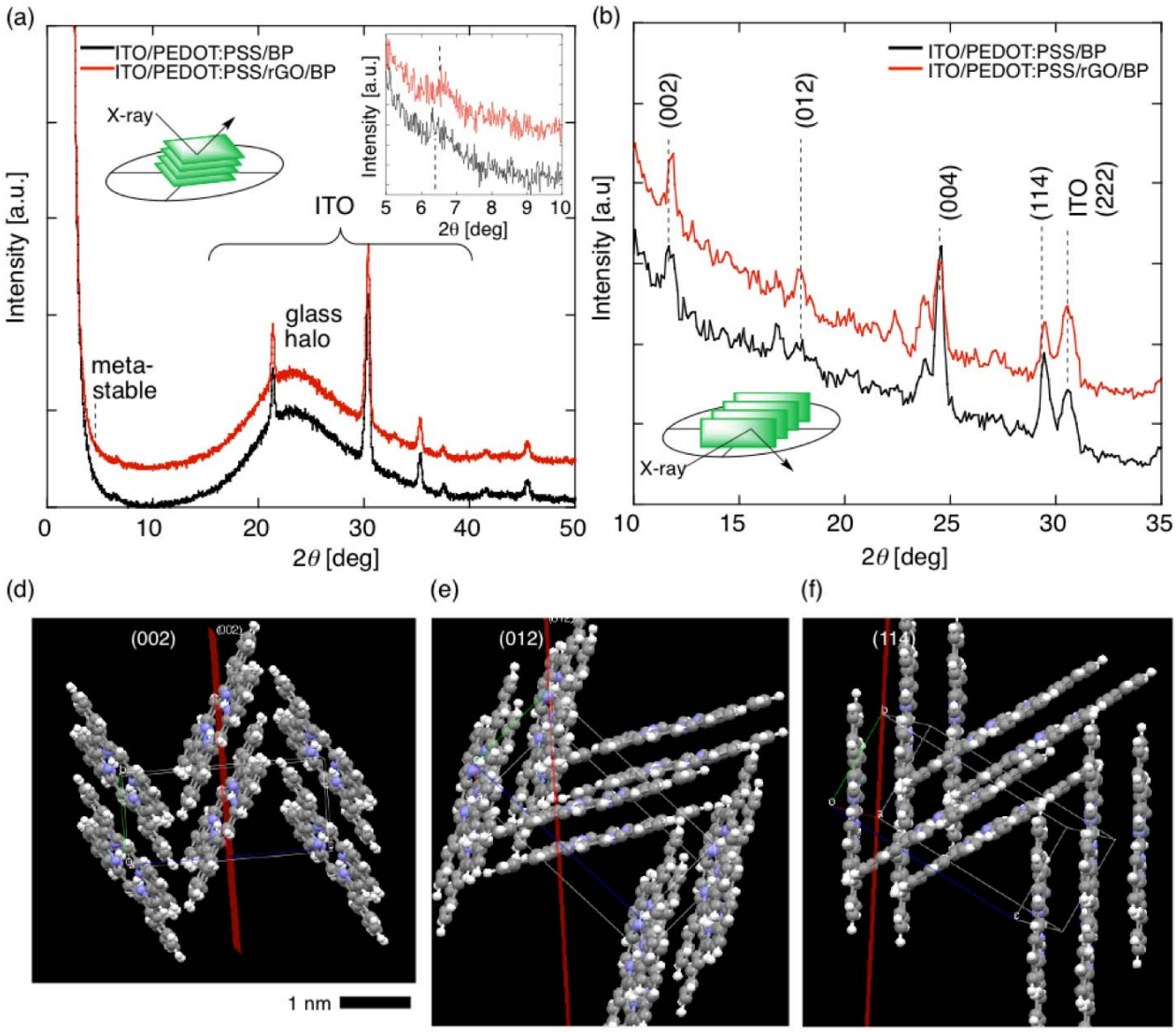

Figure 4-9. GIXD spectra of ITO/PEDOT:PSS/BP (black line) and ITO/PEDOT:PSS/rGO/BP (red line). (a) Out-of-plane and (b) in-plane spectra. (c-e) Molecular orientation of BP crystals. Red lines show (002), (012), and (114) planes, respectively.

4-4 Mechanism of Crystallization

The morphologies on PEDOT:PSS and on graphite is explained by acid-base interaction between PEDOT:PSS and BP (Figure 4-10). Porphyrin core of BP has a typical pKa of 3.9 and 4.4 for di- and mono-protonation,[19] and benzenesulfonic acid moiety in PSS is less than –1 (cf. toluenesulfonic acid: < –1.3).[20] Therefore, BP is protonated at the PEDOT:PSS-BP interface to fix the BP. Those protonated species have deeper HOMO and LUMO energies than those of neutral BP (Table 4-2), and the donor-acceptor interaction between BPH_n^{n+} (n = 1, 2) and BP accelerates aggregation of BP, or BPH_n^{n+} acts as a crystal nuclei. The flat nature of the obtained BP film

indicates that crystal nucleation and growth took place at the same rate. When PEDOT:PSS is covered with rGO, the acid-base interaction is inhibited and nucleation becomes sporadic as observed on HOPG. The rare appearance of crystals on rGO-covered surface is also indicated by the winkles on ITO/PEDOT:PSS/rGO/BP surface where BP crystals are absent. One may think that graphitic surface also possesses CH-π and π-π interactions, but these species are mobile on two-dimensional surface and do not contribute to nucleation.

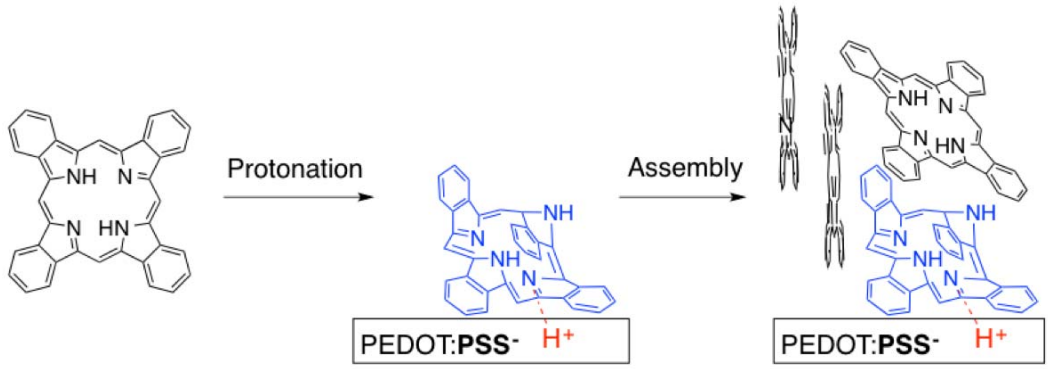

Figure 4-10. Schematic illustration of BP crystal nucleation mechanism on PEDOT:PSS.

Table 4-2. Energy levels of BP and their cation.

	BP	BPH^+	BPH_2^{2+}
LUMO+1	–2.23	–6.00	–9.72
LUMO	–2.25	–6.01	–9.72
HOMO	–5.16	–8.99	–12.70
HOMO–1	–7.21	–10.94	–12.74

In order to show the flat morphology on dense nucleation sites, polycrystalline BP on PEDOT:PSS was applied as a substrate where epitaxial nucleation of BP uniformly takes place. BP was solution processed on BP flat film and the obtained morphology was identical to that of the underlayer (Figure 4-11). This supports the hypothesis that flat polycrystalline film morphology is obtained on substrates with dense nucleation sites.

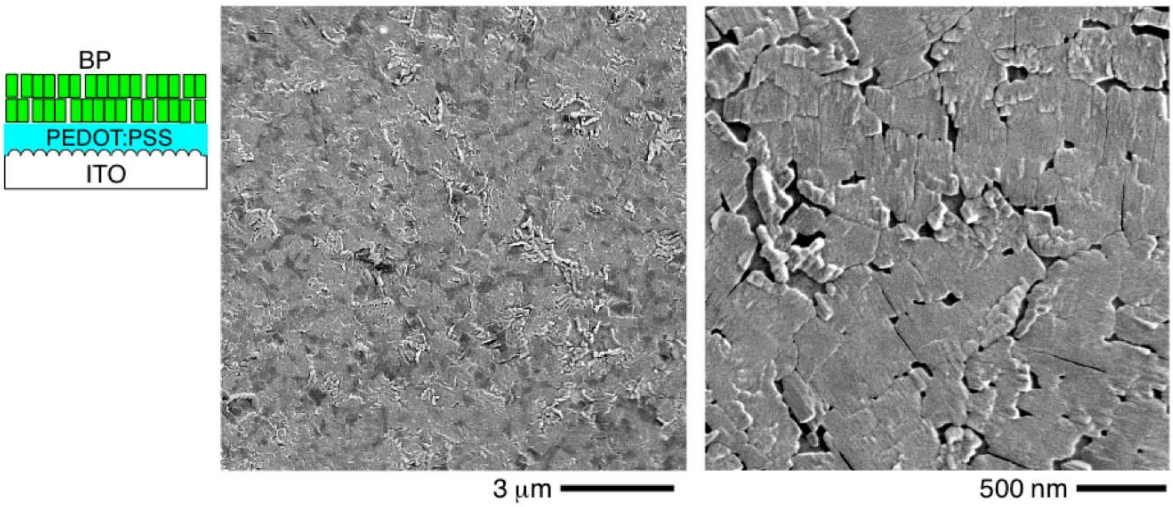

Figure 4-11. SEM images of BP fabricated on polycrystalline BP on PEDOT:PSS.

4-5 Film Morphology of P3HT

The similar morphological change was observed for P3HT, a polymer donor molecule in OPVs (Figure 4-12). Chlorobenzene solution of P3HT was spin-coated onto ITO/PEDOT:PSS and on HOPG and heated at 150 °C to remove solvents. On PEDOT:PSS, P3HT formed an uniform polycrystalline domains with the grain size of 22 ± 2 nm with the film thickness of 16 ± 8 nm. On the other hand, droplet domains with the diameter of 195 ± 10 nm were observed on HOPG. The morphology on HOPG is typically observed for polymers without interaction with substrates.[21] This shows that 3-hexylthiophene unit in P3HT interacted with PEDOT:PSS to form dense domains. The interaction between P3HT and PEDOT:PSS may be proton-mediated electrostatic interaction or multipoint van der Waals interaction between hexyl chains and PEDOT:PSS.

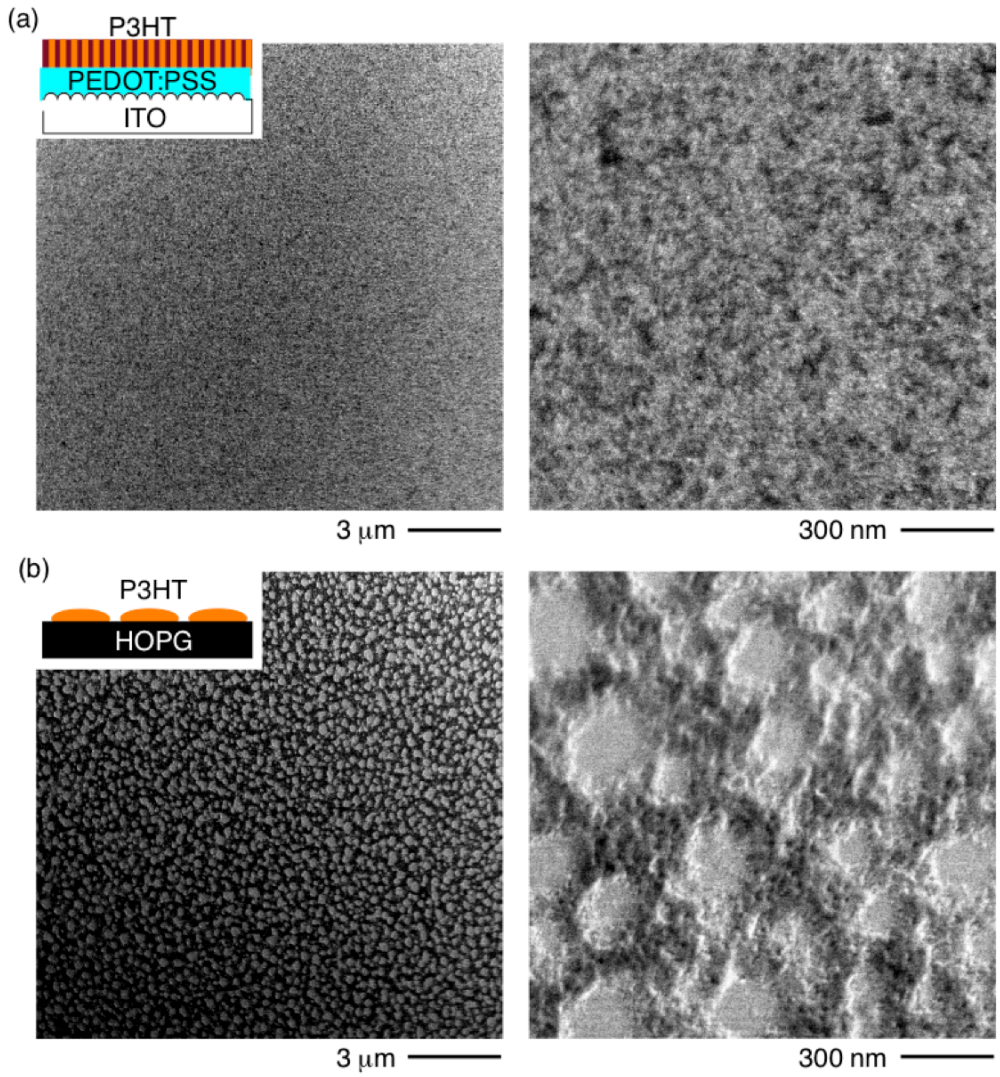

Figure 4-12. SEM images of P3HT films. (a) PEDOT:PSS and (b) HOPG were used as substrates.

4-6 Conclusion

In summary, I have shown that the PEDOT:PSS surface promotes heterogeneous nucleation of two typical donor materials BP and P3HT. Thus obtained nucleation sites promote aggregation and crystallization of donors to obtain uniform and flat film morphologies. The acid-base interaction played a key role in the crystallization, and the randomly crystallized domains were obtained on graphitic surfaces without nucleation sites. This result implies the possibility to explain the morphological control of thin films for OPVs based on the density of crystal nucleation sites, such as the morphological control over lead halide perovskite used for OPVs by surface modification with ionic groups that act as nucleation sites.[22]

4-7 Experimental Section

General.

SEM was performed on a FEI Magellan 400L at an acceleration voltage of 1 kV and anti-bias of 800 V on the sample so that the settling voltage become 200 V under reduced pressure of 5×10^{-5} Pa at the working distance of 1.5–2.0 mm. AFM was performed on an SII SPI-3800 instrument with a silicon cantilever (MikroMasch, NSC-35 Al BS, resonant frequency 120–190 kHz). GIXD was performed on Rigaku SmartLab X-ray diffractometer using CuK_{α} (radiation wavelength, 1.5418 Å). IR spectra were recorded on a JASCO FT-IR- 6100 spectrometer equipped with attenuated total reflectance with zinc selenide crystals and are reported as wavenumber (v) in cm^{-1}. TG analyses were performed on a Rigaku Co. Thermo Plus 2 TG8120 system at a heating rate of 10 K min^{-1} from 30 °C to 300 °C. All analyses were performed with the supplied instrument software. DLS measurement was performed on a Malvern Zetasizer Nano ZD machine. Correlation data were fitted using the method of cumulants[23] to the logarithm of the correlation function, yielding the diffusion coefficient, *D*. The hydrodynamic diameters of the nanoparticles were calculated using *D* and Stokes–Einstein equation ($D = k_B T/3\pi\eta d$, where k_B is the Boltzmann constant, *T* is the absolute temperature, η is the solvent viscosity, and *d* is the diameter of the particle). CONTIN algorithms were used in the Laplace inversion of the autocorrelation functions to confirm particle size distributions. Sonication was performed on an Iuchi Seieido US-4 ultrasonic cleaner. The ultrasonication experiment was performed on a TOMY UD-201 ultrasonic disruptor. Freeze-drying was performed on an EYELA FDU-1200 freeze dryer. Energy calculation was performed on Gaussian 09 software package at B3LYP/6-31G(d) level of theory.[24]

Materials.

Graphite was purchased from Aldrich (< 20 μm, Batch #14317HB). Distilled water was purified further with a Millipore Milli-Q purification system before use. Phenyl isocyanate was purchased from Kanto Chemical Co., Inc. and distilled before use. Anhydrous DMF for the reactions was purchased from Kanto Chemical Co., Inc. and was dried over 4 Å molecular sieves. DMF for dispersing Ph-iGO was filtered through a membrane filter (Advantec, 0.2 μm). Graphene oxide was dispersed in ultrapure water and freeze-dried before use. An aqueous solution of PEDOT:PSS (Clevios P VP AI4083) was filtered through a autovial with the pore size of 0.45-μm before use. P3HT was purchased from Aldrich (Mn 45000–65000, 99.995% trace metals basis). Other chemicals were purchased from Aldrich Inc., Kanto Chemical Co., Inc., and other commercial suppliers, and they were used without further purification.

ITO/BP

ITO glass was cleaned ultrasonically using a surfactant, rinsed with water, and treated with UV/ozone for 3 min. The CP solution in a chloroform/chlorobenzene mixture (1:2 weight ratio, 0.5 wt %) was spin-coated (1500 rpm, 30 sec) and then heated at 180 °C for 20 min.

ITO/PEDOT:PSS

ITO glass was cleaned ultrasonically using a surfactant, rinsed with water, and treated with UV/ozone for 3 min. PEDOT:PSS dispersion was spread uniformly on ITO substrates, spin-coated (3000 rpm, 30 sec), and annealed at 120 °C for 10 min under ambient condition.

ITO/PEDOT:PSS/BP

On ITO/PEDOT:PSS, CP solution in a chloroform/chlorobenzene mixture (1:2 weight ratio, 0.5 wt %) was spin-coated (1500 rpm, 30 sec) and then heated at 180 °C for 20 min.

HOPG/BP

On a freshly cleaved HOPG substrate (4 mm × 4 mm), CP solution in a chloroform/ chlorobenzene mixture (1:2 weight ratio, 0.5 wt %) was spin-coated (1500 rpm, 30 sec) and then heated at 180 °C for 20 min.

Preparation of graphene oxide flakes[25]

Graphite (1.0 g) was ground by mortar and pestle with NaCl (50 g) for 10 min, 250 mL of water was added to the mixture, and the mixture was sonicated for 1 min to dissolve NaCl and then filtered through filter paper. Some of the graphite remained on the filter paper. Sulfuric acid (23 mL) was added to the ground graphite, and the mixture was stirred for 16 h at room temperature. At a temperature < 20 °C, potassium permanganate (6.0 g) was added slowly, and the mixture was heated to 40 °C for 30 min. The reacting mixture was then heated to 90 °C and stirred for 90 min. At a temperature < 20 °C, water (46 mL) was added, and the mixture was heated to 105 °C and stirred for 40 min. H_2O_2 (30% solution, 10 mL) with water (140 mL) was added, and the reaction mixture was stirred for 20 min at room temperature. The resulting mixture was filtered by suction, washed with 1 M HCl aq (30 mL) and Milli-Q water (30 mL), and dried under vacuum to obtain the title compound (0.734 g) as a brown solid. Elemental analysis: C, 47.69%; H, 2.15%. IR (powder) 3590 (s, br), 3119 (s, br), 1727 (s), 1618 (s), 1502 (w), 1424 (w), 1219 (m), 1164 (m), 1049 cm^{-1} (s). The size of graphene oxide flakes can be reduced from 4425 ± 470 nm to 916 ± 78 nm by probe sonication for 50 min.

Preparation of Ph-iGO[26]

A dispersion of graphene oxide (501 mg) in DMF (50.0 mL) and phenyl isocyanate (2.43 g, 20.4 mmol) was stirred for 24 h at room temperature under nitrogen atmosphere. The reaction mixture was added to dichloromethane (500 mL), filtered, washed with dichloromethane (100 mL), and dried under vacuum to obtain the title compound (562 mg) as a black solid. AFM and DLS analysis indicated that the individual Ph-iGO sheet was several hundreds of nanometers in diameter and < 1 nm in height. Elemental analysis: C, 52.50%; H, 3.52%; N, 4.22%. IR (powder) 3367 (s, br), 2957 (s), 2929 (s), 2871 (s), 1706 (m), 1648 (s), 1599 (m), 1496 (m), 1437 (m), 1417 (m), 1386 (m), 1350 (m), 1312 (m), 1227 (m), 1100 (m), 1064 (m), 756 (m), 692 (m), 662 cm^{-1} (m).

Thermal Conversion of Ph-iGO to Reduced Graphene Oxide (rGO)

Ph-iGO lost most of the phenyl carbamate groups at 250 °C, which is lower than the decomposition temperature of PEDOT:PSS (280 °C),[27] to give insoluble rGO as analyzed by IR and TGA. Upon heating to 300 °C (heating rate: 10 K min^{-1}) in the TG analysis, Ph-iGO (4.80 mg) yielded rGO (2.49 mg) as a black solid. Elemental analysis: C, 70.76%; H, 2.24%; N, 2.82%. IR (powder) 2926 (w), 2927 (w), 2861 (w), 2871 (s), 1717 (m), 1561 (m), 1203 (m), 911 (m), 753 (m), 690 cm^{-1} (m). The elemental analysis shows the removal of 66% of the carbamates and amides.

Preparation of Ph-iGO Dispersion in DMF

Ph-iGO (20 mg) was added to DMF (10 mL) and sonicated for 30 min. The obtained dark-brown dispersion was centrifuged at 3000 rpm for 30 sec, and the supernatant was collected as a gray dispersion.

ITO/PEDOT:PSS/rGO/BP[7a]

ITO/PEDOT:PSS substrate was prepared according to the literature. Ph-iGO dispersion in DMF was spread uniformly onto the ITO/PEDOT:PSS substrate, spin-coated (1500 rpm, 30 sec), and heated at 150 °C for 10 min under an ambient condition. After one or three coatings of Ph-iGO, the substrate was transferred into a glove box filled with nitrogen. On the rGO-coated ITO/PEDOT:PSS substrate, the CP solution in a chloroform/chlorobenzene mixture (1:2 weight ratio, 0.5 wt %) was spin-coated (1500 rpm, 30 sec) and then heated at 180 °C for 20 min.

ITO/PEDOT:PSS/BP/BP

ITO/PEDOT:PSS/BP substrate was prepared according to the literature.9 On the ITO/PEDOT:PSS/BP substrate, CP solution in a chloroform/chlorobenzene mixture (1:2 weight ratio, 0.5 wt %) was spin-coated (1500 rpm, 30 sec) and then heated at 180 °C for 20 min.

ITO/PEDOT:PSS/P3HT

P3HT in chlorobenzene (0.2 wt %) was spin-coated (1500 rpm, 30 sec) onto ITO/PEDOT:PSS substrate and heated at 150 °C for 3 h under an ambient condition.

HOPG/P3HT

On a freshly cleaved HOPG substrate (4 mm 3 4 mm), P3HT in chlorobenzene (0.2 wt %) was spin-coated (1500 rpm, 30 sec) and heated at 150 °C for 3 h under an ambient condition.

SEM observation

SEM observation was performed on a FEI Magellan 400L instrument at 5×10^{-5} Pa. The working distance was set to 1.5 mm. Secondary electrons were collected with a through- lens detector. Observation at a beam landing voltage of 200 V was performed using beam deceleration, where 800 V of beam deceleration bias was applied to the primary electron beam accelerated at a voltage of 1 kV.

Energy and coordinates of neutral and acidified BP

BP

SCF Done: E(RB3LYP) = -989.577740967 A.U. after 9 cycles

Center Number	Atomic Number	Atomic Type	Coordinates (Angstroms) X	Y	Z
1	6	0	-3.204144	-1.633875	-0.735977
2	6	0	-1.870035	-1.130063	-0.894025
3	6	0	-1.785750	0.064282	-0.224232
4	6	0	-3.065263	0.332558	0.366940
5	1	0	-1.090981	-1.631201	-1.451833
6	1	0	-0.925500	0.713530	-0.136599
7	6	0	-7.124655	-3.474684	-0.489110
8	6	0	-6.821963	-4.660742	-1.285320
9	6	0	-5.522640	-4.545305	-1.656109
10	6	0	-5.046081	-3.289848	-1.082582
11	7	0	-6.034159	-2.663370	-0.382439
12	1	0	-7.519403	-5.455988	-1.515588
13	1	0	-4.930452	-5.226027	-2.254273
14	6	0	-4.694044	1.678786	1.705175
15	6	0	-4.996772	2.864838	2.501373
16	6	0	-6.296070	2.749346	2.872230
17	6	0	-6.772605	1.493889	2.298671
18	7	0	-5.784532	0.867402	1.598585
19	1	0	-4.299358	3.660117	2.731604
20	1	0	-6.888264	3.430049	3.470410
21	6	0	-8.753454	-2.128438	0.849078
22	6	0	-10.033001	-1.860149	1.440224
23	6	0	-9.948719	-0.665822	2.110023
24	6	0	-8.614571	-0.162038	1.952035
25	1	0	-10.893264	-2.509373	1.352522
26	1	0	-10.727785	-0.164653	2.667789
27	6	0	-3.739382	-2.815123	-1.246207
28	1	0	-3.062381	-3.427428	-1.833927
29	6	0	-8.379978	-3.228592	0.079399
30	1	0	-9.153128	-3.970979	-0.093178
31	6	0	-3.438752	1.432712	1.136633
32	1	0	-2.665608	2.175114	1.309183
33	6	0	-8.079327	1.019177	2.462299
34	1	0	-8.756314	1.631486	3.050028
35	7	0	-3.880728	-0.718014	0.029534
36	1	0	-4.852117	-0.806129	0.308157
37	7	0	-7.937966	-1.077903	1.186538
38	1	0	-6.966564	-0.989804	0.907956

BPH$^+$

SCF Done: E(UB3LYP) = -989.981920174 A.U. after 16 cycles

Center Number	Atomic Number	Atomic Type	Coordinates (Angstroms) X	Y	Z
1	6	0	-3.179456	-1.609173	-0.793991
2	6	0	-1.892990	-1.037684	-1.060098
3	6	0	-1.828042	0.170700	-0.414887
4	6	0	-3.071733	0.384974	0.269186
5	1	0	-1.130686	-1.498843	-1.672111
6	1	0	-1.004722	0.871271	-0.410840
7	6	0	-7.075085	-3.502206	-0.376783
8	6	0	-6.756951	-4.713323	-1.128747
9	6	0	-5.460840	-4.598814	-1.499669
10	6	0	-4.996690	-3.318452	-0.971871
11	7	0	-5.988011	-2.676708	-0.280505
12	1	0	-7.449357	-5.517470	-1.338684
13	1	0	-4.862248	-5.288943	-2.078947
14	6	0	-4.623061	1.736504	1.701080
15	6	0	-4.895891	2.721000	2.696312
16	6	0	-6.213026	2.604314	3.073907
17	6	0	-6.804208	1.543284	2.326310
18	1	0	-4.158059	3.400397	3.099941
19	1	0	-6.726992	3.172967	3.836395
20	6	0	-8.776791	-2.105129	0.809858
21	6	0	-10.083731	-1.764060	1.287340
22	6	0	-9.995506	-0.553667	1.926076
23	6	0	-8.632496	-0.107787	1.862762
24	1	0	-10.966799	-2.371406	1.147013
25	1	0	-10.794905	0.002493	2.395446
26	6	0	-3.706000	-2.828289	-1.213080
27	1	0	-3.048264	-3.453821	-1.807534
28	6	0	-8.359229	-3.240387	0.119878
29	1	0	-9.119075	-3.991698	-0.068369
30	6	0	-3.408274	1.477185	1.070648
31	1	0	-2.615253	2.194576	1.251522
32	6	0	-8.107647	1.060603	2.417763
33	1	0	-8.791289	1.646696	3.022196
34	7	0	-3.860025	-0.710779	-0.006432
35	1	0	-4.738455	-0.986160	0.414214
36	7	0	-7.940959	-1.071920	1.162352
37	1	0	-6.941559	-1.180788	1.045167
38	7	0	-5.802704	1.018625	1.511064
39	1	0	-6.028022	0.626573	0.605555

BPH_2^{2+}

SCF Done: E(UB3LYP) = -990.247233850 A.U. after 14 cycles

Center Number	Atomic Number	Atomic Type	Coordinates (Angstroms) X	Y	Z
1	6	0	-3.226941	-1.507210	-0.928462
2	6	0	-1.860275	-1.122882	-0.843823
3	6	0	-1.783102	0.071401	-0.158935
4	6	0	-3.099208	0.468793	0.205050
5	1	0	-1.032287	-1.716343	-1.208179
6	1	0	-0.882574	0.601588	0.121240
7	6	0	-7.095043	-3.583768	-0.473385
8	6	0	-6.755055	-4.702078	-1.307762
9	6	0	-5.483200	-4.510898	-1.783484
10	6	0	-4.993141	-3.263963	-1.266498
11	1	0	-7.409611	-5.540130	-1.50421
12	1	0	-4.922882	-5.164110	-2.438266
13	6	0	-4.665213	1.808786	1.643942
14	6	0	-5.004083	2.925899	2.480418
15	6	0	-6.275916	2.734904	2.956267
16	6	0	-6.767083	1.489272	2.437255
17	1	0	-4.348626	3.762877	2.678439
18	1	0	-6.835318	3.387205	3.612736
19	6	0	-8.661235	-2.242959	0.964426
20	6	0	-9.977257	-1.845973	1.329154
21	6	0	-9.900074	-0.651701	2.014047
22	6	0	-8.533484	-0.266943	2.097956
23	1	0	-10.877755	-2.376542	1.049607
24	1	0	-10.728019	-0.058585	2.379060
25	6	0	-3.728930	-2.698694	-1.455476
26	1	0	-3.025981	-3.297225	-2.025865
27	6	0	-8.307288	-3.341362	0.178645
28	1	0	-9.095191	-4.063948	-0.007924
29	6	0	-3.453123	1.566742	0.991465
30	1	0	-2.665096	2.289032	1.178663
31	6	0	-8.031451	0.924211	2.625705
32	1	0	-8.734286	1.522327	3.196668
33	7	0	-3.986828	-0.519255	-0.268757
34	1	0	-4.819672	-0.188910	-0.750741
35	7	0	-7.773688	-1.254515	1.437561
36	1	0	-6.939915	-1.584271	1.918376
37	7	0	-5.759656	0.971442	1.652342
38	1	0	-5.816042	0.102613	1.153752
39	7	0	-6.000977	-2.745929	-0.482244
40	1	0	-5.947508	-1.874171	0.011534

References

[1] Elschner, A.; Kirchmeyer, S.; Lövenich, W.; Merker, U.; Reuter, K.; *PEDOT: Principles and Applications of an Intrinsically Conductive Polymer*; CRC Press: New York, 2012.

[2] Nardes, A. M.; Kemerink, M.; De Kok, M. M.; Vinken, E. Conductivity, *Org. Electron.* **2008**, *9*, 727–734.

[3] (a) Steim, R.; Kogler, F. R.; Brabec, C. J. *J. Mater. Chem.* **2010**, *20*, 2499–2512. (b) Ratcliff, E. L.; Zacher, B.; Armstrong, N. R. *Phys. Chem. Lett.* **2011**, *2*, 1337–1350. (c) Yip, H.-L.; Jen, A. K.-Y. *Energy Environ. Sci.* **2012**, *5*, 5994–6001. (d) Mishra, A.; Bäuerle, P. *Angew. Chem. Int. Ed.* **2012**, *51*, 2020–2067.

[4] (a) De Jong, M. P.; Van Ijzendoorn, L. J.; De Voigt, M. S *Appl. Phys. Lett.* **2000**, *77*, 2255–2257. (b) Turak, A. *RSC Adv.* **2013**, *3*, 6188–6225.

[5] Graetzel, M.; Janssen, R. A.; Mitzi, D. B.; Sargent, E. H. *Nature* **2012**, *488*, 304–312.

[6] Yabu, H.; Kanahara, M.; Shimomura, M.; Arita, T.; Harano, K. Nakamura, E.; Higuchi, T.; Jinnai, H. *ACS Appl. Mater. Interfaces* **2013**, *5*, 3262–3266. (b) Harano, K.; Minami, K.; Noiri, E.; Okamoto, K.; Nakamura, E. *Chem. Commun.* **2013**, *49*, 3525–3527. (c) Kanahara, M.; Satoh, H.; Higuchi, T.; Takahara, A.; Jinnai, H.; Harano, K.; Okada, S.; Nakamura, E.; Matsuo, Y.; Yabu, H. *Part. Part. Syst. Charact.* **2015**, *32*, 441–447.

[7] (a) Matsuo, Y.; Sato, Y.; Niinomi, T.; Soga, I.; Tanaka, H.; Nakamura, E. *J. Am. Chem. Soc.* **2009**, *131*, 16048–16050. (b) Service, R. F. *Science* **2011**, *332*, 293. (c) Tanaka, H.; Abe, Y.; Matsuo, Y.; Kawai, J.; Soga, I.; Sato, Y.; Nakamura, E. *Adv. Mater.* **2012**, *24*, 3521–3525.

[8] For inorganic materials, difference in secondary electron yield changes the contrast dramatically. (a) Frank, L.; Hovorka, M.; Mikmeková, Š.; Mikmeková, E.; Müllerová, I.; Pokorná, Z. *Mater.* **2012**, *5*, 2731–2756. (b) Asahina, S.; Togashi, T.; Terasaki, O.; Takami, S.; Adschiri, T.; Shibata, M.; Erdman, N. *Microsc. Anal.* **2012**, S12–S14. (c) Nagoshi, M.; Aoyama, T.; Sato, K. *Ultramicroscopy* **2013**, *124*, 20–25. (d) Roussel, L. Y.; Stokes, D. J.; Gestmann, I.; Darus, M.; Young, R. J. *Proc. SPIE* **2009**, 73780W.

[9] Electron Inelastic Mean Free Paths in *CRC Handbook of Chemistry and Physics*, 95th Edition; Haynes, W. H. Ed.; CRC Press: Boca Raton, FL, 2014, pp 12-120–12-121.

[10] (a) Joy, D. C. *Scanning* **1995**, *17*, 270–275. (b) Lin, Y.; Joy, D. C. *Surf. Interface Anal.* **2005**, *37*, 895–900.

[11] (a) Page, A. J.; Sear, R. P. *J. Am. Chem. Soc.* **2009**, *131*, 17550–17551. (b) Diao, Y.; Harada, T.; Myerson, A. S.; Hatton, T. A.; Trout, B. L. *Nat. Mater.* **2011**, *10*, 867–871. (c) Tan, L.; Davis, R.;

Myerson, A. S.; Trout, B. L. *Cryst. Growth Des.* **2015**, *15*, 2176–2186.

[12] Okada, S. Nanocolumnar Crystal Growth of Organic Semiconductor Molecules on a Graphene-Modified Surface in *Heterogeneous Nucleation of Organic Molecules on Chemically Modified Surfaces. M.S. Thesis* The University of Tokyo, Tokyo, March 2013.

[13] Bolotin, K. I.; Sikes, K. J.; Jiang, Z.; Klima, M.; Fudenberg, G.; Hone, J.; Kim, P.; Stormer, H. L. *Solid State Commun.* **2008**, *146*, 351–355.

[14] (a) Liu, Z.; Robinson, J. T.; Sun, X.; Dai, H. *J. Am. Chem. Soc.* **2008**, *130*, 10876–10877. (b) Shih, C.-J.; Paulus, G. L. C.; Wang, Q. H.; Jin, Z.; Blankschtein, D.; Strano, M. S. *Langmuir* **2012**, *28*, 8579–8586. (c) Georgakilas, V.; Otyepka, M.; Bourlinos, A. B.; Chandra, V.; Kim, N.; Kemp, K. C.; Hobza, P.; Zboril, R.; Kim, K. S. *Chem. Rev.* **2012**, *112*, 6156–6214. (d) Quintana, M.; Vazquez, E.; Prato, M. *Acc. Chem. Res.* **2013**, *46*, 138–148.

[15] (a) Fan, X.; Peng, W.; Li, Y.; Li, X.; Wang, S.; Zhang, G.; Zhang, F. *Adv. Mater.* **2008**, *20*, 4490–4493. (b) Dreyer, D. R.; Park, S.; Bielawski, C. W.; Ruoff, R. S. *Chem. Soc. Rev.* **2009**, *39*, 228–240. (c) Eda, G.; Chhowalla, M. *Adv. Mater.* **2010**, *22*, 2392–2415.

[16] Hummers, W. S., Jr; Offeman, R. E. *J. Am. Chem. Soc.* **1958**, *80*, 1339–1339.

[17] Friedel, B.; Keivanidis, P. E.; Brenner, T. J. K.; Abrusci, A.; McNeill, C. R.; Friend, R. H.; Greenham, N. C. *Macromolecules* **2009**, *42*, 6741–6747.

[18] Aramaki, S.; Sakai, Y.; Ono, N. *Appl. Phys. Lett.* **2004**, *84*, 2085–2087.

[19] Hibbert, F.; Hunte, K. *J. Chem. Soc., Perkin Trans. 2* **1977**, 1624–1628.

[20] Guthrie, J. P. *Can. J. Chem.* **1978**, *56*, 2342–2354.

[21] (a) Xie, R.; Karim, A.; Douglas, J. F.; Han, C. C.; Weiss, R. A. *Phys. Rev. Lett.* **1998**, *81*, 1251–1254. (b) Reiter, G. *Adv. Polym. Sci.* **2013**, *252*, 29–64.

[22] (a) Ogomi, Y.; Morita, A.; Tsukamoto, S.; Saitho, T. A *J. Phys. Chem. C* **2014**, *118*, 16551–16559. (b) Li, X.; Dar, M. I.; Yi, C.; Luo, J.; Tschumi, M.; Zakeeruddin, S. M.; Nazeeruddin, M. K.; Han, H.; Grätzel, M. *Nat. Chem.* **2015**, *7*, 703–711. (c) Bi, C.; Wang, Q.; Shao, Y.; Yuan, Y.; Xiao, Z.; Huang, J. *Nat. Commun.* **2015**, *6*, 7747.

[23] Koppel, D. E. *J. Chem. Phys.* **1972**, *57*, 4814–4820.

[24] Gaussian 09, Revision **D.01**, Frisch, M. J.; Trucks, G. W.; Schlegel, H. B.; Scuseria, G. E.; Robb, M. A.; Cheeseman, J. R.; Scalmani, G.; Barone, V.; Mennucci, B.; Petersson, G. A.; Nakatsuji, H.; Caricato, M.; Li, X.; Hratchian, H. P.; Izmaylov, A. F.; Bloino, J.; Zheng, G.; Sonnenberg, J. L.; Hada, M.; Ehara, M.; Toyota, K.; Fukuda, R.; Hasegawa, J.; Ishida, M.; Nakajima, T.; Honda, Y.; Kitao, O.; Nakai, H.; Vreven, T.; Montgomery, J. A.; Jr., Peralta, J. E.; Ogliaro, F.; Bearpark,

M.; Heyd, J. J.; Brothers, E.; Kudin, K. N.; Staroverov, V. N.; Kobayashi, R.; Normand, J.; Raghavachari, K.; Rendell, A.; Burant, J. C.; Iyengar, S. S.; Tomasi, J.; Cossi, M.; Rega, N.; Millam, J. M.; Klene, M.; Knox, J. E.; Cross, J. B.; Bakken, V.; Adamo, C.; Jaramillo, J.; Gomperts, R.; Stratmann, R. E.; Yazyev, O.; Austin, A. J.; Cammi, R.; Pomelli, C.; Ochterski, J. W.; Martin, R. L.; Morokuma, K.; Zakrzewski, V. G.; Voth, G. A.; Salvador, P.; Dannenberg, J. J.; Dapprich, S.; Daniels, A. D.; Farkas, Ö.; Foresman, J. B.; Ortiz, J. V.; Cioslowski, J.; Fox, D. J. Gaussian, Inc., Wallingford CT, 2009.

[25] Hummers, W. S.; Offeman, J. R. E. *J. Am. Chem. Soc.* **1958**, *80*, 1339.

[26] Stankovich, S.; Piner, R. D.; Nguyen, S. B.; Ruoff, R. S. *Carbon* **2006**, *44*, 3342–3347.

[27] Friedel, B.; Keivanidis, P. E.; Brenner, T. J. K.; Abrusci, A.; McNeill, C. R.; Friend, R. H.; Greenham, N. C. Macromolecules **2009**, *42*, 6741–6747.

Chapter 5. Diffusion-Limited Crystal Growth of Tetrabenzoporphyrin on Polycrystalline Tetrabenzoporphyrin Layer

5-1 Introduction

In organic photovoltaics (OPVs), performance is dependent on the crystal morphology in active layer.[1] Large donor-acceptor interfacial area, i.e. large surface area of the donor crystals, is beneficial for efficient charge separation and high current density. Considering the diffusion length of excimers that are 10 to 20 nm in organic molecules, nanopillar structure with the domain size of 20 nm is highly desired.[2] This morphology has been achieved by fabricating a bulk heterojunction layer.[3] The bulk heterojunction layer is not limited to polymer systems, but in small molecule system is also applicable, as demonstrated in a system using a mixture of 21*H*,23*H*-tetrabenzo-[*b*,*g*,*l*,*q*]porphyrin (BP): fullerene derivatives casted onto a pre-formed flat polycrystalline BP film on Poly(3,4-ethylenedioxythiophene): poly(styrene sulfonate) (PEDOT:PSS).[4] However, the molecular-level mechanism of nanopillar generation remained unclear.

Previously, Oiki reported control over morphologies of BP in the bulk heterojunction layer.[5] He solution-processed BP on polycrystalline flat BP film by casting a solution mixture of 1,4:8,11:15,18:22,25-tetraethano-29*H*,31*H*-tetrabenzo[*b*.*g*.*l*.*q*]porphyrin (CP) as a precursor of BP and non-volatile molecules called matrix followed by heating at 180 °C (Figure 5-1). Due to the insolubility of BP in any neutral organic solvents, the matrix can be removed to expose BP layer for further study, and further deposition of fullerene derivatives by either solution process and vacuum deposition was possible to form donor/acceptor heterojunction. The crystal size of BP decreased from submicron to ca. 20 nm by increasing viscosity of the matrix (Figure 5-2). OPVs were fabricated by applying fullerene derivatives onto the exposed BP layer, and high current density and high performance was observed when the crystal size of BP was small. The process of crystal growth was qualitatively studied for *N*,*N*´-dicarbazolyl-3,5-benzene (MCP)[6] and [6,6]-Phenyl-C_{61}-butyric acid *n*-butyl ester (PCBNB) and concluded that crystal nucleation took place within the first one minute followed by crystal growth till four minute, and then crystal fusion was observed only in low-viscosity matrix. (Figure 5-3).

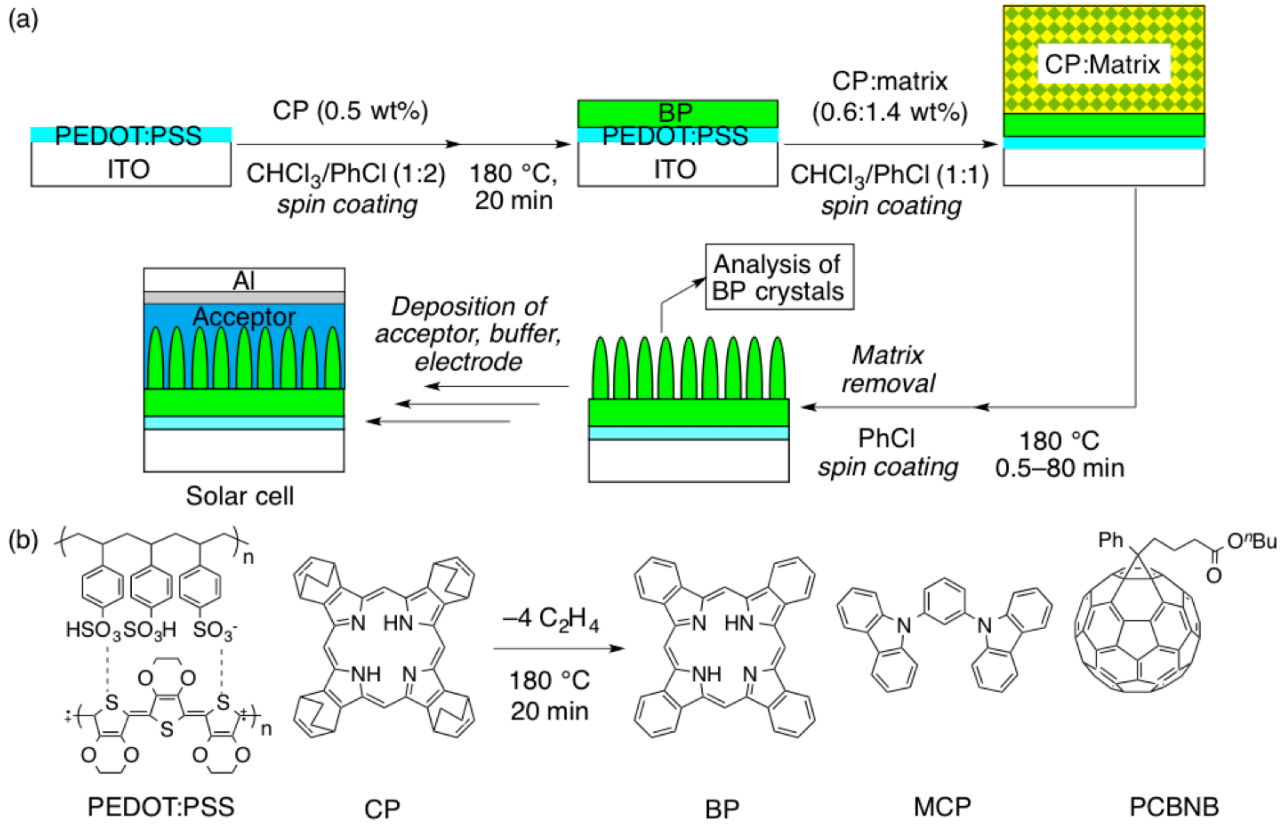

Figure 5-1. Fabrication of device structures. (a) A schematic illustration of the fabrication method of partial device structure with nanocrystalline BP on pre-formed polycrystalline BP for structural analysis and further fabrication toward OPVs. (b) Chemical structure of materials used.

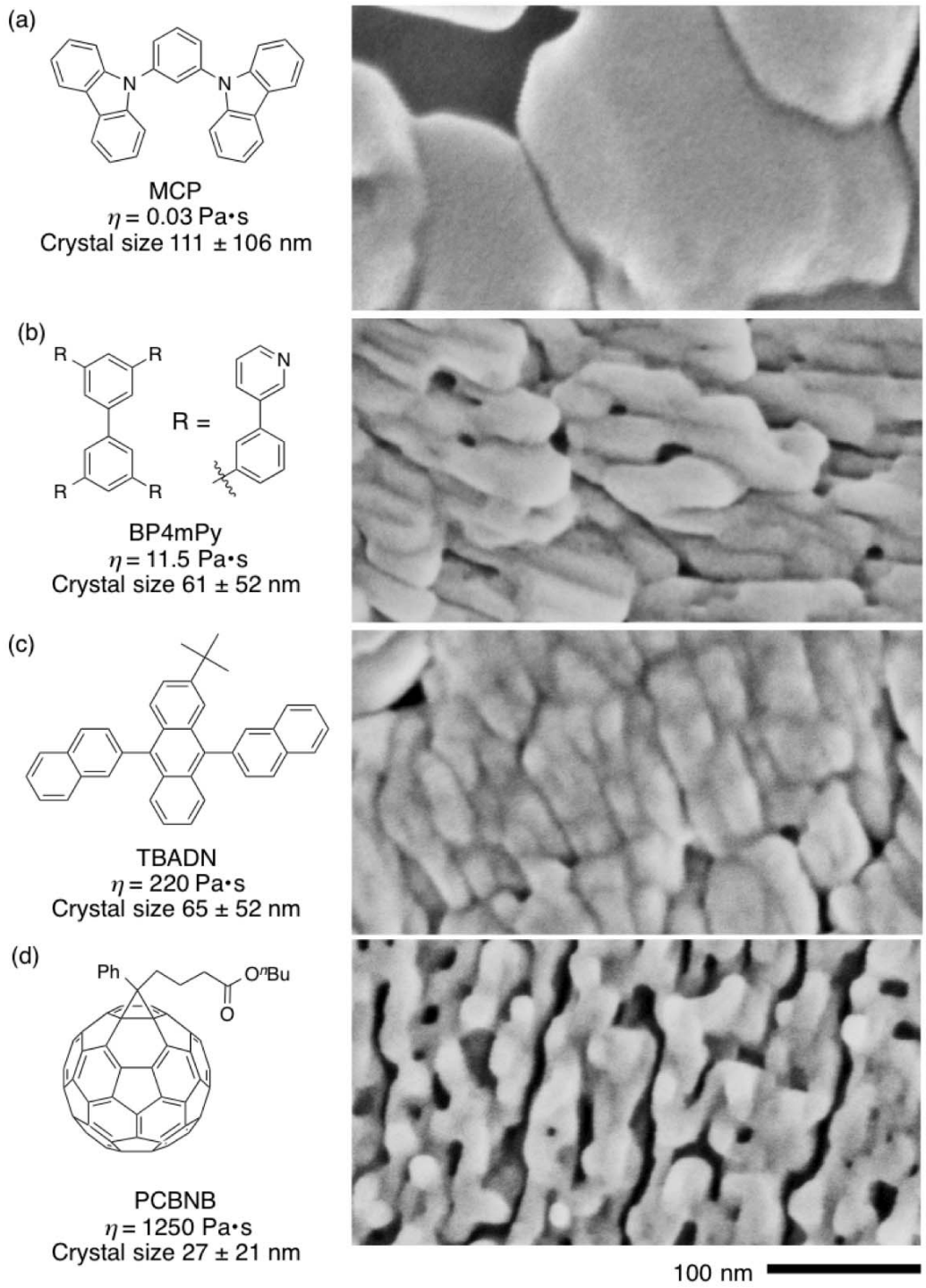

Figure 5-2. SEM images of crystal morphology of BP on polycrystalline flat BP after 20 min heating with matrices with different viscosity. (a) MCP, (b) 3,3',5,5'-tetra[3-(3-pyridyl)-phenyl] biphenyl (BP4mPy), (c) 3-*tert*-butyl-9,10-di(naphth-2-yl)anthracene (TBADN), and (d) PCBNB were used and their viscosities at 180 °C are shown under the chemical structures. SEM images were reproduced from ref. [5].

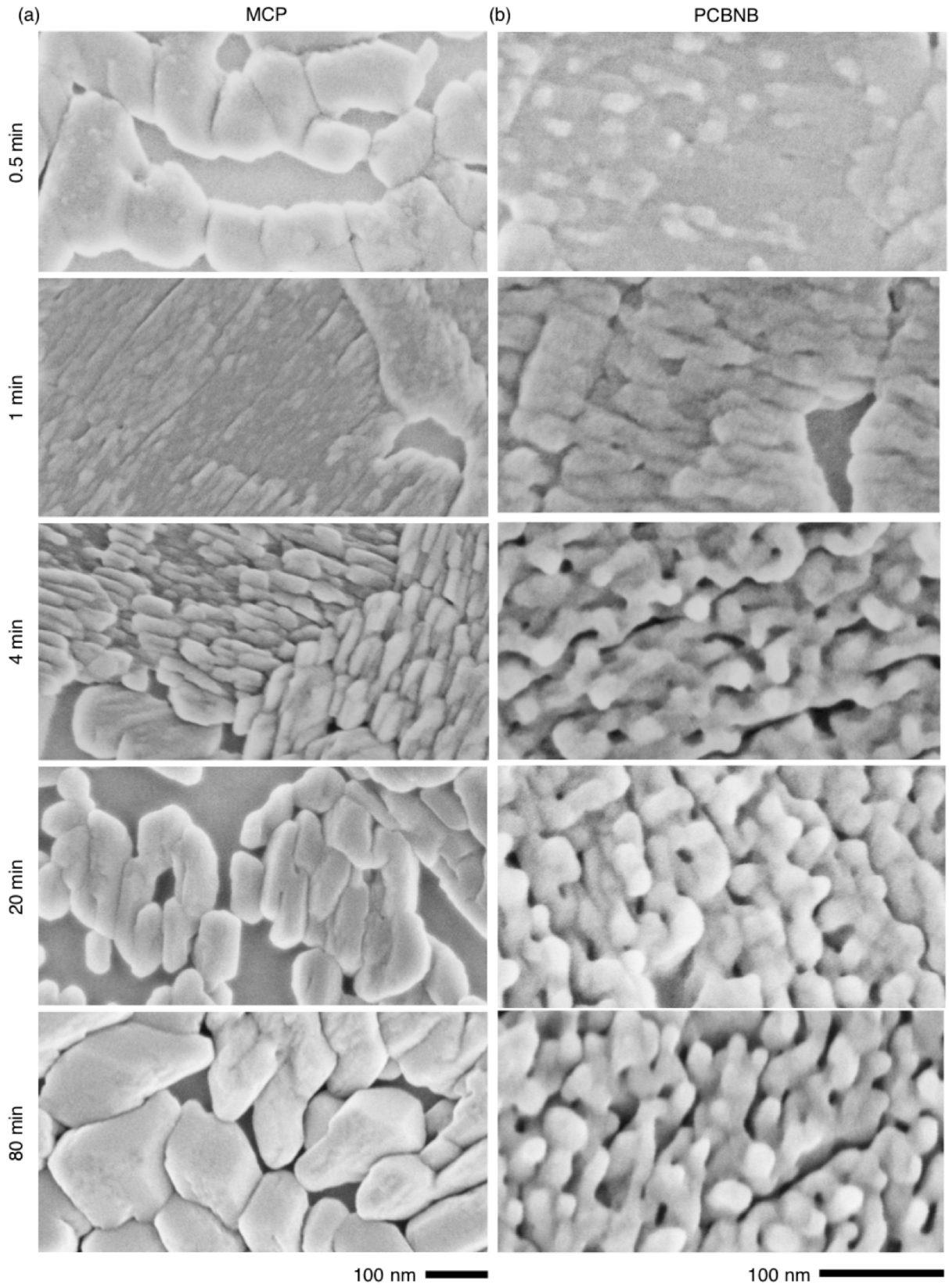

Figure 5-3. SEM images of time-dependent crystal growth of BP on polycrystalline flat BP. (a) MCP and (b) PCBNB were used as matrices. SEM images were reproduced from ref. [5].

Here, I quantitatively analyzed the time-dependent crystallization process of BP on polycrystalline flat BP film based on spectroscopies and numerical simulations using MCP and PCBNB as matrices. I have shown that the molecular diffusion determines the final crystal size in epitaxial nucleation system. Slow molecular diffusion in high-viscosity matrix limits crystal growth over crystal nucleation, and it also prevents further morphological change to increase crystal size.

5-2 Time-Dependence of BP Crystallization

The formation of BP film is composed of three steps; CP to BP conversion, nucleation and crystallization of BP, and morphological evolution (Figure 5-4). These three steps were spectroscopically and microscopically classified against heating time on samples using MCP and PCBNB as matrices.

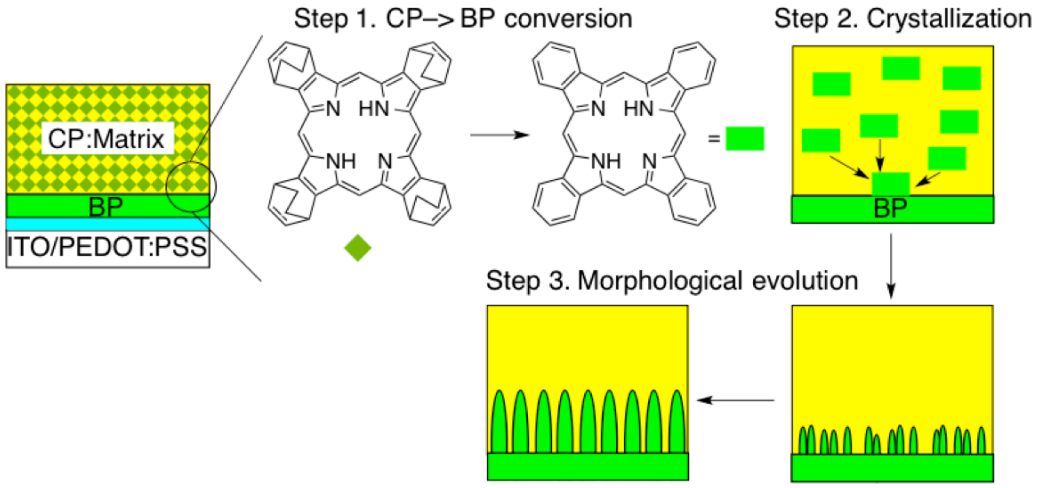

Figure 5-4. A schematic illustration of the process of crystal formation of BP.

UV/Vis spectrograms after washing out the matrices are shown in Figure 5-5. The shapes of the spectra are similar in both cases, indicating that BP did not change its polymorph by matrices. The overall light absorption in 350–800 nm saturated at 4 min, and this indicates that CP to BP conversion and crystallization of BP finished within 4 min, as previously mentioned.[5] Note that this result does not necessarily mean that CP remains before 4 min, since amorphous BP within matrices can be removed by washing.

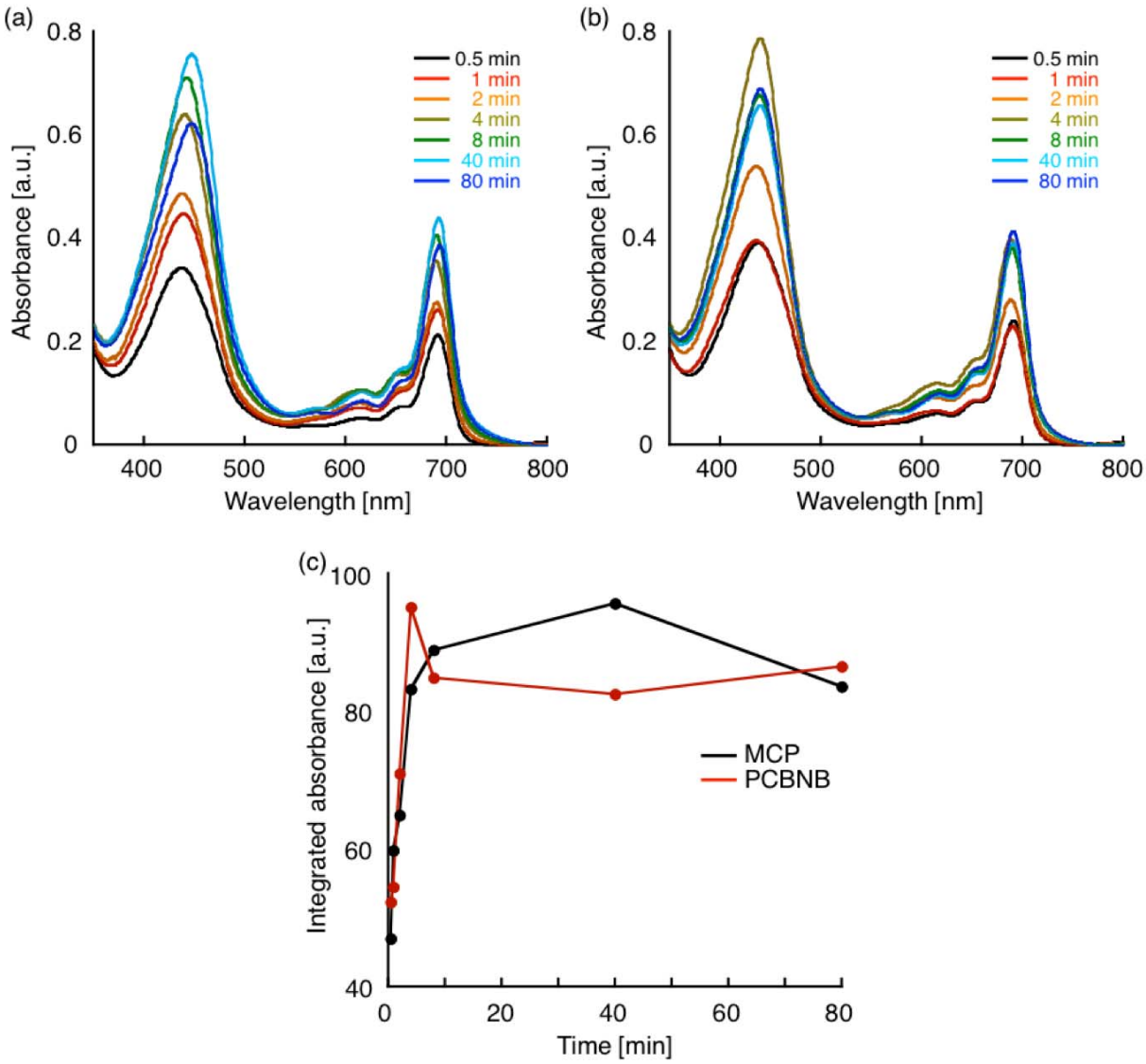

Figure 5-5. Time-dependent UV/Vis absorption spectra of ITO/PEDOT:PSS/BP/(BP:matrix) after removal of matrix. (a) MCP and (b) PCBNB were used as matrices. (c) Total absorption intensities against time. Black and red lines indicate MCP and PCBNB, respectively.

In-plane glazing incidence X-ray diffraction (GIXD) shows the crystallinity of BP (Figure 5-6). Crystal planes were assigned from single crystal structure.[7] Some diffraction originating from BP appears at 0.5 min, and this mainly comes from the underlying polycrystalline BP of ITO/PEDOT:PSS/*BP*/(BP:matrix) structure. The (101), (012), (202) and (13–1) signals appeared and signal intensities of (002), (004), (113) and (114) peaks significantly increased at 4 min, and this indicates that crystal growth started between 2 and 4 min. The increase in intensity stopped at 4 to 8 min, and change in the ratio of peak intensities is not significant, indicating that crystal orientation did not change during continuous heating process (Figure 5-6c, d). Crystal size calculated from the width of each peak was 13–22 nm (Figure 5-7), and less than that of

polycrystalline BP underlayer of 10 × 100 nm (Chapter 4). This indicates that the underlying polycrystalline BP crystals determine the crystal size of heterojunction layer. It also indicates that the μm-sized crystals observed in MCP system are polycrystalline, while 20-nm sized crystal domains in PCBNB system are composed of single crystals.

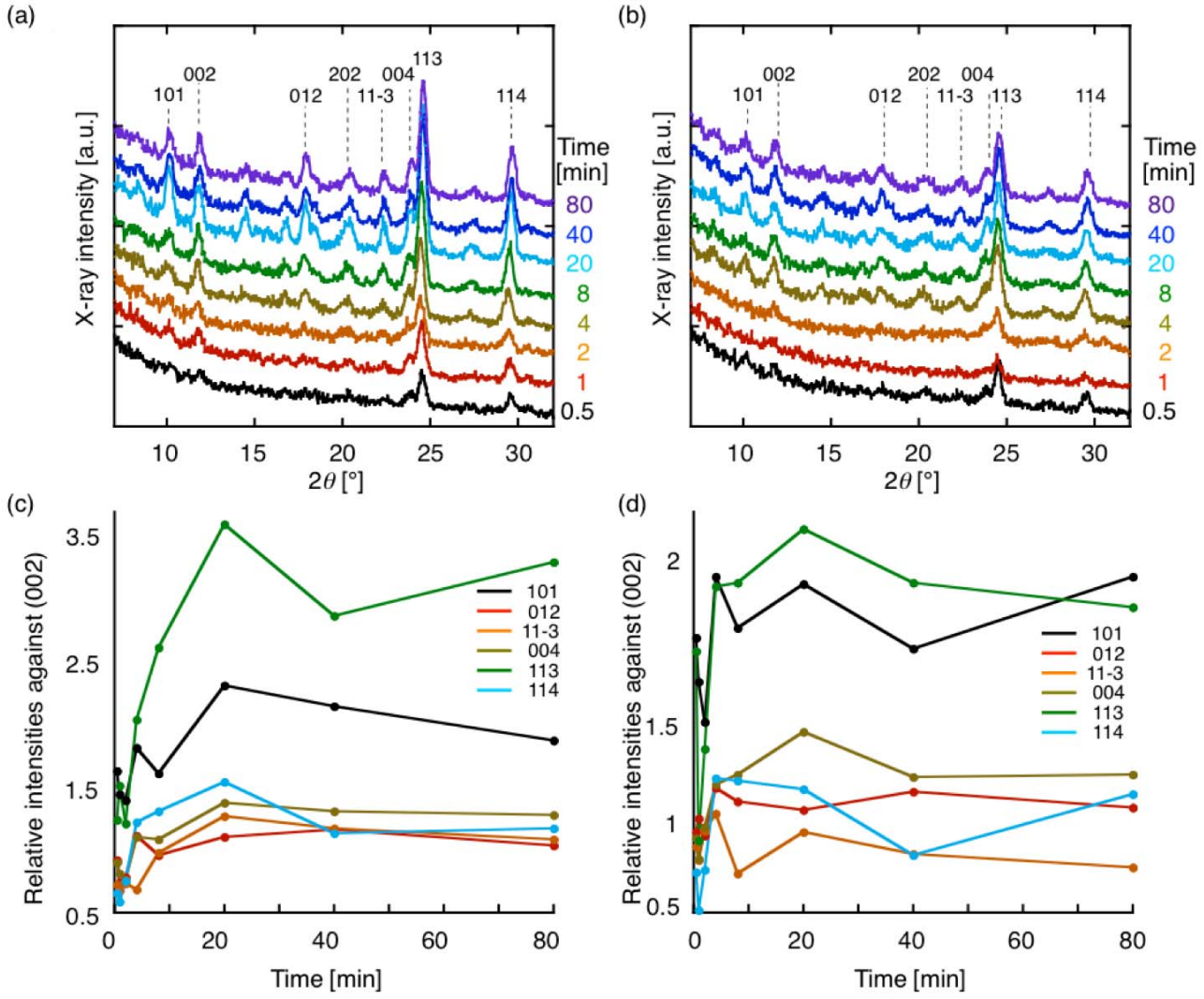

Figure 5-6. In-plane GIXD spectra of ITO/PEDOT:PSS/BP/(BP:matrix) after removal of matrix. (a) MCP and (b) PCBNB were used as matrices. (c, d) Relative intensities of diffraction peaks against (002). (c) MCP and (d) PCBNB were used as matrices.

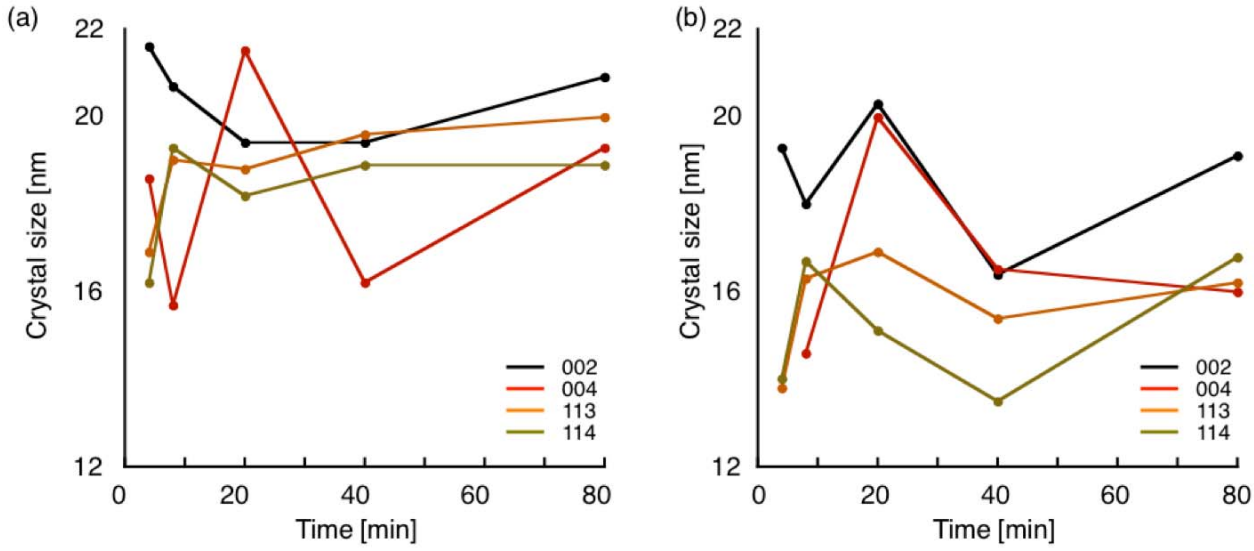

Figure 5-7. Crystal size of BP calculated from peak width of (002) (black), (004) (red), (113) (orange), (114) (amber) signals. (a) MCP and (b) PCBNB were used as matrices.

On the contrary to UV/Vis and GIXD where viscosity did not affect the spectra, SEM images show dynamic morphological evolution upon heating (Figure 5-3, Figure 5-8). When highly viscos PCBNB was used as a matrix, the number of crystals increases in the first 1 min and then drops at 2 min. After 2 min, the crystal density and the size of crystals did not change during 80-min heating with the averaged inter-crystalline distance of 48 ± 33 nm (average ± s.d.). This indicates that the crystal growth finished within 4 min and re-dissolution of crystals was negligible. On the other hand, in MCP, a low-viscosity matrix, the number of crystals decreased and the crystal size increased continuously till 20 min. In addition, SEM images of MCP system contained void spaces. This indicates the dissolution and rearrangement of BP around grain boundaries.[8]

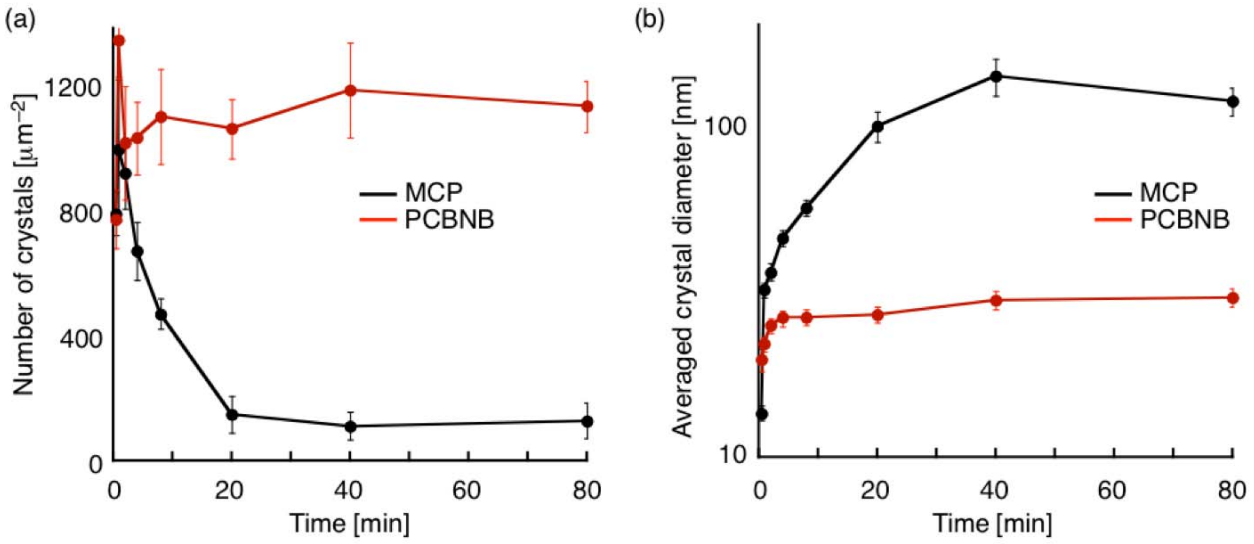

Figure 5-8. (a) The density of BP crystals and (b) averaged diameter of BP crystals based on SEM images. Black and red data indicate MCP and PCBNB, respectively.

5-3 Mechanism of Crystal Growth

The crystallization process of BP on polycrystalline BP is summarized in Figure 5-9. The precursor-matrix mixture is heated at 180 °C, and thus generated BP epitaxially nucleates on polycrystalline BP. The probability to form crystal nuclei does not depend on the matrix viscosity. The nucleation events are sporadic presumably due to surface adsorbates on polycrystalline BP. When the matrix viscosity is low, BP prefers to participate in crystal growth on crystal nuclei than forming another nuclei because crystal nucleation is energetically unfavored than crystal growth,[9] and crystal growth takes place. During crystallization, adjacent BP crystals can merge into larger crystals. At the late stage of heating, amorphous BP molecules on small BP crystals may dissolve in matrix and transferred to larger crystals to promote Ostwald ripening.[10] This ripening process is thermodynamically favored, and finally submicron crystals are obtained. On the other hand, when the matrix viscosity is high, crystal nucleation is kinetically favored over crystal growth near the polycrystalline BP since molecular diffusion in vertical direction (~10 nm) is more favored than that in lateral direction (~20 nm). Two closely adjacent BP crystals can merge upon crystal growth, but most of the crystals grow vertically because of the limited molecular diffusion. Finally nanopillar crystalline array is obtained.

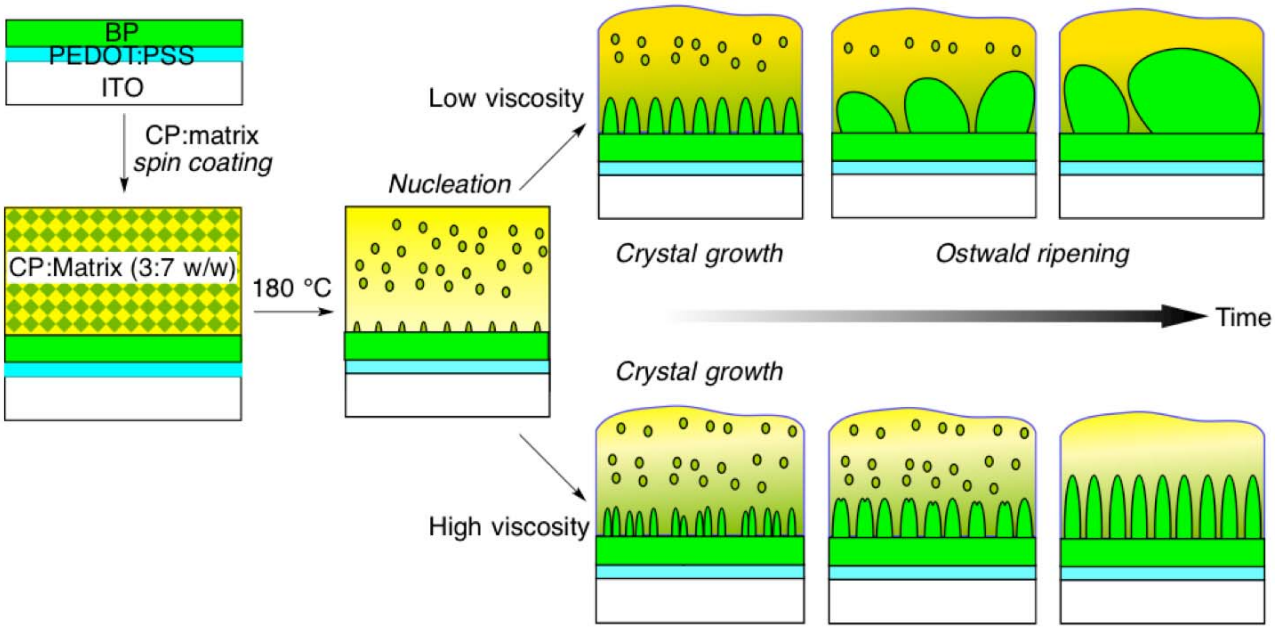

Figure 5-9. A schematic illustration of the crystal growth of BP in matrices with different viscosity.

5-4 Numerical Simulation

In order to quantitatively describe the dynamics of molecular diffusion of BP in matrices with different viscosity, numerical simulation based on diffusion equation was performed. Stokes-Einstein-Debye equation correlates molecular diffusion with viscosity as

$$D = \frac{k_B T}{6\pi\eta r_{\mathrm{H}}} \qquad \text{(eq.5-1)}$$

where D is the diffusion coefficient, k_{B} is the Boltzmann's constant, T is the temperature, h is the viscosity of the matrix, and r_{H} is the hydrodynamic radius. The hydrodynamic radius of BP r_{H} is derived from the equation

$$\frac{1}{r_{\mathrm{H}}} = \frac{1}{N^2}\sum_{i\neq j}\frac{1}{r_{ij}} \qquad \text{(eq.5-2)}$$

where N is the total number of atoms, and r_{ij} is the inter-atom distance between atoms i and j. r_{H} was calculated from the atomic coordinates in single crystal X-ray diffraction to be 5.00 Å. Viscosity of MCP and PCBNB are 0.03 and 1250 Pa s at 180 °C, and D is calculated as 2.21×10^{7} and 5.31×10^{2} nm^2 s^{-1}, respectively.

The time-dependent crystal growth was correlated to molecular diffusion based on numerical simulation of diffusion equation. The diffusion equation is expressed as

$$u(\vec{r},t) = D\nabla^2 u(\vec{r},t) \qquad \text{(eq.5-3)}$$

where $\vec{r}$ and *t* represents space and time, respectively, and $u(\vec{r},t)$ is the concentration of solute. This equation is expressed in the polar coordinates system using the distance from center *r* as

$$u(\vec{r},t) = D\frac{1}{r^2}\frac{\partial}{r}\left(r^2\frac{u(r,t)}{\partial r}\right) \qquad \text{(eq.5-4)}$$

When $r \neq 0$, eq. 5 can be simplified by variable transformation of

$$ru(r,t) \equiv w(r,t) \qquad \text{(eq.5-5)}$$

as

$$w(r,t) = D\frac{\partial^2 w(r,t)}{\partial r^2} \qquad \text{(eq.5-6)}$$

For numerical solution, eq. 5-6 is re-written in finite difference;

$$\frac{w(r,t+\Delta t)-w(r,t)}{\Delta t} = D\frac{w(r+\Delta r,t)-2w(r,t)+w(r-\Delta r,t)}{\Delta r^2} \qquad \text{(eq.5-7)}$$

and it gives the time-dependent diffusion of molecules (Figure 5-10a)

$$w(r,t+\Delta t) = w(r,t)+\frac{D\Delta t}{\Delta r^2}\left\{w(r+\Delta r,t)-2w(r,t)+w(r-\Delta r,t)\right\} \qquad \text{(eq.5-8)}$$

This numerical simulation is stable under

$$\frac{D\Delta t}{\Delta r^2} \le 0.5 \qquad \text{(eq.5-9)}$$

In order to express crystallization, nucleation site was put at r_0 = 0.1 nm at which point all the diffused molecules crystallize. Note that $r = 0$ is not defined in eq. 7. This treatment changes the equation at $r = r_0$, Δr as (Figure 5-10b);

$$\begin{cases} w(r_0,t+\Delta t) = w(r_0,t) + \dfrac{D\Delta t}{\Delta r^2}w(r_0+\Delta r,t) \\ w(r_0+\Delta r,t+\Delta t) = w(r_0+\Delta r,t)+\dfrac{D\Delta t}{\Delta r^2}\left\{w(r_0+2\Delta r,t)-2w(r_0+\Delta r,t)\right\} \end{cases} \qquad \text{(eq.5-10)}$$

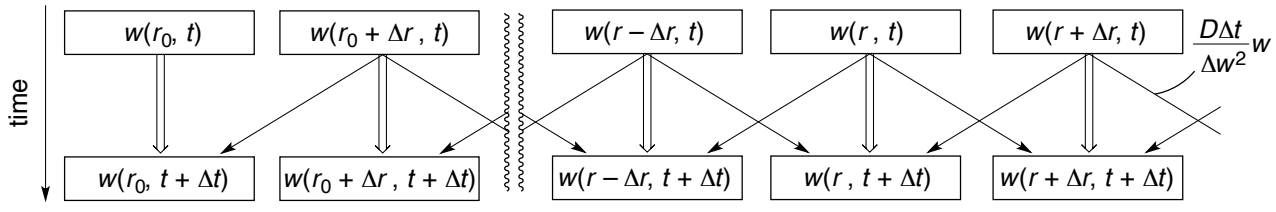

Figure 5-10. Schematic illustration of numerical simulation of diffusion equation in a spherical system.

The numerical simulation was performed for 50-nm sphere considering the typical inter-crystal distance of 48 ± 33 nm. Most of the solute molecules crystallized within 0.2 ms and 10 s in MCP

and PCBNB, respectively (Figure 5-11). In SEM images, the number of crystals increased till 1 min, indicating that crystal nucleation requires the time order of seconds. This supports the hypothesis that crystal nucleation is slower than crystal growth in MCP system. This rapid material transport in MCP can also explain the high propensity for Ostwald ripening within a short period, assuming that the surface energy of BP crystals is similar in MCP and PCBNB. This result also indicates that the limiting step in crystallization of BP is the CP-to-BP conversion that requires at least 0.5–1 min judging from the color change from purple to green, and reorganization of BP on crystal surface.

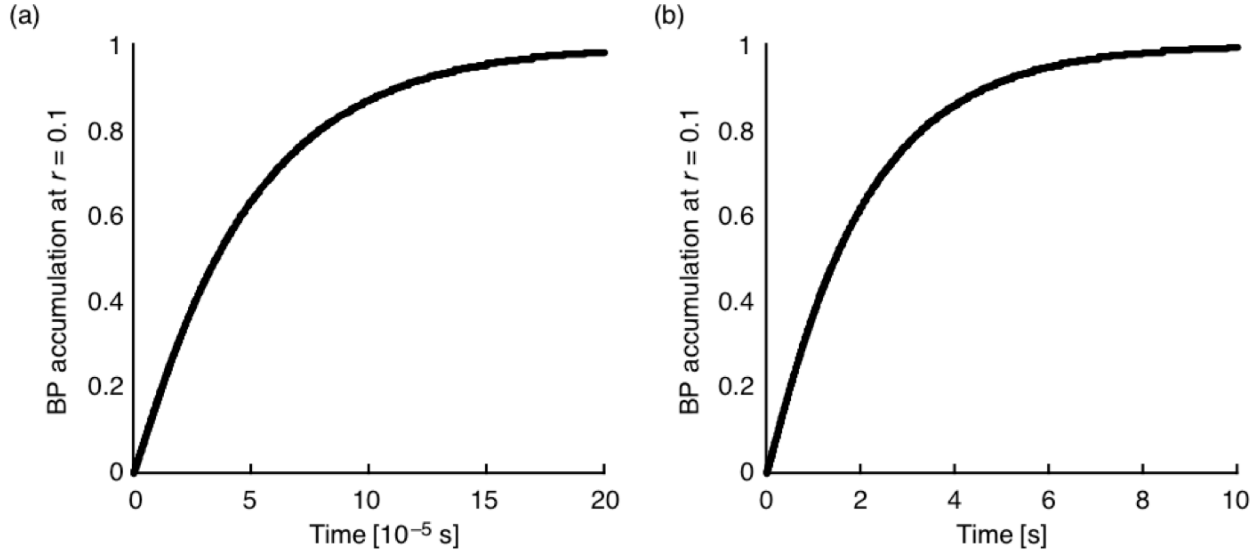

Figure 5-11. Numerical solution of diffusion equation in polar coordinate system. Parameters were (a) D = 2.21 × 10^7 nm^2 s^{-1}, Δr = 2.5 nm, and Δt = 0.1 μs that simulates MCP matrix, and (b) D = 5.31 × 10^2 nm^2 s^{-1}, Δr = 2.5 nm, and Δt = 5 ms that simulates MCP matrix.

The obtained conclusion further implies the stability of devices against morphological change. If the viscosity of the matrices at 50 °C was estimated from the extrapolation of Arrhenius plot at 170, 180, and 190 °C (Table 5-1),[11]

$$\eta = AT\exp\left(-\frac{E_a}{RT}\right) \qquad \text{(eq.5-11)}$$

where A is the pre-exponential factor, E_a is the apparent activation energy for diffusion, and R is the gas constant. The 4.4 × 10^3 increase in diffusion constant of MCP upon cooling indicates the time scale of molecular diffusion in the order of seconds considering the inverse relation between diffusion time scale and diffusion coefficient ($D\Delta t = const.$). Similarly, the nanopillar structure in PCBNB matrix would be stable for several centuries (10^9 sec) with the diffusion time scale of seconds. This result implies that the material pairs with the viscosity of more than 10^{10} Pa•s at operating temperature would be structurally stable for several tens of years.

Table 5-1. Temperature-dependent viscosity of MCP and PCBNB, and extrapolated viscosity at 50 °C. Units are Pa•s.

	190 °C	180 °C	170 °C	50 °C
MCP	0.02	0.03	0.05	131
PCBNB	550	1250	7800	5.71×10^{13}

5-5 Conclusion

In summary, I have shown that the crystal growth of BP on polycrystalline BP is a diffusion-controlled process. The phase separation and crystallization of BP:matrix heterojunction involves three steps; CP to BP conversion, BP crystal growth, and ripening. CP to BP conversion and BP crystal growth finished within 4 min regardless of the matrix viscosity, while the morphologies at 4 min and the Ostwald ripening process were viscosity-dependent. Numerical simulation of BP diffusion provided the time scale of crystallization, to support the control over growth of BP. Donor and acceptor molecular pairs with high viscosity would contribute to high stability, and the BP:fullerene systems would be more stable than polymer-based systems with alkyl chains.

5-6 Experimental Section

General.

Sample preparation and top-view SEM imaging were previously conducted by M. Oiki at the landing voltage of 1 kV. UV/Vis/NIR spectra were recorded on JASCO V-670 equipped with film holder and a ϕ 2-mm pin hall and are reported as wavenumber (n) in cm^{-1}. GIXD was performed on Rigaku SmartLab X-ray diffractometer using CuK_{α} (radiation wavelength, 1.5418 Å). Structural optimization and energy calculation were performed on Gaussian 09 at B3LYP/6-31G(d,p) level of theory (see Chapter 4). The size distribution was calculated by masking the image in Adobe Photoshop and analyzed using ImageJ software. Inter-crystalline distance was calculated from a Voronoi diagram processed on ImageJ software. The numerical simulation was performed on Microsoft Excel.

References

[1] Graetzel, M.; Janssen, R. A.; Mitzi, D. B.; Sargent, E. H. *Nature* **2012**, *488*, 304–312.

[2] (a) Scully, S. R.; McGehee, M. D. *J. Appl. Phys.* **2006**, *100*, 034907. (b) Kozub, D. R.; Vakhshouri, K.; Kesava, S. V.; Wang, C.; Hexemer, A.; Gomez, E. D. *Chem. Commun.* **2012**, *48*, 5859–5861.

[3] (a) Brabec, C. J.; Gowrisanker, S.; Halls, J. J. M.; Laird, D.; Jia, S.; Williams, S. P. *Adv. Mater.* **2010**, *22*, 3839–3856. (b) Beaujuge, P. M.; Fréchet, J. M. J. *J. Am. Chem. Soc.* **2011**, *133*, 20009–20029. (c) Karagiannidis, P. G.; Georgiou, D.; Pitsalidis, C.; Laskarakis, A.; Logothetidis, S. *Mater. Chem. Phys.* **2011**, *129*, 1207–1213.

[4] (a) Matsuo, Y.; Sato, Y.; Niinomi, T.; Soga, I.; Tanaka, H.; Nakamura, E. *J. Am. Chem. Soc.* **2009**, *131*, 16048–16050. (b) Ku, S.-Y.; Liman, C. D.; Cochran, J. E.; Toney, M. F.; Chabinyc, M. L.; Hawker, C. J. *Adv. Mater.* **2011**, *23*, 2289–2293. (c) Tanaka, H.; Abe, Y.; Matsuo, Y.; Kawai, J.; Soga, I.; Sato, Y.; Nakamura, E. *Adv. Mater.* **2012**, *24*, 3521–3525.

[5] Oiki, M. Efficient Carrier Generation in Organic Photovoltaics by Controlling Phase-separated Morphology and Electronic Energy Level. *M.S. Thesis* The University of Tokyo, Tokyo, March 2014.

[6] (a) Qiao, J.; Wang, L. D.; Qiu, Y. *SPIE*, **2006**, *6192*, 61920T. (b) Adamovich, V.; Brooks, J.; Tamayo, A.; Alexander, A. M.; Djurovich, P. I.; D'Andrade, B. W.; Adachi, C.; Forrest, S. R.; Thompson, M. E. *New J. Chem.* **2002**, *26*, 1171–1178.

[7] Aramaki, S.; Mizuguchi, J. *Acta Cryst. E* **2003**, *59*, o1556.

[8] (a) Voorhees, P. W. *J. Stat. Phys.* **1985**, *38*, 231–252. (b) Wang, Y.; He, J.; Liu, C.; Chong, W. H.; Chen, H. *Angew. Chem. Int. Ed.* **2014**, *54*, 2022–2051.

[9] Gibbs, J. W.; *Am. J. Sci.* **1878**, *16*, 441–458.

[10] (a) Cabane, H.; Laporte, D.; Provost, A. *Contrib. Min. Petrol.* **2001**, *142*, 361–373. (b) Lindqvist, C.; Sanz-Velasco, A.; Wang, E.; Bäcke, O.; Gustafsson, S.; Olsson, E.; Andersson, M. R.; Müller, C. *J. Mater. Chem. A* **2013**, *1*, 7174–7180.

[11] Ewell, R. H. *J. Appl. Phys.* **1938**, *9*, 252–269.

Chapter 6. Summary and Outlook

In the present thesis, I developed quantitative methods to investigate the dynamics of organic molecules. I have developed theoretical methods to the qualitative data sets of the previously published electron microscopic images or newly acquired images to investigate the problems in microscopic analyses; imaging principles of single molecules in TEM, the electron-specimen interaction on the chemical reaction of organic molecules, crystal nucleation and crystal growth of organic semiconductor molecules. I also addressed the statistical and theoretical expression of the observed microscopic events

In Chapter 2, the origin of apparent motions in TEM movies was discussed. The principles of TEM imaging and the motion of molecules from quantum mechanical perspective were revisited in order to understand the motion, or the time-dependent change in contrast. Quantum mechanics simulation showed that the apparent motion is dependent on the electron dose rate; images become sharper and less mobile at higher electron dose, and vice versa. The rotational energy barrier and the rotational inertia of the molecule govern the motion of the rotor. Based on this assumption, I synthesized bromine-substituted Y-shaped biphenyl rotor attached on a carbon nanohorn via an amide bond and observed their motions at various electron dose rate to find out the decrease in the apparent motion and the increase in the contrast at high electron dose rate (Figure 6-1). Further investigation of the motion was performed using iodine-substituted Y-shaped biphenyl rotor that possesses 1.5-times higher rotational inertia than that of bromine-substituted one, and less apparent motion was observed than that of bromine-substituted ones. These findings assure that the TEM images of single organic molecules are snapshots of molecules under quantum mechanical motion.

This result is fundamental to discuss the image quality in terms of the atom resolution. Unlike inorganic solids where atoms are hierarchically assembled with some thickness to show diffraction, single organic molecules inevitably undergo bond vibration including bond rotation. This implies that the SMART-TEM images of any flexible molecules inevitably suffer from blurring originating from the vibrational motions. One way to prevent the apparent motion and to observe molecules in sub-atomic resolution would be to overlap several images in similar shape.

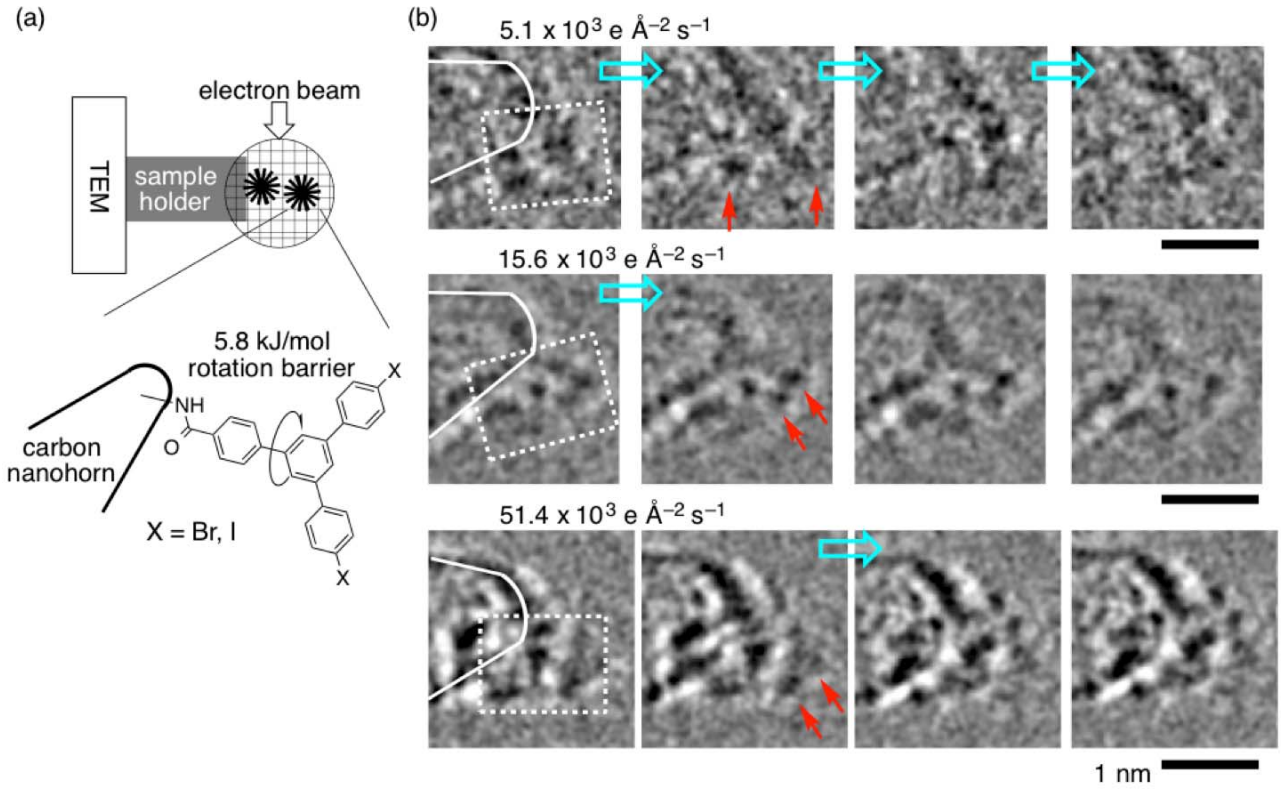

Figure 6-1. Apparent motion of Y-shaped biphenyl rotor. (a) A schematic illustration of the TEM imaging. (b) TEM images of a bromine-substituted rotor at the electron dose rate of 5.1–51.4 × 10^3 electrons nm^{-2} $Å^{=2}$ taken at 120 kV, 293 K. Scale bars: 1 nm.

In Chapter 3, the reaction dynamics of fullerene dimerization followed by rearrangement based on the published SMART-TEM images at various temperatures were described.[1] This was the first example where the chemical reactions under TEM imaging were quantitatively analyzed, and the analysis is based on a theory of unimolecular reactions that incorporate quantum states. The dimerization is essentially a bimolecular reaction, but the kinetics followed first-order kinetics because of the dense packing of fullerene inside CNT. The obtained energy barrier and the fitting curve showed the existence of two reaction pathways; a temperature-sensitive reaction path from triplet excited state, and a temperature-insensitive reaction path from highly excited state before thermal relaxation of energy (Figure 6-2). It is noteworthy that the reaction path where electronic excited state is involved underwent in the similar manner to the photochemical reactions, and the thermal relaxation is usually inevitable for conventional reaction systems where intermolecular collision often take place. The obtained result further implies the possibility to study the chemistry at electronic excited state.

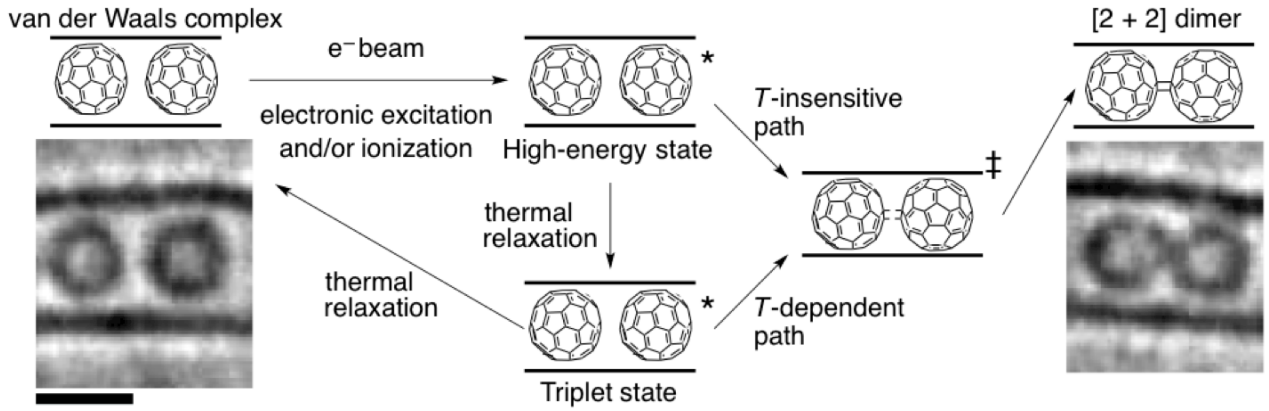

Figure 6-2. Schematic images and TEM images of fullerene dimerization inside CNT. Scale bar: 1 nm. TEM images were reproduced from ref. 1with permission from Nature Publishing Group.

In Chapter 4, the mechanisms of crystal nucleation of donor molecules on poly(3,4-ethoxythiophene): poly(4-styrenesulfonate) (PEDOT:PSS), a *de facto* standard buffer material for solar cells, are described. In this work, tetrabenzoporphyrin (BP) was initially investigated due to its insolubility in any organic solvents that help cleaning the surface for scanning electron microscopy (SEM) observation. The low-landing voltage imaging was utilized for organic crystals, and it enabled coating-free observation of the surface detailed structure in the state-of-the-art SEM with the resolution less than 1 nm. The 10 nm × 100 nm-sized polycrystalline film morphologies of BP on PEDOT:PSS and dispersed submicron crystals on graphite was observed. The higher number of crystals on PEDOT:PSS than on HOPG implied that the acid-base interaction on surface rather than CH-π and π-π interactions critically affected the morphology (Figure 6-3). Modification of PEDOT:PSS surface with solution-processable graphene derivatives supported this hypothesis. Theoretical calculations further revealed that the protonated BP with structural deformation and deeper HOMO and LUMO level than that of BP helped accumulation of BP to work as a crystal nucleation site. The acid-base principle was further demonstrated on poly(3-hexylthiophene-2,5-diyl), a standard polymer donor material, to show the one-order difference in the domain size.

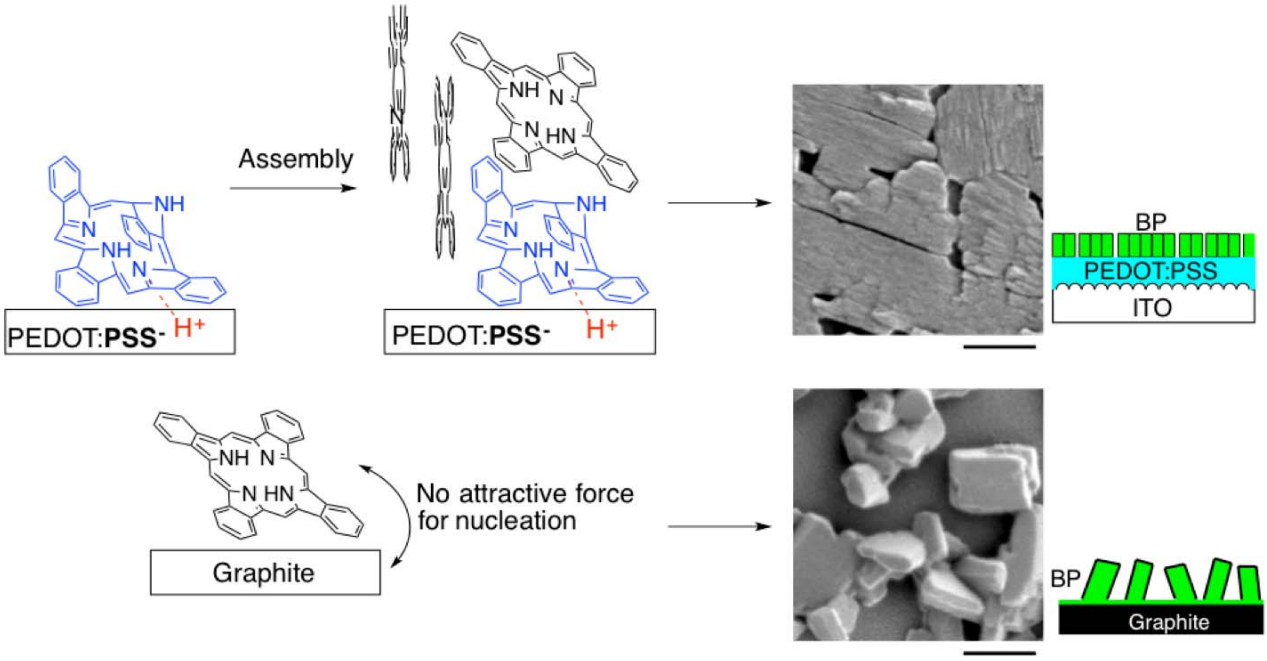

Figure 6-3. Morphological deviation of BP on PEDOT:PSS and graphitic substrate.

In Chapter 5, the mechanism of crystal growth in a small-molecule bulk heterojunction layer was described. Previous investigation revealed that the morphology of BP on polycrystalline flat BP layer can be controlled by casting the precursor of BP with co-casting molecules called matrices with various viscosities.[2] The qualitative discussion on the growth kinetics based on microscopic data was further supported by spectroscopic investigation and quantitative analysis on the crystal sizes and inter-crystalline distances from SEM images. I found that the generation of BP from its precursor and crystal growth finished within 4 min, and the further morphological change during continuous heating at 180 °C was due to the Ostwald ripening. The time scale of crystallization and ripening were supported by the simulation based on diffusion equation, where the diffusion of BP in phenyl-C_{61}-butylic acid *n*-butyl ester with the viscosity of 1250 Pa s took place in the order of seconds, whereas that of *N*, *N´*-dicarbazoyl-3,5-benzene with the viscosity of 0.03 Pa s took place in sub-milliseconds. This simulation result further implies that the possibility to estimate the stability of bulk heterojunction morphology based on the diffusion coefficient of the materials. In addition, from the perspective of crystal growth, the dependence of solvent viscosity on the obtained crystal size is inferred as long as the intermolecular interaction is similar.

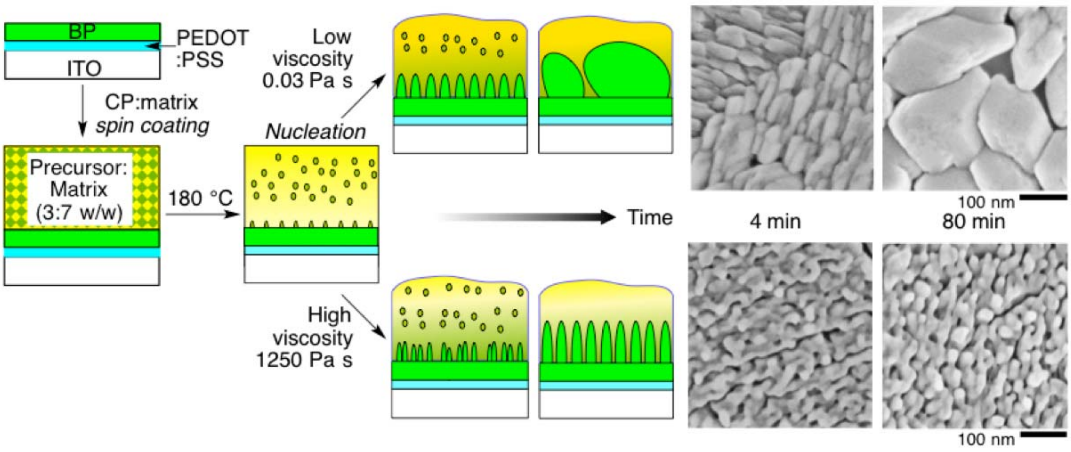

Figure 6-4. Time evolution of the morphologies of BP in matrices with different viscosity. SEM images were reproduced from ref. 2.

The key findings of the ability to quantitatively discuss the microscopic images discussed throughout this thesis will open the way toward quantitative microscopic studies in molecular level. I have demonstrated that the quantitative discussion is applicable to bond rotation, chemical reaction, and crystallization. It would be possible to further expand the scope to study the chemistry of single molecules and molecular clusters, including metal-organic complexes and clusters, further complex molecules involving in flexible nonbonding interactions such as polypeptides with secondary and tertiary structures, and biomineralization.

References

[1] Koshino, M.; Niimi, Y.; Nakamura, E.; Kataura, H.; Okazaki, T.; Suenaga, K.; Iijima, S. *Nat. Chem.* **2010**, *2*, 117–124.

[2] Oiki, M. Efficient Carrier Generation in Organic Photovoltaics by Controlling Phase-separated Morphology and Electronic Energy Level. *M.S. Thesis* The University of Tokyo, Tokyo, March 2014.